LBL-30652

Lawrence Berkeley Laboratory

UNIVERSITY OF CALIFORNIA

Materials & Chemical Sciences Division

Electronic Structure in the Actinides—Three Case Studies

W.K. Kot
(Ph.D. Thesis)

April 1991

LOAN COPY
Circulates
for 4 weeks
Bldg. 50 Library.
LBL-30652
Copy 2

Prepared for the U.S. Department of Energy under Contract Number DE-AC03-76SF00098

DISCLAIMER

This document was prepared as an account of work sponsored by the United States Government. While this document is believed to contain correct information, neither the United States Government nor any agency thereof, nor the Regents of the University of California, nor any of their employees, makes any warranty, express or implied, or assumes any legal responsibility for the accuracy, completeness, or usefulness of any information, apparatus, product, or process disclosed, or represents that its use would not infringe privately owned rights. Reference herein to any specific commercial product, process, or service by its trade name, trademark, manufacturer, or otherwise, does not necessarily constitute or imply its endorsement, recommendation, or favoring by the United States Government or any agency thereof, or the Regents of the University of California. The views and opinions of authors expressed herein do not necessarily state or reflect those of the United States Government or any agency thereof or the Regents of the University of California.

LBL - 30652

Electronic Structure in the Actinides — Three Case Studies

(Ph. D. Dissertation)

by

Wing K. Kot

Department of Chemistry
University of California
Berkeley, California 94720

and

Chemical Sciences Division
Lawrence Berkeley Laboratory
University of California
Berkeley, California 94720

April 1991

This work was supported by the Director, Office of Energy Research, Office of Basic Energy Sciences, Chemical Sciences Division of the U. S. Department of Energy under Contract No. DE-AC03-76SF00098.

Electronic Structure in the Actinides —— Three Case Studies

by

Wing Keung Kot

Abstract

The zero-field splittings (ZFS) of Cm^{3+} incorporated into single crystals of $LuPO_4$ have been determined by electron paramagnetic resonance (EPR) spectroscopy to be 0.0, 2.4, 8.0 and 9.3 cm^{-1} at 298K; they show a fair agreement with those measured by excitation and fluorescence experiments. The total splitting of ≈ 10 cm^{-1} is significantly smaller than the only previously known ZFS of the half-filled *5f* shell of Cm^{3+} (20.2 cm^{-1} in Cm^{3+}:$SrCl_2$). This unexpectedly small crystal-field interaction is probably responsible for the first room-temperature observation of an EPR signal of an actinide. The resulting spin-Hamiltonian parameters cannot be used to predict accurately the ground electronic states of the neighboring trivalent Kramers ions Pu^{3+} and Cf^{3+} diluted into $LuPO_4$.

The relatively low excited *6d* configuration in the Th^{3+} free ion is found to be stabilized relative to the *5f* by trigonal crystal-fields with no axial ligands to the extent that it becomes the ground configuration in tris(bis-trimethylsilylcyclopentadienyl) thorium (III) (Cp''_3Th) and trisindenyl thorium (III). The *5f* crystal-field states in Cp''_3Th are found to be over 15,000 cm^{-1} above ground. This represents the first instance where the ground electronic configuration in an actinide is different than $5f^n$. Theoretical consideration has reached the same conclusion. A similar crystal-field around Ce^{3+} was shown to result in a *5d* excited state that is the lowest in energy ever observed in trivalent cerium.

Reaction of $PaCl_5$ or $PaCl_4$ with $LiBH_3CH_3$ afforded the tetrahedral $5f^1$ complex $Pa(BH_3CH_3)_4$. Failure to observe an EPR signal with the complex is probably due to a Γ_8 quartet ground state and fast spin-lattice relaxation. The ^1H and ^{11}B NMR spectra were recorded; the sign of the upfield proton and the magnitude of the downfield boron isotropic shifts cannot be explained by a spin-polarization model. The same model, however, can be used to interpret the ^1H isotropic shifts in $Np(BH_3CH_3)_4$ and $U(BH_3CH_3)_4$, suggesting that there is a qualitative difference in the metal-ligand interaction between $Pa(BH_3CH_3)_4$ and its neptunium and uranium analogues. The hyperfine parameters K measured for $Np(BH_3CH_3)_4$ are -5.177 MHz for the bridging protons and -0.498 MHz for the terminal protons.

Glenn T. Seaborg

to my parents

Contents

Acknowledgements v

Chapter 1 Introduction 1

Chapter 2 Zero-Field Splitting of Cm^{3+} in $LuPO_4$

2.1 Introduction 5

2.2 Structures of $LuPO_4$ and YPO_4 8

2.3 Electronic Structure of Cm^{3+} in D_{2d} Symmetry 10

2.4 Experimental Results 15

2.4.1 X-Band EPR 15

2.4.2 Q-Band EPR 18

2.4.3 Temperature Dependence Studies 22

2.5 Analysis and Discussion 25

2.6 Absorption and Fluorescence Spectra of Cm^{3+}:$LuPO_4$ 35

2.6.1 Absorption Spectra of Cm^{3+}:$LuPO_4$ 36

2.6.2 Exictation Spectra of Cm^{3+}:$LuPO_4$ 37

2.6.3 Fluorescence Spectra of Cm^{3+}:$LuPO_4$ 41

2.7 EPR of Pu^{3+} and Cf^{3+} in $LuPO_4$ 43

2.7.1 EPR of Pu^{3+}:$LuPO_4$ 44

2.7.2 EPR of Cf^{3+}:$LuPO_4$ 46

2.8 Summary 48

Appendix 49

References 51

Chapter 3 Electronic Structures in Compounds of Trivalent Thorium

3.1 Introduction 53

3.2 EPR of $[\eta^5\text{-}C_5H_3(SiMe_3)_2]_3Th$ 55

3.3 EPR of $(C_9H_7)_3Th$ 58

3.4 Absorption Spectra of $[\eta^5\text{-}C_5H_3(SiMe_3)_2]_3Th$ 65

3.5 Electonic Structures of Cp''_3Th and $(C_9H_7)_3Th$ 68

3.6 EPR of Ce^{3+} in Trigonal Symmetry 76

3.7 Attempts to Prepare Lewis Base Adducts of Cp''_3Th 80

3.8 Summary 82

References 83

Chapter 4 Synthesis, Electronic Structure and NMR Studies of $Pa(BH_3CH_3)_4$

4.1 Introduction 87

4.2 Reaction of $LiBH_3CH_3$ with Niobium and Tantulum Halides, Cs_2MCl_6 (M = Zr, U, Np, Pu) and $CsUCl_6$ 90

4.3 Reaction of $LiBH_3CH_3$ with Cp_2ZrCl_2 and Cp_2TiCl_2 94

4.4 Syntheses of Protactinium Chlorides 102

4.4.1 Preparation of Pa^{4+}:Cs_2ZrCl_6 and its Reaction with $LiBH_3CH_3$ 102

4.4.2 Syntheses of $PaCl_5$ and $PaCl_4$ 104

4.4.3 Solubility of $PaCl_5$ in Aromatic Solvents 108

4.5 Reaction of $PaCl_5$ with $LiBH_4$ and $(CH_3C_5H_4)Na$ 110

4.6 Reaction of Protactinium Chlorides with $LiBH_3CH_3$ 113

4.7 Electronic Structure of $Pa(BH_3CH_3)_4$ 119

4.8 NMR of $Np(BH_3CH_3)_4$ and $Pa(BH_3CH_3)_4$ 122

4.8.1 Theory of Paramagnetic NMR Shifts 122

4.8.2 ^1H and ^{11}B NMR of $Np(BH_3CH_3)_4$ 126

4.8.3 ^1H and ^{11}B NMR of $Pa(BH_3CH_3)_4$ 129

4.9 Summary 133

4.10 Experimental 134

References 137

Acknowledgements

Malheureux peut-être l'homme, mais heureux
l'artiste que le désire déchire !

— Charles Baudelaire

Anyway you'll never know, the
many ways I've tried.

— The Beatles

Between what i saw and what i said, what i said and what i kept silent, what i kept silent and what i dreamt, what i dreamt and what i forgot,* there is a lot for me to acknowledge. Deeds have been done and words will never be enough; nonetheless, let me try.

Professor Glenn Seaborg has shown me exceptional patience and indulgence; i hardly felt entitled to them and in return now there is only my utmost gratitude. Much support came from Norman Edelstein. We differed on occasisons, but Norm put up with my decisions to meander in my research — he even let me work with PA when i could have just as well worked with cerium. Surely generosity knows no bound.

Generous were also those who supplied me with many different chemical samples. Dr. Marv Abraham and Dr. Lynn Boatner of Oak Ridge supplied the curium-doped crystals, Professor Michael Lappert of Sussex provided many thorium samples while Dr. Lester Morss of Argonne unfailingly met with my repeated request for more and more PA.

Of the LBL staff, many deserve more than just a thank you but it's the best that i can do. Jerry Bucher had an answer for every question or problem which he's more than willing to share. George Shalimoff had lent many a helping hand, related anecdotes and even assisted

*After Octavio Paz

with the crossword when i was stumped. Barbara Moriguchi-Iwai time and again offered her expertise and advice in everything ranging from word processing to sushi-making while Allan Zalkin had helped in more ways than just one-and-a-half strtucture.

Remembrance and appreciation go back to the SHEIKS and those who helped me get started, in particular Ken Gregorich and Ron Shinomoto; Ron had showed me much about synthetic chemistry.

There are, of course, the Andersens. Perhaps it's embarrassing to thank each and every one of them — it seems like i've been around long enough to know every generation of them — but i cannot stop for that. John, Steve, Tony, Rob, Sharon, Marc and Wayne had all been special; they provided whatever little realization there was of my not-too-realistic vision of what life in graduate school would be like. As for Dick himself, it's amazing that he so often rekindled in me the excitement about chemistry during the conversations that we've had, one regret is that they are so few and far in between.

Working with PA, to say the least, could be a lonely undertaking — most people kept the distance. Happily for me, they have stayed away from the PA but they have not stayed away from me. There's always somebody there to share and working with PA somehow became tolerable. Hope and fear, joy and despair, to share them all is no theme for the faint-of-hearts. My words are now far away when i attempt to thank my housemates — Isabelle literally fed and clothed me while Christophe's camaraderie, elle est grande et grosse. Myron had always remembered me no matter where he was, be it Jersey, Marseille or Stuttgart, i only prayed that i deserved it. Often bold and outrageous, at times stimulating and inspirational, but whatever he is, Kim is incomparable. Piehler and i shared quite a bit indeed, let's just hope they'll get better than point-charge calculations. Glen had been, in his words, a buddy; he's even managed to make many things from LA likable. Jane's laughter enchanted and enlivened more than a few listless afternoons; Jane, riez, riez toujours. i'll never be able to thank my family enough — they keep on giving and giving — and so i'll not; so much of these would have been meaningless if not for them.

This work was supported by the Director, Office of Energy Research, Office of Basic Energy Sciences, Chemical Sciences Divsion of the US Department of Energy under Contract No. DE-AC03-76SF00098.

Chapter 1

Introduction

After over 40 years since its first introduction [1], the concept of the actinide series is by now firmly established and universally accepted after some early doubts and arguments to the contrary. Most of the early doubts arose because of some of the unexpected and nonuniform properties exhibited by the actinides. For example, the actinide hypothesis has been argued against based on the variability in the stable oxidation states, especially in the first half of the series; such variability is much less pronounced in the lanthanides. As a series, the actinides do not show physical and chemical properties which are as smoothly varying as those found in the lanthanides. The situation can be understood by recognizing that the *5f* shell is not identical to the *4f* shell in many of its important properties, and so while important similarities exist between the two series, there are also striking differences.

The differences arise primarily because of the lower binding energies of the *5f* electrons and their less efficient shielding by the outer electrons when compared to the *4f* electrons. As a consequence, the *4f* shell in general can adequately be treated as an inner core orbital; the electronic and hence the chemical properties of the rare earths are therefore comparatively uniform. The great success of parametrization schemes in classical spectroscopy involving the *4f* electrons is a perfect illustration [2]; both the empirically determined free-ion

and crystal-field parameters show smooth variations along the series and excellent agreement is often obtained between experimental results and the theoretical model. In the case of the actinides, the stabilization and shrinkage of the *5f* orbitals occur much less precipitously (see Fig 3.8) such that only in the second half of the series can the *5f* be described as a localized and inner shell. The crossing point at which the *f* shell drops below the *d* shell in energy occurs at different points in the two series; the *5f* shell is not occupied in the actinide metal until protactinium while the magnetic behavior of all rare-earth metals can be treated as a collection of rare-earth trivalent ions with localized *f* electrons [3]. The *5f* orbitals are relatively extended spatially because of the inefficient shielding, experimentally this has been observed in the electron paramagnetic resonance (EPR) spectra of U^{3+} and Pu^{3+} in CaF_2, which show a superhyperfine interaction between the *5f* electrons and the ligand nuclei [4]; such interaction was not seen with Nd^{3+} or Sm^{3+}. The spatial diffuseness of the *5f* orbitals together with the many energetically accessible outer orbitals have meant special chemical and spectroscopic interests. Chemically, the different oxidation states and importance of covalency in actinide compounds are well-known; the richness of organouranium chemistry [5] has made that of neodymium seem monotonous. Spectroscopically, parametrization schemes for the actinides are not as successful as in the lanthanides and the challenge is to interpret the experimental data with different and often more complicated models.

Chemistry is very much a science of interpolation and extrapolation among the periodic table. Given the large number of different interactions which are either not found or less important in the lanthanides (e.g. spin-orbit coupling, relativistic effect [6], larger radial distribution of the *5f* orbitals), the interpolation and extrapolation in the actinide series must be done more cautiously and over a wider range. For example, the metal (III–IV) oxidation potentials of the actinides extend over a range of over 12 V while those of the lanthanides spread over 6 V [7]; nobelium has a stable divalent state in aqueous solution while ytterbium behaves much like the neighboring elements with a stable trivalent state [8].

This Thesis describes the efforts to study the electronic structure of the actinides in three different systems. In Chapter 2, the zero-field splitting of Cm^{3+} incorporated into single crystals of $LuPO_4$ has been determined by a combination of electron paramagnetic resonance and optical measurements. It is found that while the $5f^7$ configuration shows a larger interaction

with the crystal-field than the $4f^7$ configuration of Gd^{3+} through intermediate coupling, the two configurations are similar in the sense that room-temperature EPR can be observed of the Russell-Saunders ground *S* term. Compounds of all actinides were previously found to be EPR silent at room temperature; even the nominal *S* ground states of Am^{2+}, Cm^{3+} and Bk^{4+} were thought to be too impure through intermediate coupling for observation of EPR at room temperature. The ground electronic configuration in compounds of trivalent thorium is found to be $6d^1$ in Chapter 3, showing the importance of the closeness in energy of various orbitals at the beginning of the actinide series. In contrast, the relative stability of the core-like *4f* orbital is demonstrated in trivalent cerium. Chapter 4 describes the attempt to study the electronic structure in $Pa(BH_3CH_3)_4$. Because of its scarcity and radioactivity, protactinium has received relatively little study both electronically and chemically. This is unfortunate because this early actinide is expected to have interesting electronic and chemical properties due to the large radial distribution of its *5f* wavefunction and a low-lying *6d* configuration; with only one unpaired electron, its tetravalent state is also expected to have a simple electronic structure.

References

[1] (a) G. T. Seaborg, *Man-Made Transuranium Elements*, Chapter 3 (Prentice-Hall, New Jersey, 1963). (b) G. T. Seaborg, J. J. Katz and W. M. Manning, Nat. Nucl. Energy Series IV, **14B**, (1949).

[2] See, for example, S. Hüfner, *Optical Spectra of Transparent Rare Earth Compounds*, (Academic Press, New York, 1978).

[3] B. Cogblin, *The Electronic Structures of Rare-Earth Metals and Alloys: the Magnetic Heavy Rare Earths*, (Academic Press, London, 1977).

[4] W. Kolbe and N. Edelstein, Phy. Rev. B **4**, 2869 (1971).

[5] J. G. Brennan, Ph. D. Dissertation, University of California at Berkeley (1985).

[6] K. S. Pitzer, Acc. Chem. Res. **12**, 271 (1979).

[7] J. L. Nugent, R. D. Baybarz, J. L. Burnett and J. L. Ryan, J. Inorg. Nucl. Chem. **33**, 2503 (1971).

[8] J. Maly, T. Sikkeland, R. J. Silva and A. Ghiorso, Science **160**, 1114 (1968).

Chapter 2

Zero-Field Splitting of Cm^{3+} in $LuPO_4$

2.1 Introduction

Atoms and ions with half-filled shells occupy an unique position in chemical studies. Their electronic ground states, in the limit of Russell-Saunders coupling, are characterized by $L = 0$ and are not split by the electric field of the surrounding ligands because of the spherical symmetry. Crystal-field splittings of these S-states (crystal-field is taken to include all interactions between the central ion and the ligands in this thesis, as opposed to only the electrostatic crystal-field), however, are observed experimentally; and the mechanisms which cause their splittings have become a subject of much interest and perplexity. While there is a fair understanding of the relatively small splittings found in transition metals, there is little progress made in interpreting the larger splittings present in the lanthanides. The situation is even worse in actinides. Experimentally, in contrast to the large body of data that exists for Mn^{2+}, Fe^{3+} ($3d^5$), Eu^{2+}, Gd^{3+} ($4f^7$), N and even $O^+(2p^3)$, data for the $5f^7$ ions Am^{2+}, Cm^{3+} and Bk^{4+} are seriously lacking. Theoretical study of S-state splittings in actinides is practically non-existent.

Electron paramagnetic resonance spectroscopy (EPR) has been the technique of choice to study these S-state splittings because their magnitudes are on the order of $0.0001 - 1\ cm^{-1}$. The first reported observation of Cm^{3+} by EPR was made independently by two groups with

essentially the same results [1] —— Cm^{3+} incorporated into crystals of $LaCl_3$ gave a spectrum of seven lines with a Landé g-factor of 1.991. These results are practically identical to those of Gd^{3+}:$LaCl_3$, suggesting very similar zero-field splittings (ZFS) in the two systems. However, in view of the much larger spin-orbit coupling in Cm^{3+}, both the g-value and the crystal-field splitting are expected to be different than those of Gd^{3+}. To resolve these discrepancies, Abraham *et al.* [2] repeated the experiment with Cm^{3+} in crystals of $LaCl_3$ and $La(C_2H_5SO_4)_3{\cdot}9H_2O$, showing that the earlier spectra were due to Gd^{3+} impurities and that the Cm^{3+} resonance consisted of only one anisotropic line with a g-value of 1.925. The new results are more consistent with theory and the fact that only one line was observed indicated that the ZFS was large compared to the frequency at which the resonance was observed. Thereafter, the EPR of Cm^{3+} and the isoelectronic Am^{2+} and Bk^{4+} had received more studies, but almost exclusively in crystals with cubic site symmetry such as CaF_2, $SrCl_2$ and ThO_2.

$O^+(3)$	$\overline{O}, \overline{T}_d$	$\overline{D}_{2d}$
$D_{5/2}$	$\Gamma_7\,(\Gamma_6)^a + \Gamma_8$	$\Gamma_6 + 2\Gamma_7$
$D_{7/2}$	$\Gamma_6 + \Gamma_7 + \Gamma_8$	$2\Gamma_6 + 2\Gamma_7$

TABLE 2.1 Decomposition of Irreducible Representations of $O^+(3)$ into Irreducible Representations of the Double Groups $\overline{O}$, $\overline{T}_d$ and $\overline{D}_{2d}$ ($^a\Gamma_6$ in $\overline{T}_d$ symmetry)

In cubic site symmetry, the ground $J = 7/2$ manifold of Cm^{3+} is split into three Stark components with labels Γ_6, Γ_7 and Γ_8, following the decomposition of the irreducible representations of the continuous rotation group $O^+(3)$ into irreducible representations of the cubic double group $\overline{O}$ (Table 2.1). Both Γ_6 and Γ_7 are Kramers doublets while Γ_8 is a quartet. In all but one of the cases studied, resonance could only be observed at liquid helium temperature and only one line was seen, corresponding to the transition within the ground doublet Γ_6. Using a higher microwave frequency and a larger magnetic field caused admixture by Zeeman interactions of the excited state Γ_8 into the ground Γ_6 doublet. The observed

transition became anisotropic and from the anisotropy of the resonance the energy of the Γ_8 state could be calculated. Kolbe *et al.* [3] tabulated the $\Gamma_6 \rightarrow \Gamma_8$ splittings for Gd^{3+} and Cm^{3+} in various hosts and the list is reproduced in Table 2.2.

Host	Lattice Constant	Gd^{3+}	Cm^{3+}
CeO_2	5.41 Å	0.0653 cm^{-1}	17.8 cm^{-1}
ThO_2	5.60	0.06645	15.5
CaF_2	5.46	0.0578	13.4
SrF_2	5.80	0.0501	11.2
BaF_2	6.20	0.0448	—
$SrCl_2$	7.00	0.0198	5.13

TABLE 2.2 $\Gamma_6 \rightarrow \Gamma_8$ Splittings of Gd^{3+} and Cm^{3+} in Various Cubic Site Symmetry Hosts (From Reference 3)

Electronic structures of Cm^{3+} and Gd^{3+} in a crystal-field will be discussed in a later section, but it is obvious from Table 2.2 that the ZFS of the two are very different and the splittings found in Cm^{3+} are in general orders of magnitude larger than those found in Gd^{3+}. It has actually been suggested that "for actinides the splittings are too great to be properly studied by standard EPR techniques [4]." The complete ZFS of Cm^{3+} in various hosts have been estimated to be 10–50 cm^{-1}. Indeed there is only one instance where the complete ZFS of the ground $J = 7/2$ manifold of Cm^{3+} is determined by EPR —— Cm^{3+}:$SrCl_2$. It is also the only system where the total ZFS of Cm^{3+} is known; no other experimental technique has been applied to its study. In this system, unlike the others in Table 2.2, resonance could be observed at a temperature as high as 200 K. Moreover, a second transition was found and could be assigned as the transition within the excited Γ_7 doublet. The $\Gamma_8 \rightarrow \Gamma_7$ splitting could be determined from the admixture of the Γ_8 state and was found to be 15.3 cm^{-1}, thus the total ZFS of Cm^{3+}:$SrCl_2$ is 20.43 cm^{-1} [5]. Transitions involving the Γ_8 state were not observed.

Even less data exist for Cm^{3+} doped into crystals with non-cubic site symmetry. Other than $LaCl_3$ and $La(C_2H_5SO_4)_3 \cdot 9H_2O$, only one system, Cm^{3+}:$ThSiO_4$, has been studied and no EPR could be observed. It is against this background that experimental work on Cm^{3+} doped in single crystals of $LuPO_4$ (and, to a lesser extent, YPO_4), to be described in this chapter, was undertaken.

2.2 Structure of $LuPO_4$ and YPO_4

Both $LuPO_4$ and YPO_4 belong to a large group of crystals that possess the zircon structure which is made up of linked RO_4 (R = V, P, As, Si, Ge) and MO_4 (M = metal) tetrahedra. The crystal is tetragonal and the space group is D_{4h}^{19} ($I4/amd$). The ionic radii of Lu^{3+} and Y^{3+} are very similar (0.977 and 1.019 Å respectively for eight-coordination) [6] and so are the cell dimensions for the two phosphates: a = 6.798 Å and c = 5.961 Å for $LuPO_4$ and a = 6.885 Å and c = 5.982 Å for YPO_4. The unit cell contains four molecules and Figure 2.1 shows the arrangement of the PO_4 tetrahedra around it. The site of the metal ion forms the center of two interlocking tetrahedra whose corners are occupied by oxygen atoms, thus the point group symmetry of the metal site is D_{2d}. The two tetrahedra are of different sizes and hence there are two sets of metal-oxygen distances —— 2.263 Å and 2.346 Å for $LuPO_4$; 2.314 Å and 2.374 Å for YPO_4 [7]. The crystal axes a, a and c are related to the D_{2d} axes x, y and z by a rotation of $\pi/4$ about the c (equivalent to the z) axis; x and y are two equivalent axes. This is important to note because it greatly simplifies the alignment of the crystals in the experiments to be described.

The crystals used in this work, $^{243,244}Cm$ and ^{248}Cm doped in $LuPO_4$ and YPO_4, were supplied by L. A. Boatner and M. M. Abraham of Oak Ridge National Laboratory. They were grown by a flux method described before [8]. The crystals selected for the experiments had typical dimensions of 5 mm × 2 mm × 1 mm (the long dimension coincides with the crystal c-axis) and were transparent with a pink tint. The $^{243,244}Cm$ -doped crystals turned black in

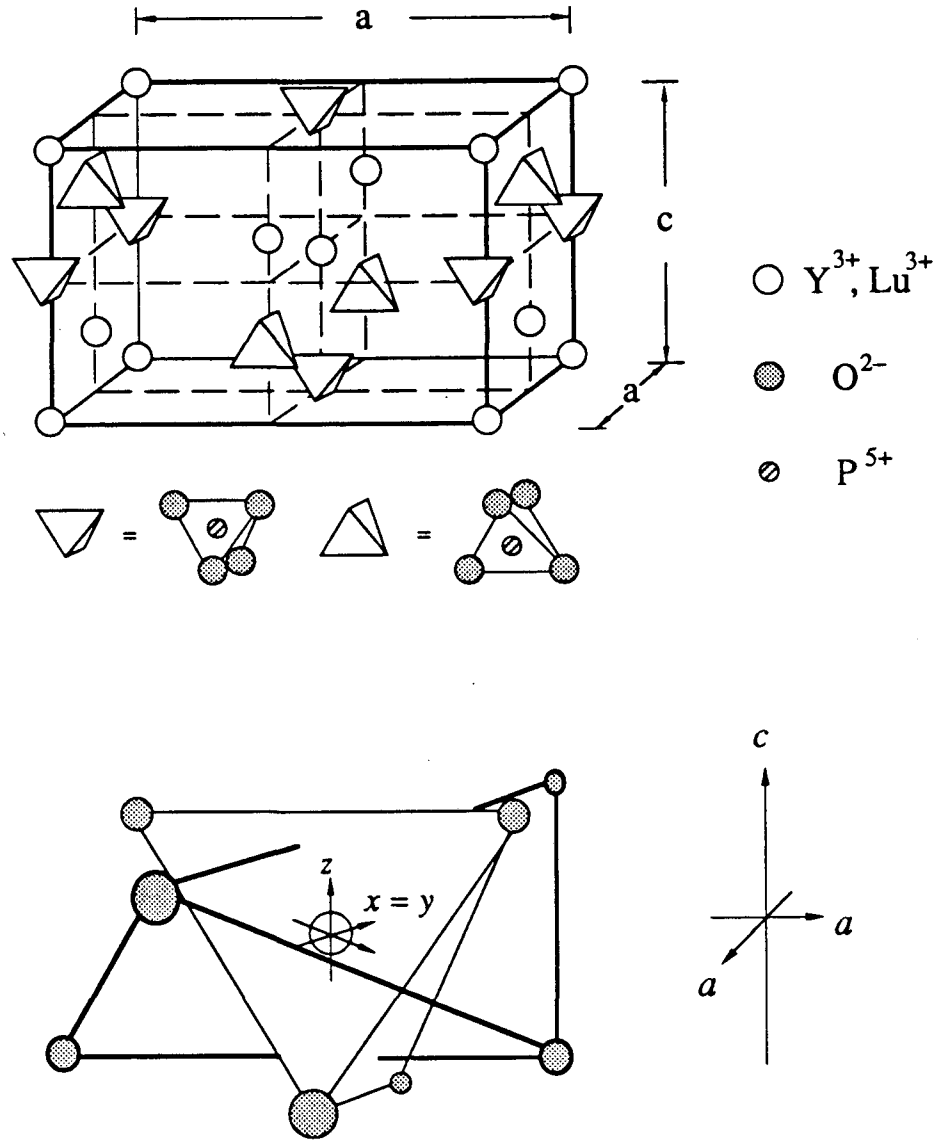

FIGURE 2.1 Unit cell of the tetragonal zircon structure of $Lu(Y)PO_4$(top). Two interlocking tetrahedra centered at the metal ion (bottom), the D_{2d} axes (x, y, z) are related to the crystal axes (a, a, c) by a $\pi/4$ rotation about the c (z) axis.

days because of radiation damage (half-life of $^{243}Cm = 28.5\ y$, $^{244}Cm = 18.11\ y$ and $^{248}Cm = 3.397 \times 10^5\ y$) which severely degraded the quality of the spectra obtained. Annealing the crystals at ≈550 °C for a few hours returned the crystals to their original condition but after a few such annealings, the damage to the crystals appeared to be permanent and the crystals remained gray to black in appearance.

The ionic radius of eight-coordinated Cm^{3+} is unknown, but the radius of six-coordinated Cm^{3+} (0.97 Å) is considerably larger than those of Lu^{3+} and Y^{3+} (0.861 Å and 0.900 Å respectively). However, it is expected that the Cm^{3+} will substitute for a Lu^{3+} (or Y^{3+}) in the crystal lattice and occupy a D_{2d} site because all trivalent sites are equivalent and the other cationic site is even smaller. Furthermore, ions of even a larger size than Cm^{3+} such as Ce^{3+} (1.01 Å) was found to take up only the D_{2d} site in both of these lattices [9]. Any amount of distortion in the lattice caused by the size mismatch is not expected to destroy the D_{2d} site symmetry.

The concentration of Cm^{3+} in the crystals is not known with certainty, but is estimated to be less than 0.1 %.

2.3 Electronic Structure of Cm^{3+} in D_{2d} Symmetry

The Hamiltonian H of an ion placed in a crystal field consists of $H_{free\text{-}ion}$, the free ion Hamiltonian, and $H_{crystal\text{-}field}$, which is the perturbation produced by the surrounding charge distribution.

$$H = H_{free-ion} + H_{crystal-field} \tag{2.1}$$

$$H_{free-ion} = \sum_i \left(\frac{p_i^2}{2m} - \frac{Ze^2}{r_i}\right) + \sum_{i<j} \frac{e^2}{r_{ij}} + \sum_i \xi(r)\, l_i \cdot s_i \tag{2.2}$$

The summations in (2.2) are, in order, the electron-nuclear interaction, interelectronic repulsion and spin-orbit coupling. Because of the diffuseness of the $5f$ orbitals, the Coulomb integrals in

the actinides are smaller than the corresponding integrals in the lanthanides; at the same time spin-orbit interaction in the actinides is much larger because of their higher Z. As a result, one of the most notable features of the electronic structure of actinides is the breakdown of Russell-Saunders coupling and a pronounced tendency towards *jj* coupling [10]. This breakdown of Russell-Saunders coupling will admix levels with the same J value and the largest admixtures will result from levels for which $\Delta L = 0, \pm 1$ and $\Delta S = 0, \pm 1$. The Gd^{3+} free ion has a spin-orbit coupling constant ζ_{4f} of $\approx$ 1,500 cm^{-1} and its Russell-Saunders ground term of $^8S_{7/2}$ is J-mixed with states like $^6P_{7/2}$ and $^6D_{7/2}$. Its actinide analogue Cm^{3+} has a ζ_{5f} of $\approx$ 3,000 cm^{-1}. In addition, the first few excited $J = 7/2$ manifolds in Cm^{3+} are lower in energy than those found in Gd^{3+}; for example, two excited $J = 7/2$ manifolds are at $\approx$ 17,000 and 22,000 cm^{-1} in Cm^{3+} while they are at $\approx$ 32,000 and 36,000 cm^{-1} in Gd^{3+}. The effect of the much larger spin-orbit coupling in Cm^{3+} is shown by these calculated free-ion wavefunctions [11]:

$$Gd^{3+} \quad 0.9844|^8S_{\frac{7}{2}}\rangle + 0.1736|^6P_{\frac{7}{2}}\rangle - 0.0140|^6D_{\frac{7}{2}}\rangle + \ldots$$
$$Cm^{3+} \quad 0.8884|^8S_{\frac{7}{2}}\rangle + 0.4197|^6P_{\frac{7}{2}}\rangle - 0.0909|^6D_{\frac{7}{2}}\rangle + \ldots$$

and so while the Gd^{3+} ground state has a 97 % S-state character, it is only 79 % pure for Cm^{3+}. It is generally believed that this larger non-S character in Cm^{3+} is the primary reason of the more substantial crystal-field interaction experienced by its ground state than that of Gd^{3+} (see Table 2.2). Another consequence of this larger non-S character in Cm^{3+} is that spin-lattice relaxation in a crystalline host becomes more efficient such that low temperature is required to observe EPR of Cm^{3+}. Unlike Gd^{3+}, no EPR of Cm^{3+} or any other actinide has ever been observed at room temperature.

When introduced into a crystal lattice, the metal ions' interactions with the ligands are described by the perturbative crystal-field Hamiltonian which has been found to be very successful when applied to spectroscopy of the rare earths. Energy levels and symmetries of the crystal-field states can be explained and predicted very well by the model. The same treatment applied to the actinides has been much less successful. Such a difference is attributed to the fact that the $4f$ orbitals are more deeply buried in the core and the surrounding ions only create a slight perturbation which is chiefly electrostatic. The $5f$ orbitals, being more diffuse and

less tightly bound, interact much more strongly with the ligands. Covalency is also thought to be more important. Crystal-field splittings in the actinides therefore are generally much greater than in the lanthanides.

The eigenfunctions to (2.2) have complete spherical symmetry and so the crystal-field Hamiltonian is normally expanded in terms of spherical harmonics or operators that have the same transformation properties. Consequently,

$$H_{crystal-field} = \sum_{k,q} B_q^k C_q^k \tag{2.3}$$

where C_q^k's are operators defined by the spherical harmonics $Y_q^k(\theta, \phi)$

$$C_q^k = \left(\frac{4\pi}{2k+1}\right)^{\frac{1}{2}} Y_q^k(\theta, \phi) \tag{2.4}$$

and B_q^k's are the crystal-field parameters to be determined empirically from experimental data, using free-ion wavefunctions as basis sets. While ideally one would like to treat these parameters as physical quantities, in practice it is found that little physical meaning can be attached to them. Simple-minded point-charge calculations certainly give no useful insight to the problem, but even some of the most sophisticated *ab initio* calculations performed have not been found to give satisfactory agreement with experiments [12]. Crystal-field model and variations of it are useful primarily as phenomenological parametrization schemes, any success they may show demonstrates the power of group theory. It is perhaps ironic that the usefulness of the crystal-field model is mainly attributable to this fact. Consider the problem at hand. In D_{2d} symmetry, Equation (2.3) becomes

$$H_{crystal-field} = B_0^2C_0^2 + B_0^4C_0^4 + B_4^4(C_4^4 + C_{-4}^4) + B_0^6C_0^6 + B_4^6(C_4^6 + C_{-4}^6) \tag{2.5}$$

and the $C_{\pm 4}^k$'s transform like $[J_\pm]^4$, where J_+ and J_- are the raising and lowering operators respectively. As a result, free-ion states with $\Delta M_J = \pm 4$ are connected by the tetragonal crystal

field. It is hereby emphasized again that a pure S-state ion is *not* split by the electrostatic interaction with the crystal-field and other mechanisms have to be invoked to explain the experimentally observed splittings. However, since the crystal-field theory makes no assumption about the underlying physical process, it is still an useful model to describe the ground state splittings of Gd^{3+} and Cm^{3+} and S-state ions call for special treatment only in the sense that a different set of parameters is required. The ground $J = 7/2$ manifolds of Gd^{3+} and Cm^{3+} are split in D_{2d} symmetry into four Stark levels, each of which is a Kramers doublet, and are labeled by the irreducible representations of the double group $\overline{D}_{2d}$ (Table 2.1):

Doublets	Wavefunctions	Zeroth-order Energies
$\Gamma_7(\pm 1/2)$	$a\,\lvert\pm 1/2\rangle - b\,\lvert\mp 7/2\rangle$	$-5b_2^0 + 9b_4^0 - 5b_6^0$
$\Gamma_6(\pm 3/2)$	$c\,\lvert\pm 3/2\rangle - d\,\lvert\mp 5/2\rangle$	$-3b_2^0 - 3b_4^0 + 9b_6^0$
$\Gamma_6(\pm 5/2)$	$c\,\lvert\pm 5/2\rangle + d\,\lvert\mp 3/2\rangle$	$+1b_2^0 - 13b_4^0 - 5b_6^0$
$\Gamma_7(\pm 7/2)$	$a\,\lvert\pm 7/2\rangle + b\,\lvert\mp 1/2\rangle$	$+7b_2^0 + 7b_4^0 + b_6^0$

(2.6)

The crystal-field parameters describing this ground S-state splitting are in general not applicable to the excited states whose energy levels are normally determined by methods such as absorption spectroscopy. Crystal-field parametrization of the ground S-state of course is normally not practical; for the present case, it requires five parameters for three energy levels. Nonetheless, if crystal-field parameters for a ground S-state is available, any correlation they may have with those that describe the excited states will be indicative of the mechanisms for the S-state splitting.

Another parametrization scheme that is commonly used in EPR and closely related to the crystal-field model is the spin-Hamiltonian,

$$H_{spin} = g\mu_B H\cdot S + \tfrac{1}{3}b_2^0 O_2^0 + \tfrac{1}{60}(b_4^0 O_4^0 + b_4^4 O_4^4) + \tfrac{1}{1260}(b_6^0 O_6^0 + b_6^4 O_6^4) \tag{2.7}$$

where S is an "effective spin", $g\mu_B H\cdot S$ is the Zeeman interaction, O_n^m's are the Stevens operators [13] and b_n^m's are the spin-Hamiltonian parameters. The spin-Hamiltonian is used to give a shorthand description of the experimental results. By convention, S is assigned a value

such that $(2S+1)$ equals the observed number of energy levels and therefore is only a fictitious spin [14]. The spin-Hamiltonian parameters are related to the crystal-field parameters by a series of constants [15].

The ordering and energies of the crystal-field states are a function of the spin-Hamiltonian (or crystal-field) parameters. In general b_2^0 is dominating and so its sign determines the ordering of the states while the off-diagonal b_n^4's are much smaller and little mixing between states results, i.e. b and d in (2.6) are small. When the b_n^4's are ignored, the energies of the four Kramers doublets are given in (2.6) and Γ_7 (±7/2) will be the ground state if b_2^0 is negative; otherwise, Γ_7 (±1/2) is lowest. Though small, the crystal-field induced admixture is responsible for making transitions within all the doublets possible. Consider the Zeeman operator $\beta H\cdot(L+g_eS)$, it can be approximated as $g_J\beta H\cdot J$ if J-mixing is ignored. The first-order Zeeman effect can then be found simply by evaluating the matrix elements of J_x, J_y and J_z ($J_x = J_y$ in axial symmetry), i.e.

$$\begin{aligned} \langle JM_J \mid H_{zeeman\,\parallel} \mid JM_J' \rangle &= g_J\beta H_z \langle JM_J \mid J_z \mid JM_J' \rangle = g_J\beta H_z M_J \delta_{M_J M_J'} \\ \langle JM_J \mid H_{zeeman\,\perp} \mid JM_J' \rangle &= \tfrac{1}{2} g_J\beta H_x \langle JM_J \mid J_\pm \mid JM_J' \mp 1 \rangle = \tfrac{1}{2} g_J\beta H_x [(J \pm M_J)(J \mp M_J + 1)]^{1/2} \end{aligned} \tag{2.8}$$

and the components of the g-tensors of the spin Hamiltonian within each doublet with effective spin $S = \frac{1}{2}$ are given by

$$\begin{aligned} g_\parallel &= 2\, g_J M_J \\ g_\perp &= g_J[(J \pm M_J)(J \mp M_J + 1)]^{1/2} \end{aligned} \tag{2.9}$$

Thus it is seen that without crystal-field mixing, all but the Γ_7 (±1/2) state (all Kramers doublets will from now on be labled by their principal components i.e. Γ_7 (±1/2) = $|\pm\frac{1}{2}\rangle$) will have $g_\perp = 0$ and no transition will be allowed. In the only previous investigation of Cm^{3+} in a D_{2d} site symmetry host, $ThSiO_4$ [16], no EPR signal was detected. This was explained by the fact that, analogous to Gd^{3+}:$ThSiO_4$ [16], the ground doublet is primarily $|\pm\frac{7}{2}\rangle$ with $g_\perp \approx 0$. Resonances

within excited doublets were not seen presumably because they were not populated at the low temperature required for the experiment.

2.4 Experimental Results

Crystals chosen for experiments were all annealed at ≈ 550 °C . For the X-band (≈ 9 GHz) experiments, the crystals were mounted inside a Kel-F cylinder such that their crystallographic *c* axis rested horizontally. The Kel-F cylinder in turn was loaded into an EPR tube which was sealed after it was filled with ≈ 200 mmHg of helium gas. To prevent the crystals from being inadvertently displaced during the experiment, the Kel-F cylinder was machined such that both the fit of the crystal in it and itself in the EPR tube are snug. Spectra could be recorded from ≈2 to 350 K with the use of an Oxford continuous flow cryostat ESR-910.

For the Q-band (≈ 35 GHz) experiments, the crystals were loaded in a piece of polyethylene tubing which was flame sealed on both ends. The outside of the tubing was decontaminated for radioactivity before being fixed horizontally inside the Q-band cylindrical TE_{011} cavity. Experiments could be performed at 300, 77 and 4 K. Data for Cm^{3+}:YPO_4 were collected at 300 and 4 K only.

The angle θ between the crystal *c* axis and the magnetic field was varied by use of a goniometer attached on the X-band resonant cavity, and in the case of the Q-band experiments, by rotating the magnet pole-faces. Microwave radiation was generated with Varian E101 (X-band) and E110 (Q-band) microwave bridges. The microwave frequency was measured using an EIP-548 frequency counter and the magnetic field was determined with a Varian E-500 NMR Gaussmeter.

2.4.1 X-Band EPR

Figure 2.2 shows a sample of X-band EPR spectra for Cm^{3+}:$LuPO_4$ obtained at various temperatures. Many lines were observed but by comparison to the EPR spectrum of

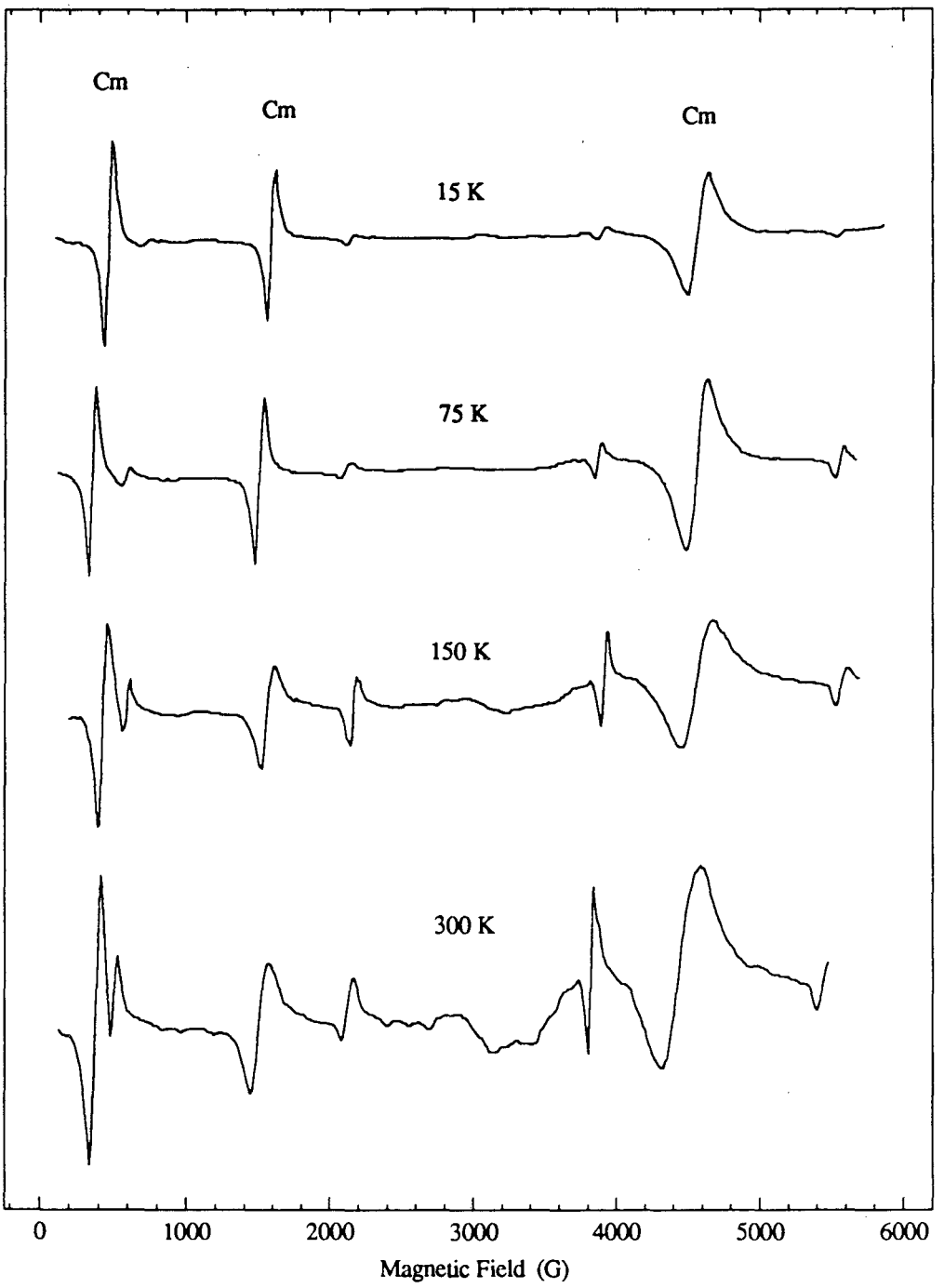

FIGURE 2.2 EPR spectra of Cm^{3+}:$LuPO_4$ at various temperatures (peaks not labeled are due to Gd^{3+} impurities) Microwave Frequency = 9.235 GHz and $\theta = 0°$.

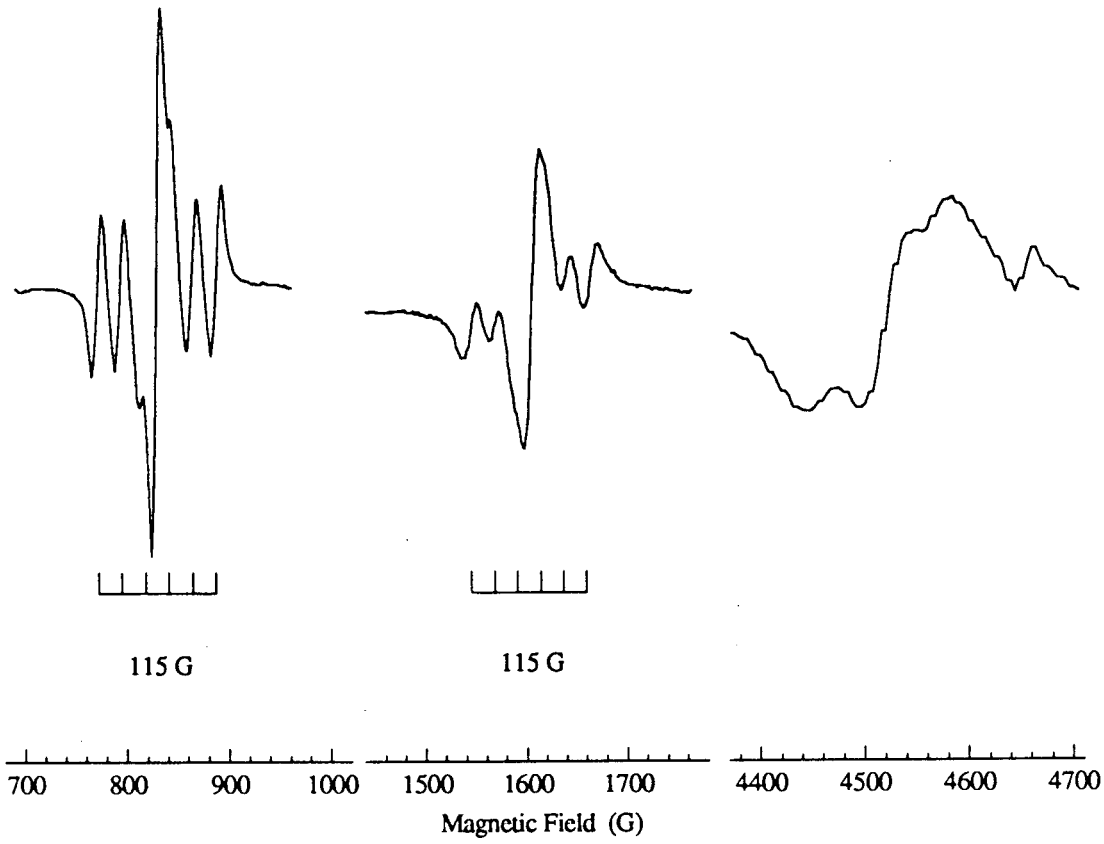

FIGURE 2.3 EPR spectrum of $^{243,244}Cm^{3+}$:$LuPO_4$ showing hyperfine structure. Microwave frequency = 9.233 GHz and temperature = 77 K.

Gd^{3+}:$LuPO_4$, it was found that only three of the lines could be assigned to Cm^{3+}, the rest were due to Gd^{3+} impurities. This assignment was confirmed by the spectra of $^{243,244}Cm$ (Fig 2.3) which showed a distinctive six-line hyperfine structure (I = 5/2 and 0 for ^{243}Cm and ^{244}Cm, respectively). The parallel hyperfine coupling constant measured is 23.10 G, compared to 20.92 G found previously for ^{243}Cm:$SrCl_2$ [17]. The lines due to Gd^{3+} were in general narrower and could be saturated at low temperature and only interfered with data-collecting when they overlapped with the Cm^{3+} lines. The Cm^{3+} resonances could be observed even at room temperature with peakwidths ranging from 20 to 80 G. They showed little change with temperature apart from one line (assigned below as $|\pm\frac{1}{2}\rangle$) which sharpened considerably as the temperature was lowered. This is the first indication that the crystal-field states are relatively

close in energy, otherwise a sizeable change in relative intensity should be present. The relative intensity of the transition within $|\pm\frac{1}{2}\rangle$ decreases at low temperature, suggesting that the $|\pm\frac{7}{2}\rangle$ state is the ground state. The measured g-values were least-squares fitted to the relation

$$g^2 = g_{\parallel}^2 \cos^2\theta + g_{\perp}^2 \sin^2\theta \tag{2.10}$$

and the resonances could be assigned to the doublets $|\pm\frac{5}{2}\rangle$, $|\pm\frac{3}{2}\rangle$ and $|\pm\frac{1}{2}\rangle$ (2.8). The g-values showed a small temperature dependence, reflecting the change in crystal-field with temperature, and they are listed in Table 2.3. No resonance with g-values corresponding to the $|\pm\frac{7}{2}\rangle$ doublet was found. This can be likened to the doublet in Cm^{3+}:$ThSiO_4$ [16] —— small tetragonal mixing of the $|\mp\frac{1}{2}\rangle$ doublet into $|\pm\frac{7}{2}\rangle$ results in a small $g_{\perp}$ value and hence a low transition probability. The g-values of $|\pm\frac{7}{2}\rangle$ are evaluated with Equation 2.8 using the values of a and b found for the $|\pm\frac{1}{2}\rangle$ state. Note also that more crystal-field mixing is seen to occur at a lower temperature.

Temperature	298 K		77 K		4K	
	$g_{\parallel}$	$g_{\perp}$	$g_{\parallel}$	$g_{\perp}$	$g_{\parallel}$	$g_{\perp}$
$a\,\|\pm 1/2\rangle - b\,\|\mp 7/2\rangle$	1.46(3)	7.34(2)	1.422(2)	7.341(5)	1.380(3)	7.284(3)
$c\,\|\pm 3/2\rangle - d\,\|\mp 5/2\rangle$	4.17(2)	3.98(2)	4.15(1)	4.083(2)	4.12(1)	4.10(1)
$c\,\|\pm 5/2\rangle + d\,\|\mp 3/2\rangle$	8.06(2)	3.98(1)	7.971(2)	4.083(2)	7.977(3)	4.102(2)
$a\,\|\pm 7/2\rangle + b\,\|\mp 1/2\rangle$	(12.79)[a]	(0.21)	(12.72)	(0.23)	(12.69)	(0.25)

TABLE 2.3 Measured g-values of Cm^{3+}:$LuPO_4$ at Various Temperatures (Microwave Frequency = 9.17 to 9.32 GHz). [a]Values in parentheses are calculated using $g_J = 1.925$.

2.4.2 Q-Band EPR

A typical Q-band spectrum is shown in Figure 2.4. Among the notable features is the presence of many lines, sometimes as many as six Cm resonances were detected. However, not all of these could be followed as the angle θ was varied, either because their intensities decreased rapidly or the maximum magnetic field available was not high enough. Other than the resonances already observed in the X-band experiments, only one line could be followed to any reasonable extent. This resonance occurred at very low field and showed a large temperature dependence (Fig 2.5). Furthermore, this line has very different g-values and opposite temperature dependences in the two different crystal systems. This is very puzzling because the two crystals are almost identical in structure and they are expected to have a very similar crystal-field around the Cm^{3+} ion. At room temperature and $\theta = 90°$, this resonance has a g-value of 49 in $LuPO_4$ and 15 in YPO_4; but when the temperature was lowered to 77 K, they shifted dramatically to 22 and 18 respectively. This line cannot be assigned to a transition within any of the four Kramers doublets, and can only arise from a transition between different doublets. 'Inter-doublet' transitions are common in lanthanide systems such as Gd^{3+}:$LuPO_4$ [8] and Tb^{4+}:ThO_2 [18] where the ZFS are small (the term 'inter-doublet' is used loosely here as the Kramers doublets lose their identities at high magnetic field, but it aptly describes the present situation especially when the transition takes place at very low field); for instance, all seven magnetic dipole allowed transitions ($\Delta M_s = \pm 1$) were observed in Gd^{3+}:$LuPO_4$. But this is rather unexpected for Cm^{3+} because it would represent an energy separation between two doublets ($\approx$ 35 GHz, 1.2 cm^{-1}) that is considerably smaller than any of the splittings measured before (Table 2.2). Much of the later experiments were therefore designed to confirm this $\approx$ 1 cm^{-1} splitting. As θ changed from 90° to 0°, the intensity of this line decreased and became too weak to be detected at $\approx$ 5°. This can be explained by considering the Zeeman matrix element (Equation 2.7) between the different doublets. It is seen that all perpendicular Zeeman matrix elements are different than zero. On the other hand, no two states are connected by the parallel Zeeman interaction unless they both contain the same M_J component. Ignoring higher order effects which can further admix the Kramers doublets, since they are expected to be small, one can see that $\langle \pm\frac{7}{2} | H_{zeeman\,\parallel} | \pm\frac{5}{2} \rangle$ and $\langle \pm\frac{3}{2} | H_{zeeman\,\parallel} | \pm\frac{1}{2} \rangle$ are both zero.

Another 'anomaly' of this low-field resonance was observed when the experimental microwave frequency was changed. At room temperature and $\theta = 90°$, the 'intra-doublet' resonances in Cm^{3+}:$LuPO_4$ all shifted upfield as expected when the microwave frequency was increased, resulting in more or less the same g-values. The low-field resonance, however, shifted to a lower field —— it occurred at 550 G at a microwave frequency of 34.445 GHz but moved to 485 G at 34.906 GHz. Parallel to the opposite temperature dependence in the two crystal systems, this low-field transition in Cm^{3+}:YPO_4 showed an upfield shift with increasing microwave frequency. This 'inter-doublet' transition decreased in intensity relative to the $|\pm\frac{5}{2}\rangle$ resonance as the temperature was lowered, suggesting that it arose from an excited state. Otherwise, little information concerning the ordering and energies of these doublets can be inferred from these results.

Unexpectedly small and coincidental with the Q-band frequency, this 'inter-doublet' energy separation can be most sensitively probed by EPR. It is also certain that some of the other observed but unassigned Q-band resonances at high-field are transitions of the same nature.

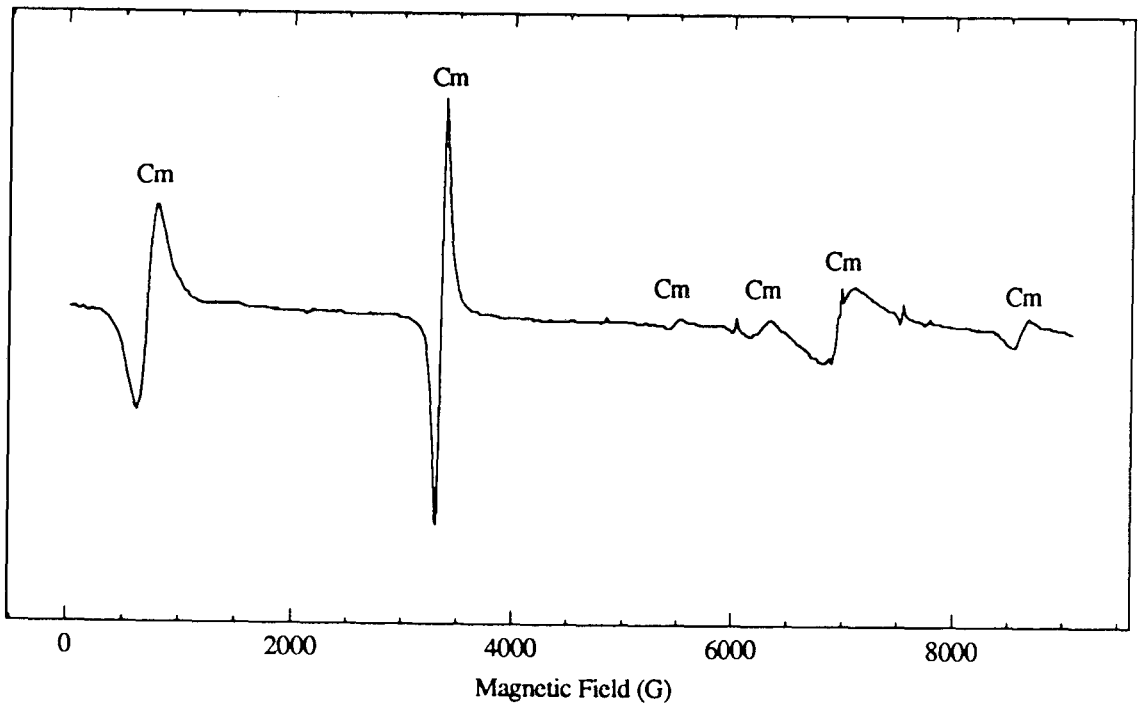

FIGURE 2.4 Q-Band EPR spectrum of Cm^{3+}:LuPO4 showing six Cm resonances.

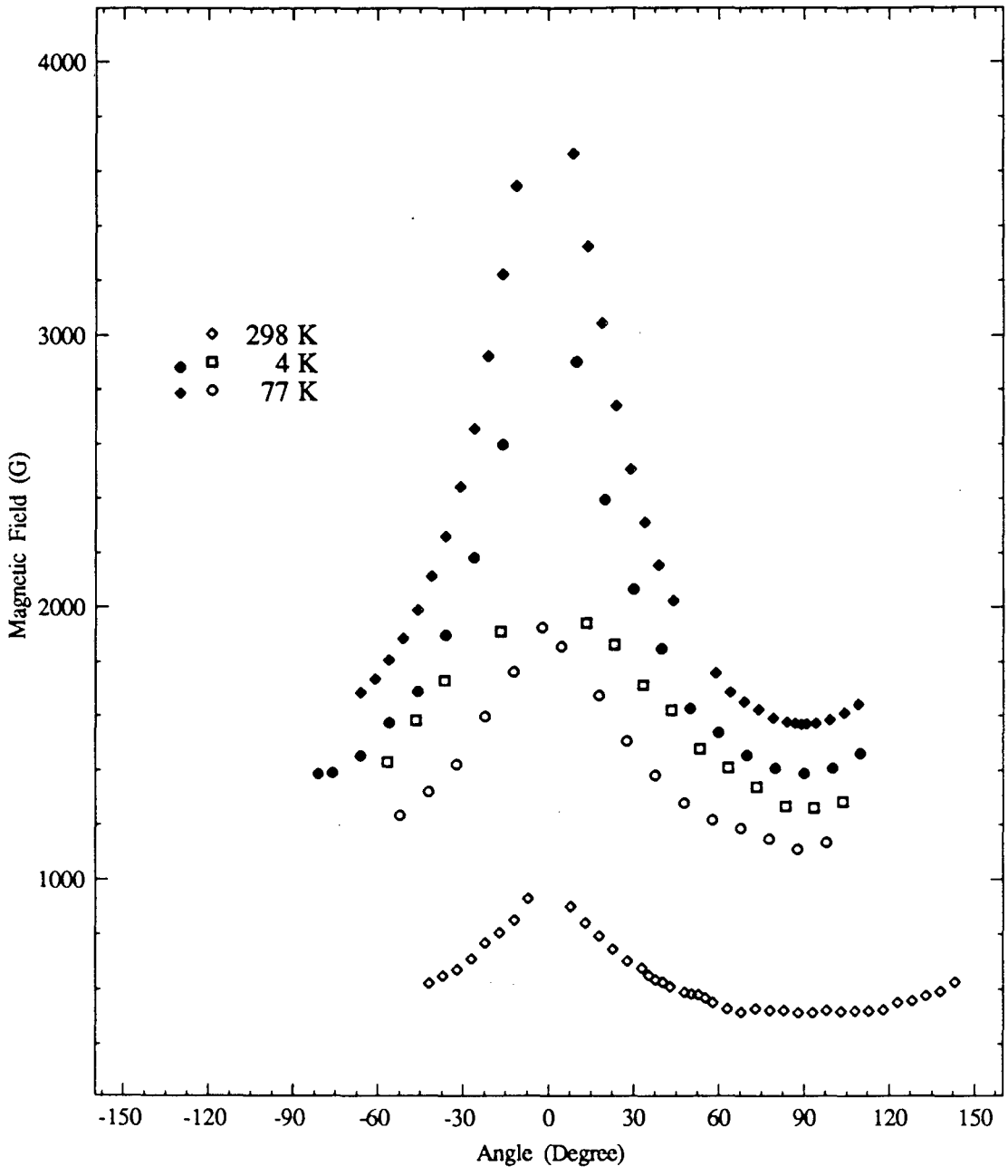

FIGURE 2.5 Angular and temperature dependence of the Q-Band EPR low-field transitions in Cm^{3+}:$LuPO_4$ (open symbols) and Cm^{3+}:YPO_4 (solid symbols). Microwave Frequency = 34.885 GHz.

2.4.3 Temperature Dependence Studies

A good deal of information can be derived from an analysis of the intensity and peak shape of a resonance line. The integrated area under a resonance line is proportional to the number of spins while the lineshape provides insight about the relaxation mechanism. Since more than one line can be assigned as due to Cm^{3+} in the observed spectra, an analysis of their temperature dependence may give information on the energy ordering of the Kramers doublets and, more importantly, help assign the low-field Q-band resonance. A series of spectra were then recorded of Cm^{3+}:$LuPO_4$ from 10 K to 300 K at an interval of ≈ 50 K with the crystal *c*-axis aligned parallel to the magnetic field.

In order for a lineshape analysis to be meaningful, distortion of the spectrum either by saturation or overmodulation has to be avoided. These conditions were satisfied experimentally by employing low microwave power and modulation amplitude. The microwave power employed was typically ≈ 5 mW and no appreciable change to the peak shape could be observed with a microwave power of up to 100 mW. The modulation amplitude used was 2 G, significantly smaller than the peak widths measured (20 to 50 G). Shown in Figure 2.6 is the $|\pm\frac{1}{2}\rangle$ doublet resonance together with least-squares fits to a Gaussian and a Lorenztian function. The resonance clearly has a Lorenztian lineshape and this suggests that inhomogeneous line-broadening is not important. This is expected since the concentration of Cm^{3+} in the crystal is known to be low and most of the contributions to inhomogeneous line-broadening such as i) difference in crystal-field seen by the central ions due to crystal imperfections and ii) dipole interactions between spins with different Lamour frequencies are minimized. Gradual broadening and transformation of the EPR lineshape from Lorentzian to Gaussian as the concentration of the paramagnetic ion is increased has been observed [19]. Broadening of lines due to radiation damage was found to be important in crystals doped with $^{243,244}Cm$ but it was not noticeable with ^{248}Cm.

The intensity I of a resonance line n at temperature T is a function of the transition probability P and the population X of the Zeeman level involved (2.11). The population follows the Boltzmann distribution and the transition probability can be calculated only with a detailed knowledge of the wavefunctions; they are not known. However, if the assumption is

made that the wavefunctions do not show much change over the experimental temperature range (i.e. that the energy of the crystal-field levels and the transition probability are independent of temperature), then Equation (2.11) can be rewritten as (2.12) and the intensity dependence on transition probability is removed. Little information on the temperature dependence of crystal-field is available; yet the fairness of this assumption is judged in the present case by whether the low-field Q-band line can be assigned based on the resulting information. In should also be noted that ΔE_{12} in (2.12) is actually the energy difference between the lower Zeeman levels of the doublets involved, but it is found to have the same value as the zero-field energy between the doublets when $\theta = 0$.

$$I_n(T) \propto P_n(T) X_n(T) \tag{2.11}$$

$$\frac{\left(\frac{I_1}{I_2}\right)_T}{\left(\frac{I_1}{I_2}\right)_{T'}} = \frac{\left(\frac{X_1}{X_2}\right)_T}{\left(\frac{X_1}{X_2}\right)_{T'}} = e^{-\left(\frac{\Delta E_{12}}{kT} - \frac{\Delta E_{12}}{kT'}\right)} \quad where \quad \begin{array}{l} \Delta E_{12} = E_1 - E_2 \\ k = Boltzmann\ constant \end{array} \tag{2.12}$$

Temperature	$\lvert\pm\frac{5}{2}\rangle$	$\lvert\pm\frac{3}{2}\rangle$	$\lvert\pm\frac{1}{2}\rangle$
15 K	1.0	1.318	7.515
85 K	1.0	2.127	13.321
150 K	1.0	2.217	14.177

TABLE 2.4 Measured Relative Intensities of the Resonances at Various Temperature (Intensity of $\lvert\pm\frac{5}{2}\rangle$ Doublet Normalized to 1.0 for Each Temperature)

Listed in Table 2.4 are representative values of the measured intensities of the three resonances at various temperatures. Different integration methods can be used for determining the intensities and integrating the experimental line twice should give the most accurate result. It was found, however, that integrating the best-fit Lorentzian function gave essentially the same

result, reflecting again the goodness of the Lorentzian fit. By Equation (2.10), the energy difference between the $|\pm\frac{5}{2}\rangle$ and $|\pm\frac{3}{2}\rangle$ states is found to be 5.82 ± 1.51 cm^{-1} while that between the $|\pm\frac{3}{2}\rangle$ and $|\pm\frac{1}{2}\rangle$ states is 1.12 ± 0.41 cm^{-1}. Without making further assumptions, no information can be obtained for the energy difference between the $|\pm\frac{7}{2}\rangle$ and $|\pm\frac{5}{2}\rangle$ states; nevertheless, these results, coupled with its temperature dependence are good evidence that the low-field resonance is a transition between the $|\pm\frac{3}{2}\rangle$ and $|\pm\frac{1}{2}\rangle$ doublets. This assignment and others are examined further with the other results in a more detailed analysis.

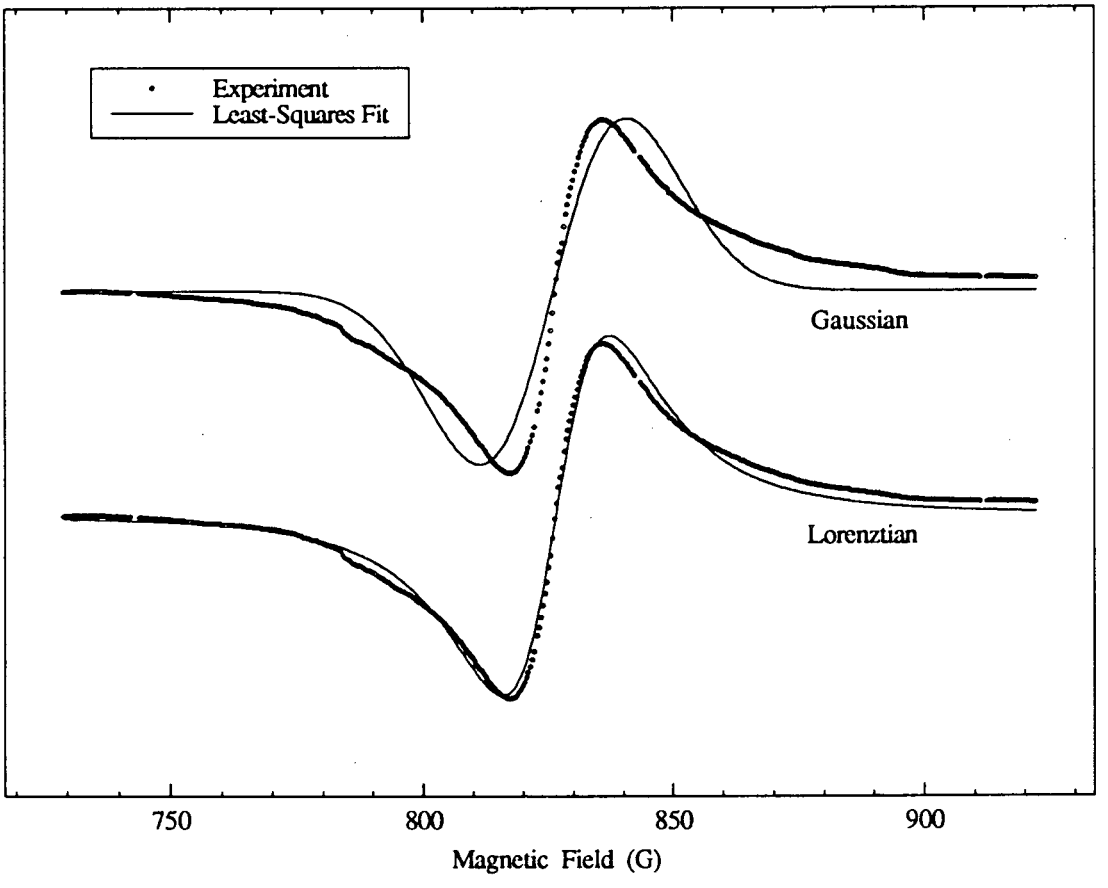

FIGURE 2.6 Least-squares fit to the $|\pm\frac{1}{2}\rangle$ doublet resonance. Microwave Frequency = 9.232 GHz. Temperature = 15 K and $\theta = 90°$.

2.5 Analysis and Discussion

Although the low-field Q-band resonance can now be assigned with some confidence as an 'inter-doublet' transition between $|\pm\frac{3}{2}\rangle$ and $|\pm\frac{1}{2}\rangle$, there are four different ways in which this can be done, i.e. from either of the two Zeeman levels of the lower doublet to either of the two Zeeman levels of the upper doublet. In theory, with knowledge of the wavefunctions in Section 2.4.1 and the zero-field energies from 2.4.3, one can diagonalize the 4×4 perpendicular Zeeman interaction matrix of the doublets involved or preferably the 8×8 matrix of the $J = 7/2$ manifold (in which case the energy between $|\pm\frac{7}{2}\rangle$ and $|\pm\frac{5}{2}\rangle$ was treated as a variable and assigned trial values). In practice, however, it was found that the zero-field energies from Section 2.4.3 are not precise enough so that all four assignments are equally likely. Recall that this transition occurs at very low field where the Zeeman levels of a doublet are very close together in energy.

Another approach is to least-squares fit all the available data to the spin-Hamiltonian (2.7) which diagonalizes simultaneously both the Zeeman and the crystal-field interactions. It was found that when only the 'intra-doublet' transitions were used in the fitting, the fitting normally did not converge. With the inclusion of the 'inter-doublet' transition, however, the fitting did converge to give an unique set of parameters. This can be expected since assigning an 'inter-doublet' transition effectively fixes the energy difference between two doublets at ≈ 1.2 cm^{-1} and severely limits the choice and variation of the parameters. The best fit was obtained with the 'inter-doublet' transition assigned as between the upper Zeeman level of the $|\pm\frac{3}{2}\rangle$ doublet and the lower Zeeman level of the $|\pm\frac{1}{2}\rangle$ doublet; the parameters are given in Table 2.5 together with the calculated zero-field energies. Selected fit to experimental data are shown in Figure 2.7. The other three assignments resulted in convergence but much poorer fits. Nevertheless, parameters obtained from these fits agree to within 20 % with the 'best-fit' parameters and the calculated zero-field energies are within $\pm$ 2 cm^{-1} when compared to the 'best-fit' set. These energies are listed in Table 2.6 for comparison; we shall only refer to the 'best-fit' parameters and energies for the rest of the discussion.

The calculated zero-field energies at 10 K are 1.4 cm^{-1} and 6.2 cm^{-1} for the $|\pm\frac{3}{2}\rangle \rightarrow |\pm\frac{1}{2}\rangle$ and $|\pm\frac{5}{2}\rangle \rightarrow |\pm\frac{3}{2}\rangle$ splittings respectively, in good agreement with the results obtained from the

Temperature		298 K	77 K	4 K
g		1.925	1.925	1.925
b_2^0 (cm^{-1})		–0.741	–0.910	–0.936
b_4^0 (cm^{-1})		0.074	0.056	0.051
b_6^0 (cm^{-1})		0.056	0.059	0.060
b_4^4 (cm^{-1})		–1.036	–1.347	–1.429
b_6^4 (cm^{-1})		–0.146	–0.608	–0.645
Zero-Field Energies (cm^{-1})	$\lvert\pm\frac{1}{2}\rangle$	9.3	11.3	11.4
	$\lvert\pm\frac{3}{2}\rangle$	8.0	9.9	10.0
	$\lvert\pm\frac{5}{2}\rangle$	2.4	3.8	3.8
	$\lvert\pm\frac{7}{2}\rangle$	0.0	0.0	0.0

TABLE 2.5 Spin-Hamiltonian Parameters and Calculated Zero-Field Energies of Cm^{3+}:$LuPO_4$ at Various Temperatures

Inter-doublet Transition assigned as	Zero Field Energy (cm^{-1})		
$5 \rightarrow 7$	4.09	8.11	9.28
$5 \rightarrow 8$	2.32	7.92	9.23
$6 \rightarrow 8$	4.25	8.09	9.23

5 = lower Zeeman level of $\lvert\pm\frac{3}{2}\rangle$ 7 = lower Zeeman level of $\lvert\pm\frac{1}{2}\rangle$
6 = upper Zeeman level of $\lvert\pm\frac{3}{2}\rangle$ 8 = upper Zeeman level of $\lvert\pm\frac{1}{2}\rangle$

TABLE 2.6 Zero-Field Splittings of Cm^{3+}:$LuPO_4$ with Various 'Inter-Doublet' Transition Assignments at Room Temperature

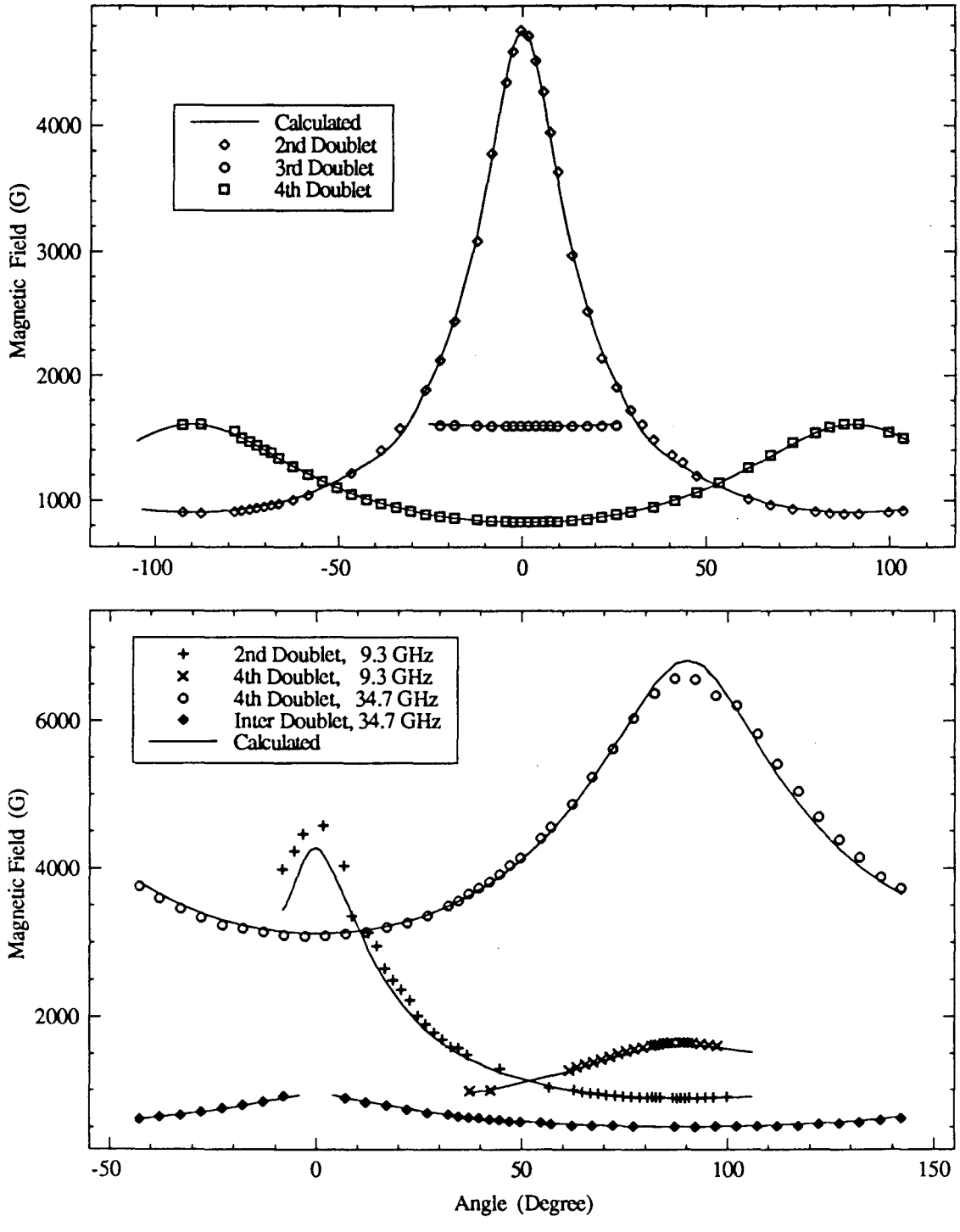

FIGURE 2.7 Experimental and fitted dependence of the EPR spectra as a function of the angle between the crystallographic *c* axis and the magnetic field. (Top) Microwave frequency = 9.235 GHz, 77K and (Bottom) Microwave frequency = 34.742 GHz, room temperature.

temperature dependence study; the calculated $|\pm\frac{7}{2}\rangle \rightarrow |\pm\frac{5}{2}\rangle$ splitting is 3.8 cm^{-1}. Shown in Figure 2.8 is the calculated Zeeman energy levels of the ground manifold of Cm^{3+}:$LuPO_4$ when the magnetic field is perpendicular to the crystal *c* axis; experimentally observed EPR transitions are also indicated. The large temperature dependence of the low-field transition described in Section 2.4.2 can now easily be explained by referring to Figure 2.8. The calculated $|\pm\frac{3}{2}\rangle \rightarrow |\pm\frac{1}{2}\rangle$ splitting is 1.4 cm^{-1} and 1.3 cm^{-1} at 10 K and 298 K respectively. The difference of 0.1 cm^{-1} is a large one in the microwave frequency regime, consequently a large shift of the resonance field with temperature was observed. Increasing the microwave frequency shifts the resonance downfield as expected from the diagram.

Pfister et al. [20] have tried to interpret the temperature dependence of the ZFS of Mn^{2+} in LiCl and NaCl using a model which couples the lattice vibration with the metal center and found that the spin-Hamiltonian parameters could be fitted to an equation of the form

$$D(T) = D(0) - A\left(\coth\frac{B}{T} - 1\right) \tag{2.13}$$

where D is the spin-Hamiltonian parameter (or the ZFS), A and B are constants characteristic to the system, and T is the temperature. The same physical model could not be used to explain the temperature dependence of ZFS of Gd^{3+} doped in YRO_4, $ScRO_4$ and $LuRO_4$ (R = V, P, As), although Equation (2.13) still gave a good fit to the experimental data which showed a 10–20 % increase in b_2^0 and the ZFS as the temperature was lowered from 300 K to 4 K [21]. Data can only be obtained at three different temperatures for the present case; however, they do show the trend as predicted by (2.13) and the same order of magnitude increase as the temperature is lowered. The origin of this increase is not well understood but the local anisotropy around the central ion is known to make a contribution. A rough measure of the local anisotropy is the *c/a* ratio of the unit cell which is correlated with the parameter b_2^0. Thermal expansion of the unit cell of YPO_4, YVO_4 and presumably $LuPO_4$ has been known to be anisotropic [22], the larger *c/a* ratio at low temperature results in a larger b_2^0 and ZFS. Incidentally, the temperature dependence of the thermal expansion coefficient and other processes such as thermal saturation in solids can also be described by a hyperbolic cotangent function and so care must be taken in

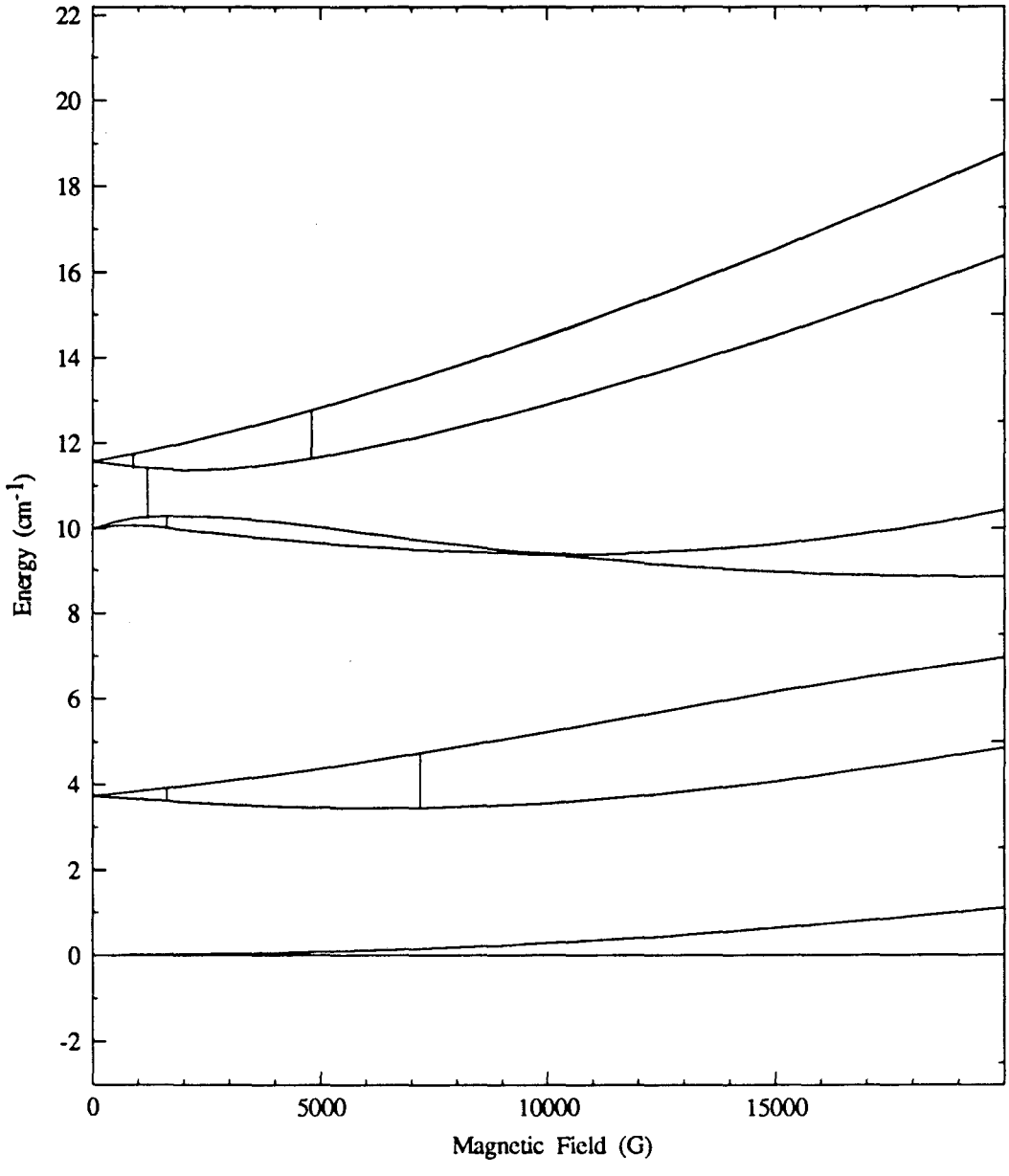

FIGURE 2.8 Calculated Zeeman energy levels and the observed X (0.3 cm^{-1}) and Q (1.2 cm^{-1}) Band EPR transitions with the magnetic field perpendicular to the crystallographic *c* axis at 77 K.

interpreting (2.13). As the ZFS of an S-state ion is believed to result from more than one mechanism, the temperature dependence of ZFS is also expected to have contributions from different processes. It can only be remarked that ZFS in Cm^{3+}:$LuPO_4$ shows qualitatively the same temperature dependence as in Gd^{3+}:$LuPO_4$.

As mentioned in Section 2.1, Cm^{3+}:$SrCl_2$ represents the only system where the total Cm^{3+} ZFS is known; its spin-Hamiltonian parameters are listed in Table 2.7 together with those of Gd^{3+}:$SrCl_2$ and Gd^{3+}, Cm^{3+}:$LuPO_4$. Only two parameters are necessary to describe the cubic site symmetry in $SrCl_2$. Figure 2.9 is an energy diagram comparing the ZFS of the four systems. A good deal of effort has been put into the study of the ZFS of Gd^{3+} both experimentally and theoretically; many physical processes have been found to be important as origins of the ZFS. What often results is a confusing picture of many competing and often canceling contributions that arise from a large variety of mechanisms such that even very simple generalizations are difficult to make. With the little data on Cm^{3+} at hand, it is unreasonable, if not impossible, to discuss them in terms of the specific physical processes. We shall therefore primarily point out some of the more relevant systematics about the four systems. The reader is referred to a number of review articles for a discussion of the many different mechanisms proposed [23].

Apart from b_4^0 and b_4^4 in $LuPO_4$, the spin-Hamiltonian parameters have the same signs for both ions and the energy orderings of their electronic states are identical in both crystals (Fig 2.9). The total ZFS of Cm^{3+} are much larger than those of Gd^{3+} and this is believed to be due to the larger intermediate coupling found in Cm^{3+}, as already discussed in Section 2.3. A comparison of these ZFS with any excited $J = 7/2$ splitting should be revealing in this respect; unfortunately no experimental splitting of any excited $J = 7/2$ manifold is known (*vide infra*). The ratios of the total ZFS reflect the ratios of the dominant parameters; and in the case of $LuPO_4$, this ratio of ≈ 12 is much smaller than those found in $SrCl_2$ (384) and the others listed in Table 2.2. Hyperfine constants found for Cm^{3+}:$SrCl_2$ and Cm^{3+}:$LuPO_4$ are very similar, a result that is normally taken as an indication of the same degree of covalent bonding. While the fourth- and sixth-order parameters for the two systems are roughly comparable, no comparison is possible for b_2^0; the b_2^0 value found for Cm^{3+}:$LuPO_4$ is unexpected in the sense that it results in a very small ZFS. While the total ZFS of Gd^{3+} increases by a factor of > 10 in going from

M^{3+}:$SrCl_2$	b_4	b_6	Total ZFS
[a]Cm^{3+}	-660×10^{-3}	-77.0×10^{-3}	20.43
[b]Gd^{3+}	-1.66×10^{-3}	-4.25×10^{-6}	0.0532
Cm^{3+}/Gd^{3+}	398	18117	384

M^{3+}:$LuPO_4$	b_2^0	b_4^0	b_4^4	b_6^0	b_6^4	Total ZFS
Cm^{3+}	-740×10^{-3}	74×10^{-3}	-1.036	56×10^{-3}	-146×10^{-3}	9.3
[c]Gd^{3+}	-63×10^{-3}	-0.3×10^{-3}	2.1×10^{-3}	0.02×10^{-3}	-0.09×10^{-3}	0.76
Cm^{3+}/Gd^{3+}	11.7	(–)246	(–)486	2800	1622	12.2

TABLE 2.7 Spin-Hamiltonian Parameters and Total ZFS (in cm^{-1}) for Gd^{3+} and Cm^{3+} in $SrCl_2$ and $LuPO_4$ (Data for $SrCl_2$ are at 4 K and those for $LuPO_4$ are at room temperature. [a] From Ref. 5, [b] from Ref. 24, [c] from Ref. 8)

$SrCl_2$ to $LuPO_4$, that of Cm decreases. Kolbe *et al.* [3] have pointed out that the $\Gamma_6 \rightarrow \Gamma_8$ splittings (and presumably the total ZFS) are in general an inverse function of the cell dimensions (see Table 2.2) which appears to agree qualitatively with an ionic point charge model. Changing the ligand from the monovalent halide to the divalent oxide increases the splittings further. It was also argued that since the Cm^{3+} splittings are thought to be dominated by intermediate coupling effects, there is no exception found for this generalization whereas the reversal of the magnitudes of the Gd^{3+} splittings in CeO_2 and ThO_2 is not understood. The presently determined total ZFS for Cm^{3+}:$LuPO_4$ is smaller than those found in CeO_2 and ThO_2 as expected (the cell dimenstions of $LuPO_4$ are a = 6.798 Å and c = 5.961 Å). However, the symmetry of the crystal-field is also likely to play a role into determining the size of the splittings and a more appropriate comparison is better made with systems with a

lower-than-cubic system; no such data are available. It is therefore of interest to determine if b_2^0 and the ZFS is proportionally small for Cm^{3+} in another low-symmetry host.

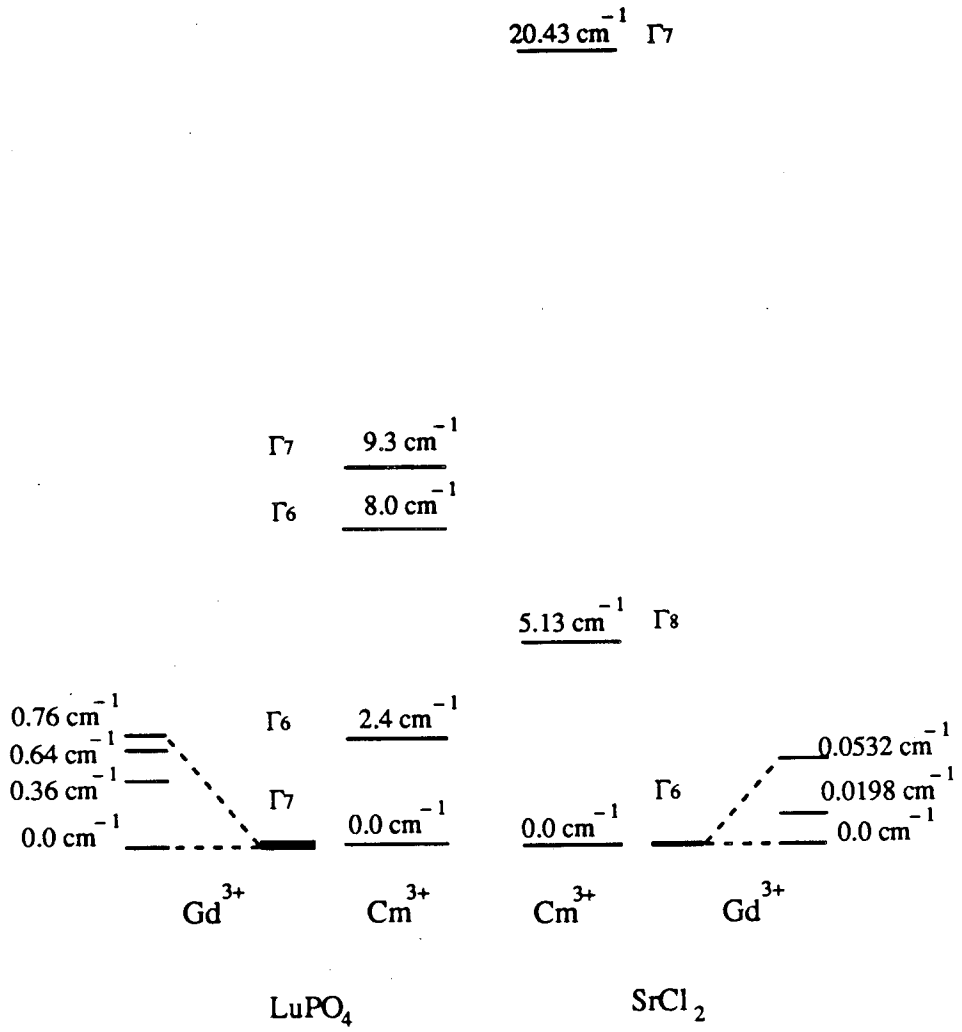

FIGURE 2.9 Schematic Energy Diagram of Zero-Field Splittings of Gd^{3+} and Cm^{3+} in $LuPO_4$ and $SrCl_2$. The energies of Cm^{3+}:$SrCl_2$ are at 4 K while the rest are at room temperature.

Any comment on the physical significance of the size of b_2^0 is speculative as even some of the most complete *ab initio* analyses on Gd^{3+} and Mn^{2+} have ended in puzzling results. For example, Wybourne has found that the major contributions to b_2^0 of Gd^{3+} arise from relativistic effect and an interaction which is first order both in crystal-field and spin-orbit coupling, but the calculated b_2^0 carries the wrong sign [23a]. Nevertheless, the correlation between the size of the total ZFS and the temperature at which EPR can be observed appears to be valid since both are consequences of the extent of the interaction between the *S*-state and the crystal-field. Thus EPR is detectable at 200 K in Cm^{3+}:$SrCl_2$ which has a relatively small ZFS whereas the first room temperature EPR of an actinide is observed in Cm^{3+}:$LuPO_4$ with an even smaller ZFS.

Although b_2^0 is still dominant in determining the total ZFS in Cm^{3+}:$LuPO_4$ as in Gd^{3+}:$LuPO_4$, the other parameters have become relatively more important. This can be seen qualitatively in Figure 2.9 where it is evident that the energy separations between the Kramers doublets in Gd^{3+}:$LuPO_4$ approach the axial symmetry limit of 3:2:1 more so than Cm^{3+}:$LuPO_4$ (when b_4^0 and b_6^0 are neglected, the separations between doublets are $-6b_2^0$:$-4b_2^0$:$-2b_2^0$). The relatively large values found for b_4^4 and b_6^4 in Cm^{3+} mix free ion states with $\Delta M_J = \pm 4$. The effect of this mixing is shown in the parallel Zeeman effect (Fig 2.10) in which *A* and *B* are the regions where admixed levels would cross each other if no mixing takes place. The gap between the repelling branches is determined by the magnitude of the off-diagonal matrix elements. In contrast, inclusion of these off-diagonal elements is found to be unnecessary for the axial molecule GdF_3 [25]. On a more quantitative basis, the increased importance of the fourth- and sixth-order parameters is obvious from the ratios of the Cm^{3+} parameters over the Gd^{3+} parameters in Table 2.7. This suggests that higher-order perturbation mechanisms are much more prominent in Cm^{3+} than in Gd^{3+}. This is not surprising as most higher-order effects involve excited electronic states and spin-orbit coupling and Cm^{3+} has both lower lying excited states and much larger spin-orbit coupling constant than Gd^{3+}. Unfortunately, there does not exist any simple way whereby the different effects can be isolated and studied individually.

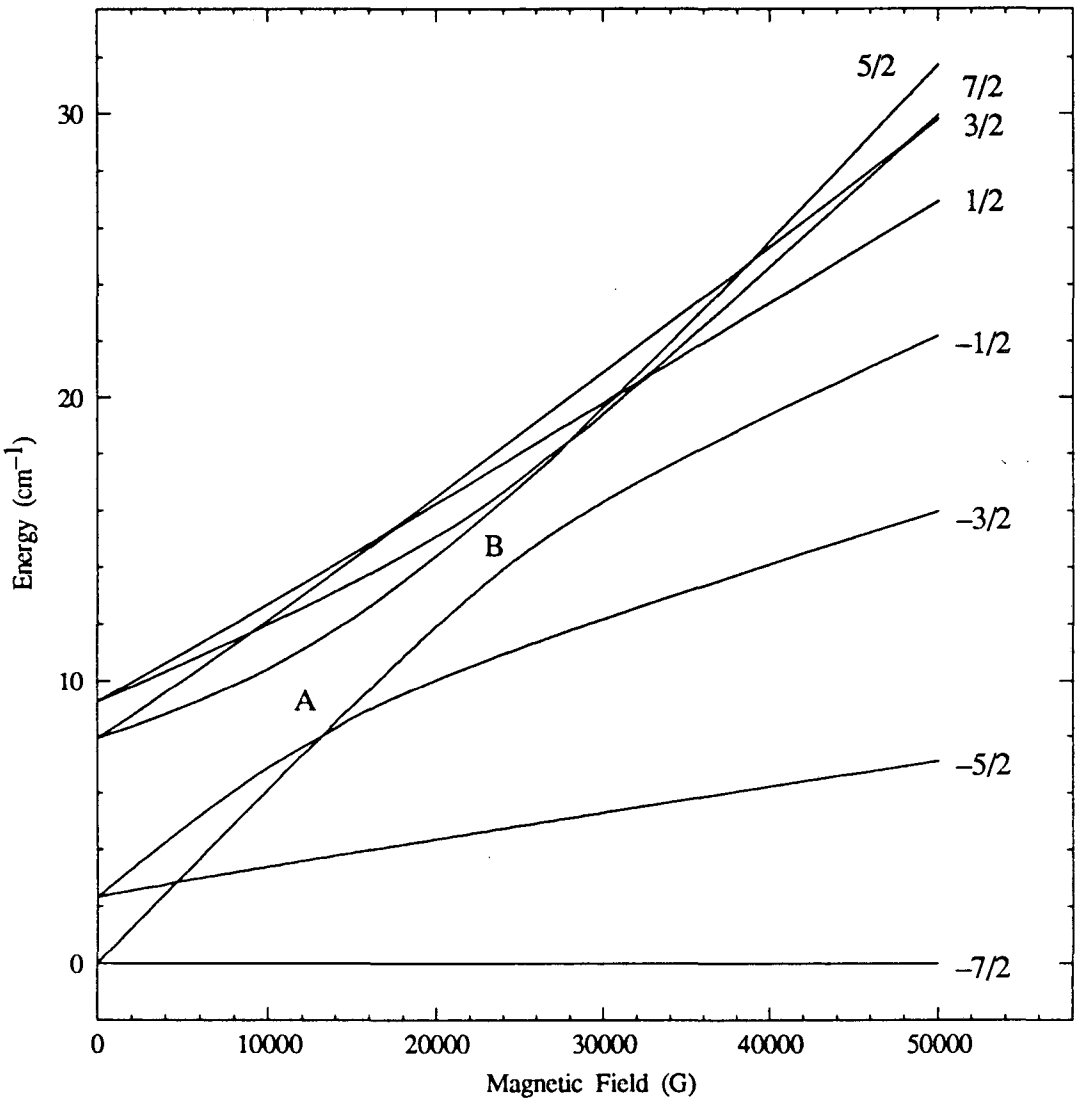

FIGURE 2.10 Calculated parallel Zeeman effect of Cm^{3+}:$LuPO_4$ at room temperature. Regions marked A and B are where the doublet $|\mp\frac{3}{2}\rangle$ crosses $|\pm\frac{5}{2}\rangle$ and $|\pm\frac{7}{2}\rangle$ crosses $|\mp\frac{1}{2}\rangle$ respectively if no mixing occurs.

2.6 Absorption and Fluorescence Spectra of Cm^{3+}:$LuPO_4$

Although EPR is in general a very sensitive technique, the accuracy of the measurements described in the previous sections is limited by the small number of transitions that can be detected and assigned. The total ZFS in Cm^{3+}:$LuPO_4$ of ≈ 10 cm^{-1} and the energy separations between Kramers doublets of 1 – 7 cm^{-1} are easily within the resolution limit of optical spectroscopy. Optical spectroscopy of lanthanides is characterized by the sharpness of the absorption and emission lines, typical $f \rightarrow f$ transitions have linewidths of 0.01 to 0.5 cm^{-1}. Linewidths found in actinides are considerably broader. As discussed in Section 2.4.3, inhomogeneous line-broadening is normally unimportant in a dilute crystal, performing the experiments at low temperature (4 to 77 K) minimizes the homogeneous linewidths and a resolution of 0.1 to 1 cm^{-1} can be achieved for actinides. Optical methods were therefore used to confirm the EPR results from above. Moreover, if information can be obtained on the crystal-field of the excited electronic states of Cm^{3+}:$LuPO_4$, a comparison of the two crystal-fields may be revealing on the ZFS mechanisms.

Optical methods as applied to the present case are not without their problems. While a small concentration of impurity ions reduces the inhomogeneous linewidths, it limits the sensitivity of the measurement; $f \rightarrow f$ transitions are formally forbidden and do not have large oscillator strengths. Another complication in actinide spectroscopy is that selection rules are very often violated, making assignments difficult.

In D_{2d} symmetry, all half-integral J manifolds of the f^7 configuration decompose into $(2J+1)/2$ Kramers doublets with labels of Γ_6 or Γ_7. Selection rules are the same for both absorption and emission spectroscopies and the allowed transitions are:

	Γ_6	Γ_7
Γ_6	σ	σ, π
Γ_7	σ, π	σ

where π is the polarization of the electric field along the z direction (crystal c axis, $E \parallel c$) and σ is the polarization of the electric field along the x (or y) direction ($E \perp c$). The ground state was determined to be Γ_7 from above with the highest excited doublet of Γ_7 only 9.3 cm^{-1} away at room temperature; so population of and absorption arising from every doublet of the ground manifold is expected.

2.6.1 Absorption Spectra of Cm^{3+}:$LuPO_4$

A list of measured energy levels of Cm^{3+}:$LuPO_4$ can be found in Appendix 2.A.

In general the measured spectra at 4 K showed relatively sharp (FWHM of 1–2 cm^{-1}) but very weak lines. The weak intensity limited the accuracy and precision of the measurement. Fewer lines than theoretically predicted could be detected; below 24,000 cm^{-1}, only nine out of eighteen expected transitions were located and only four lines were detected above 24,000 cm^{-1}. This most likely is caused by the low concentration of Cm^{3+} in the crystals. The absorption lines do not show good polarization characteristics such that their assignments are difficult and a consistent set of crystal-field parameters cannot be obtained. Additionally, the total splittings of the excited $J = 7/2$ manifolds could not be determined as only two crystal-field states could be found for both the $^6D_{7/2}$ and $^6I_{7/2}$ free-ion states.

Many of the observed transitions occurred in groups of two or three, spread over a region of < 10 cm^{-1}, instead of a single line and these fine structures undoubtedly arose from the ground manifold of Cm^{3+}; splittings of excited states by the crystal-field normally are in the order of tens to hundreds of wavenumbers. With the knowledge of the ZFS determined from the EPR data, it is straightforward to interpret these lines. Of the thirteen transitions recorded, all but three of the weakest exhibited fine structures and most showed a splitting of 3.2–3.8 cm^{-1}, a second splitting of 7.4–10.0 cm^{-1} was also observed. None showed the quartet structure as expected. The reason for the failure to observe a fourth line in the fine structure is probably due to a combination of i) the low population of the highest state of the ground manifold ii) the low probability of transitions arising from this state and iii) the broadness of the peak widths which cannot be resolved. Both the unpolarized spectra and polarized spectra

recorded at 77 K do not show much difference; those recorded at room temperature have much broader peak widths and most of the fine structures disappeared. While these fine structures are consistent with the ZFS determined by EPR, the associated uncertainties are rather large because of the low intensities of the transitions and information more precise than the EPR results could not be obtained.

2.6.2 Excitation Spectroscopy of Cm^{3+}:$LuPO_4$

Measurement of absorption spectra such as those in Section 2.6.1 is generally based on the determination of the absorption coefficient $\alpha(\omega)$ at frequency ω,

$$I_t(\omega) = I_o(\omega)\ e^{-\alpha(\omega)x} \tag{2.14}$$

where $I_o(\omega)$ is the incident spectral intensity and $I_t(\omega)$ is the spectral intensity transmitted through a path length x. When $\alpha(\omega)x$ is small, as is the case with a dilute crystal of Cm^{3+}:$LuPO_4$, (2.14) can be approximated as

$$I_t(\omega) \approx I_o(\omega)\ [1 - \alpha(\omega)x] \tag{2.15}$$

With a double-beam spectrometer, a reference beam with intensity $I_R(\omega) = I_o(\omega)$ is used such that

$$\alpha(\omega)x = \frac{[\ I_R(\omega) - I_t(\omega)\ ]}{I_R(\omega)} \tag{2.16}$$

It can therefore be seen that, in cases of very small $\alpha(\omega)x$, absorption spectroscopy measures a small difference of two large quantities and this severely limits its accuracy and sensitivity. Various techniques have been developed to improve upon this situation. One such technique involves directly monitoring the absorbed energy rather than the difference $(I_R - I_t)$. While $\alpha(\omega)$ is independent of the intensity of the incident radiation, the energy absorbed by the sample can

be increased by substituting a laser for a conventional light source. This energy can be converted into thermal energy which causes a rise in temperature and pressure which in turn can be detected by a microphone (photoacoustic spectroscopy), or it can decay radiatively and the fluorescence intensity measured as a function of the excitation frequency (excitation spectroscopy). The sensitivity of excitation spectroscopy is in practice limited by two factors: i) the ratio of decay rate by fluorescence to the total decay rate which may include radiationless decay, and ii) the collection efficiency of the fluorescence photons which are emitted in all directions. Under optimal conditions, an absorption of $\Delta I / I$ of 10^{-14} can be detected; a more realistic detection limit is 10^{-8} which is still far superior to that of classical absorption spectroscopy (an absorbance of 0.0001 corresponding to I_t / I_R of 10^{-4}). Figure 2.11 is a schematic diagram illustrating the processes of absorption, excitation and fluorescence.

Excitation spectroscopy is normally used to study line positions of excited states but there are two features about Cm^{3+}:$LuPO_4$ which make excitation spectroscopy suitable to probe its ground manifold. The total splitting of the ground manifold Cm^{3+}:$LuPO_4$ was determined to be ≈ 10 cm^{-1} from above; this relatively small splitting ensures that the higher states within the manifold are populated even at very low temperature. The fact that EPR of excited states could be observed at 4 K very nicely illustrates this point. A second feature about Cm^{3+} is that the first excited manifold is over 16,000 cm^{-1} above ground (the lowest crystal-field state of the manifold in Cm^{3+}:$LuPO_4$ is 16,528 cm^{-1}, see 2.A) and nonradiative decay from this manifold is unimportant. This feature does not only increase the quantum efficiency of the fluorescence which in turn increases the sensitivity of the measurement, it also significantly increases the lifetime of the excited state, resulting in narrower fluorescence linewidths and thus improving the resolution.

A tunable dye laser (Coumarin 487) pumped by an argon laser was used to provide the excitation from 19,500 to 21,000 cm^{-1}. The radiation was collected and focused onto the crystal which was kept at ≈ 10 K. The fluorescence intensity of the 16,528 cm^{-1} line was monitored while the excitation frequency was scanned. The resulting spectrum is shown in Figure 2.12. Three relatively sharp lines plus a very weak shoulder were observed. The three lines correspond to the absorption spectrum at $\approx 19,770$ cm^{-1} which is also included in Figure 2.12 for comparison. The shoulder, which was not observed in the less sensitive absorption

spectrum, corresponds to the absorption originating from the highest doublet of the ground manifold. Its small intensity is probably due to a very small transition probability rather than the low population as the absorption arising from the next highest doublet (which is only 1.4 cm^{-1} away) is much stronger. The splittings of the ground manifold are measured to be 0.0, 3.6, 8.5 and 9.9 cm^{-1}, compared to 0.0, 3.8, 10.0 and 11.4 cm^{-1} measured by EPR at 4 K.

A second peak was found at an excitation frequency of 20,180 cm^{-1}. This peak is very weak and broad but appears to have the same overall width ($\approx$ 10 cm^{-1}) and profile as the group at 19,775 cm^{-1}. As it does not correspond to any line in the absorption spectrum (see 2.A) or reveal any fine structrure, it was not studied further.

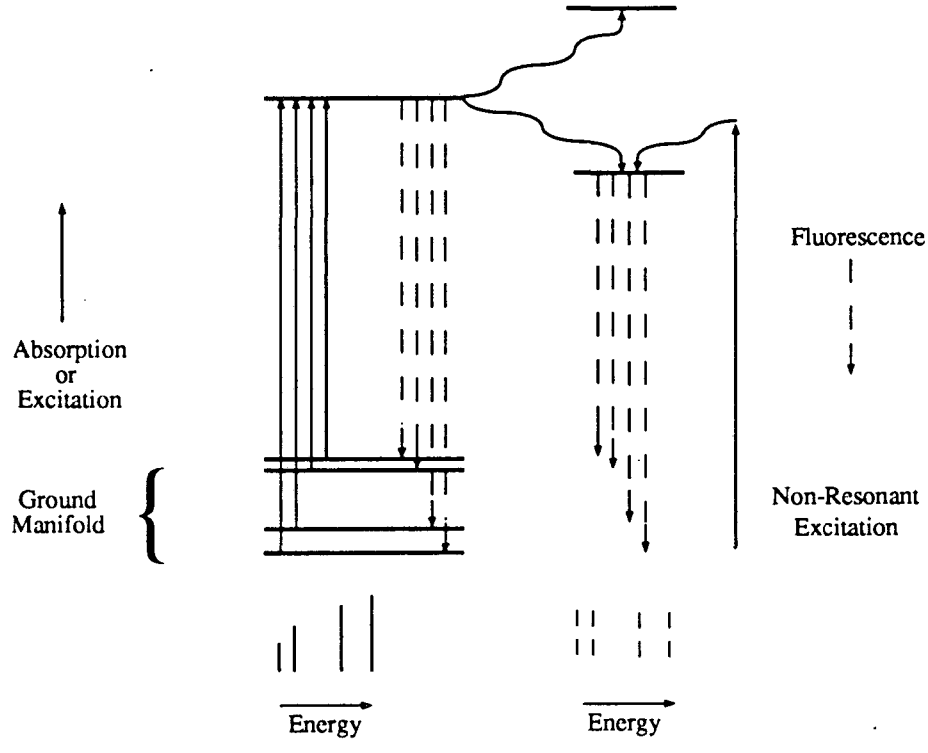

FIGURE 2.11 Schematic diagram of the absorption, excitation and fluorescence processes. Wavy lines indicate non-radiative decay. At the bottom of the diagram are profiles of the absorption/excitation spectra (solid line) and the fluorescence spectrum (dashed line) assuming equal fluorescence branching ratios to every crystal-field state of the ground manifold. The intensity difference in the excitation spectrum is due to population difference.

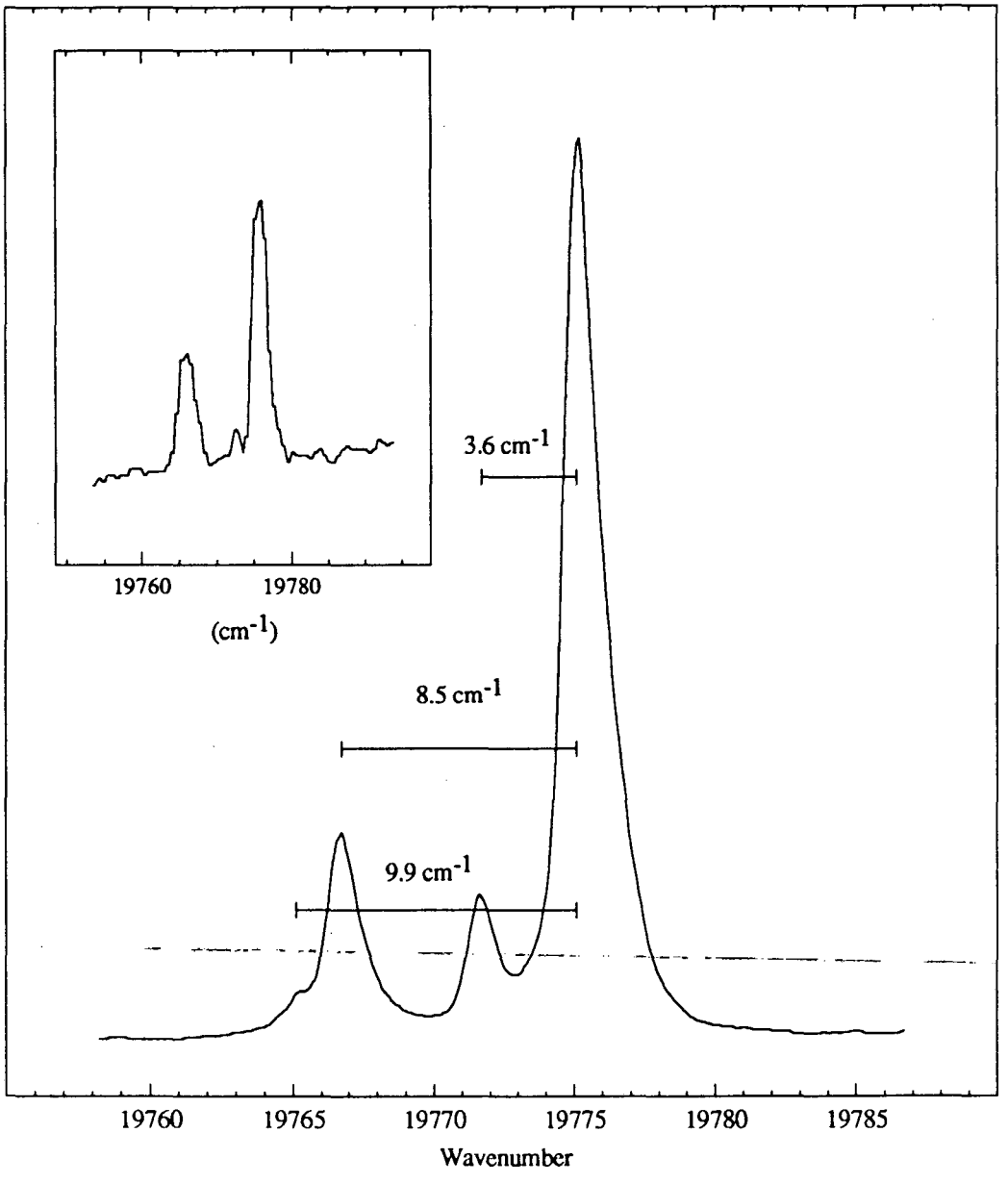

FIGURE 2.12 Excitation Spectrum of Cm^{3+}:$LuPO_4$ at ≈10 K. The x-axis is the excitation frequency and the signal represents fluorescence intensity at 16,528 cm^{-1}. No polarization was used and the peakwidths (FWHM) measured are, from left to right, 1.5 cm^{-1}, 1.2 cm^{-1} and 1.2 cm^{-1}. Shown in the inset is the absorption spectrum in the same region.

2.6.3 Fluorescence Spectra of Cm^{3+}:$LuPO_4$

Fluorescence spectra of Cm^{3+}:$LuPO_4$ were obtained with an argon ion laser providing the excitation; the emission photons were collected at 90° to the laser photons and analyzed with a SPEX 1403 double monochromator. Figures 2.12 and 2.13 show these spectra and the results are summarized in Table 2.6.

	σ-Polarization		π-Polarization	
Excite w/496 nm	16528.4 cm^{-1} (s)		16528.4 cm^{-1} (s)	
(20,158 cm^{-1})	16525.0 (w)	Δ = 3.4 cm^{-1}	16525.0 (w)	Δ = 3.4 cm^{-1}
	16519.6 (s)	8.8	16519.6 (m)	8.8
	16575.4 (br)			
	19775.7 cm^{-1} (w)		19775.4 cm^{-1} (s)	
	19772.2 (w)	Δ = 3.5 cm^{-1}	19772.2 (w)	Δ = 3.2 cm^{-1}
	19767.5 (s)	8.2	19767.3 (m)	8.1

TABLE 2.6 Fluorescence Spectra of Cm^{3+}:$LuPO_4$ at 10 K

The spectra (Fig 2.13) obtained are reminiscent of the absorption peaks; they are in general very weak and do not show good polarization characteristic. With the exception of the peak at 16,575.4 cm^{-1}, they all show splittings of 3.2–3.5 cm^{-1} and 8.1–8.8 cm^{-1} but again no quartet structure is apparent. Consequently, similar to the absorption spectra, they are consistent with the EPR results but they are not useful for a more precise determination of the splittings of the ground manifold.

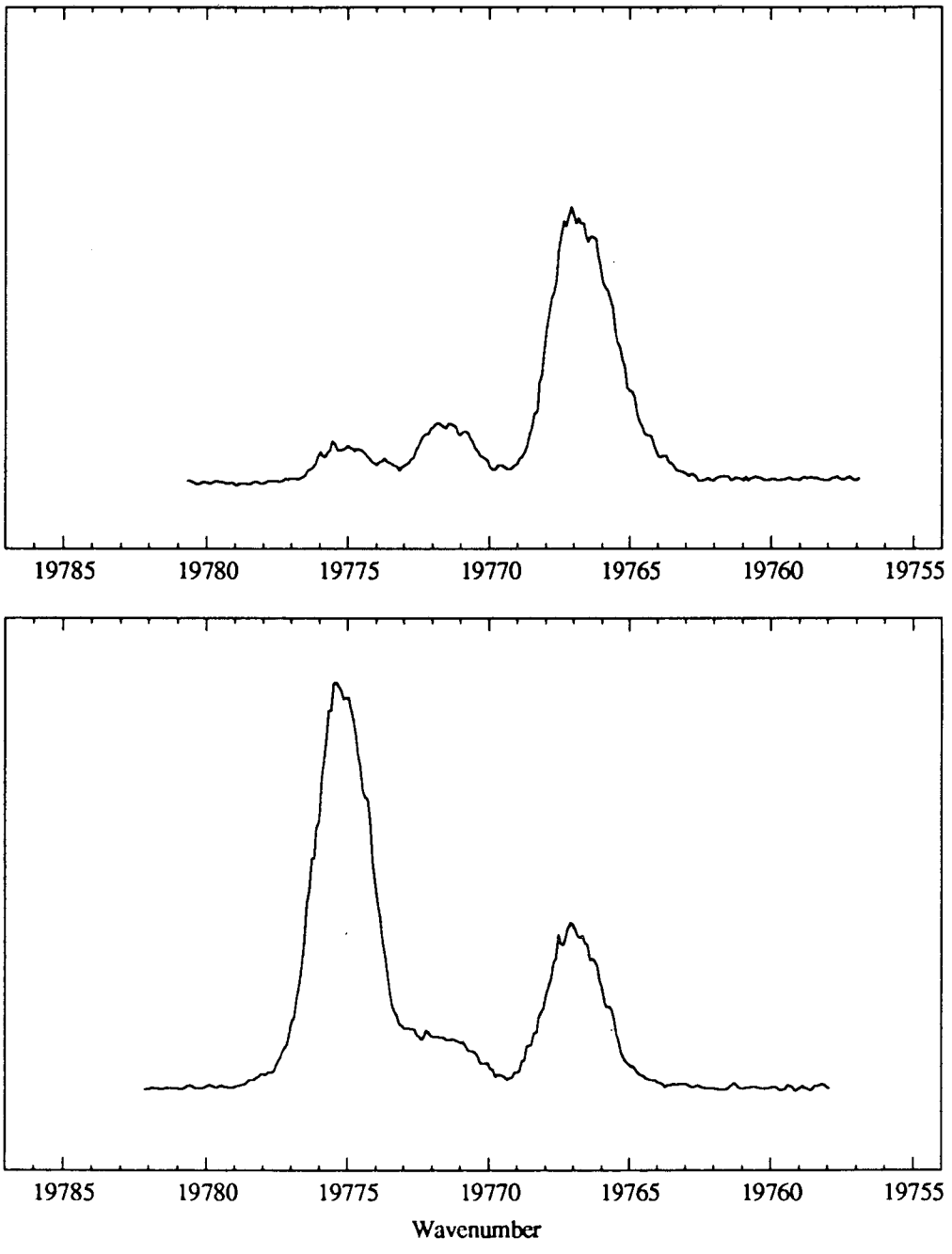

FIGURE 2.13 Fluorescence spectra of Cm^{3+}:$LuPO_4$ at 10 K using the 496 nm line as excitation. The σ-spectrum is on top and the π-spectrum is at the bottom.

2.7 EPR of Pu^{3+}:$LuPO_4$ and Cf^{3+}:$LuPO_4$

The most extensive crystal-field study of Cm^{3+} was performed on Cm^{3+}:$LaCl_3$. It was found that, similar to Gd^{3+}:$LaCl_3$, crystal-field parameters for the neighboring actinides (lanthanides) could be used to give satisfactory fit to the observed energy levels in Cm^{3+}:$LaCl_3$ (Gd^{3+}:$LaCl_3$). Interestingly, the calculated total ZFS for the ground S-state using the Bk^{3+}:$LaCl_3$ parameters is 7.5 cm^{-1}, although the wrong ground state was predicted [26]. The ground state was found experimentally to be a $|\pm\frac{1}{2}\rangle$ doublet [2], but the ZFS is not known inspite of evidence suggesting that states are located at 0.9 cm^{-1} and 1.6 cm^{-1} [27]. While the calculated splitting of 7.5 cm^{-1} cannot be assigned too much significance because i) of the large uncertainties associated with the determined parameters and ii) the parameters are determined for a large energy range of over 30,000 cm^{-1}, it raises the question: how well can the ZFS of the ground S-state of Cm^{3+} be described by the crystal-field of the excited states (which is principally electrostatic in origin compared to the ground S-state crystal-field) through intermediate coupling? Recent calculations have shown that in some instances the ZFS of the ground state of Gd^{3+} can be explained by considering only the crystal-field of the excited states. Specifically, the ZFS of the Gd^{3+} S-state was found to be a reflection of the crystal-field splitting of the excited $^6P_{7/2}$ manifold [28]. It is expected that crystal-field parameters of excited states are more applicable to the Cm^{3+} S-state splittings than in Gd^{3+} since intermediate coupling effects are expected to dominate in Cm^{3+}. The calculated ground S-state splitting in Cm^{3+}:$LuPO_4$ using free-ion parameters from Cm^{3+}:$LaCl_3$ and crystal-field parameters for Nd^{3+}:YPO_4 is 2.3, 7.3 and 7.7 cm^{-1}.

No crystal-field parameter of any actinide in $LuPO_4$ is available and the splittings of the $^6D_{7/2}$ or the $^6I_{7/2}$ manifold in Cm^{3+}:$LuPO_4$ could not be determined. An alternative is to determine if the spin-Hamiltonian parameters of Cm^{3+}:$LuPO_4$ can be used to predict the ground electronic states of the neighboring actinide ions. If the large intermediate coupling effect is the only important ZFS mechanism in Cm^{3+}:$LuPO_4$, then the spin-Hmailtonian parameters can be related to the crystal-field parameters by the use of the operator equivalent factors [14]. The resulting crystal-field parameters can then be used to calculate the wavefunctions of the crystal-field states of the neighboring actinides in $LuPO_4$. Such an approach relies on the

expectation that crystal-field parameters of neighboring elements do not show large variations, an assumption that is often borne out by experiment. For example, the ground crystal-field state of Np^{4+}:$ZrSiO_4$ (D_{2d} site symmetry) was calculated to be a Γ_6 doublet by using the free-ion parameters of Np^{4+}:$Zr(BD_4)_4$ and the crystal-field parameters of U^{4+}:$ZrSiO_4$. This was experimentally confirmed by EPR [29], Pu^{4+}:$ZrSiO_4$ was also found to have very similar crystal-field parameters [30]. For the present case, g-values of the electronic ground states in Pu^{3+}: $LuPO_4$ and Cf^{3+}:$LuPO_4$ have been determined by EPR and compared to those calculated by using free-ion parameters from crystal-field analyses of Pu^{3+},Cf^{3+}:$LaCl_3$ [26] and a set of crystal-field parameters obtained form the spin-Hamiltonian parameters using the operator equivalent factors. Operator equivalent factors have been calculated for a 50-term Cm^{3+} wavefunction [31] and they are used here together with tabulated conversion factors [32] to give the following "crystal-field parameters" for Cm^{3+}:$LuPO_4$ (in cm^{-1} at 10 K): $B_2^0 = 446$, $B_4^0 = 322$, $B_6^0 = -850$, $B_4^4 = -1{,}080$ and $B_6^4 = 818$.

2.7.1 EPR of Pu^{3+}:$LuPO_4$

Trivalent plutonium has received more EPR studies than any other transuranium actinides. However, most of these studies were performed with cubic-symmetry hosts; no EPR study of Pu^{3+} in D_{2d} site symmetry is known. In general, intermediate coupling is found to be important in determining its electronic structure; the $J = 5/2$ ground manifold of the Pu^{3+} was found to be only 66 % $^6H_{5/2}$ [33].

X-band EPR spectra were recorded at 4 K and the results are shown in Figure 2.14. The least-squares fitted g-values are: $g_{\parallel} = 0.7716$ and $g_{\perp} = 0.6578$. Using the crystal-field parameters from above and the free-ion parameters from the Pu^{3+}:$LaCl_3$ analysis [26], the ground state in Pu^{3+}:$LuPO_4$ is calculated to be a $|\pm\frac{1}{2}\rangle$ doublet with little crystal-field induced J-mixing and the associated g-values are: $g_{\parallel} = 0.4892$ and $g_{\perp} = 1.196$. The calculated first excited state is at 45 cm^{-1} away with $g_{\parallel} = 1.203$ and $g_{\perp} = 0.1477$. The experimentally observed g-values show serious discrepencies with these values and it is clear that the crystal field parameters for

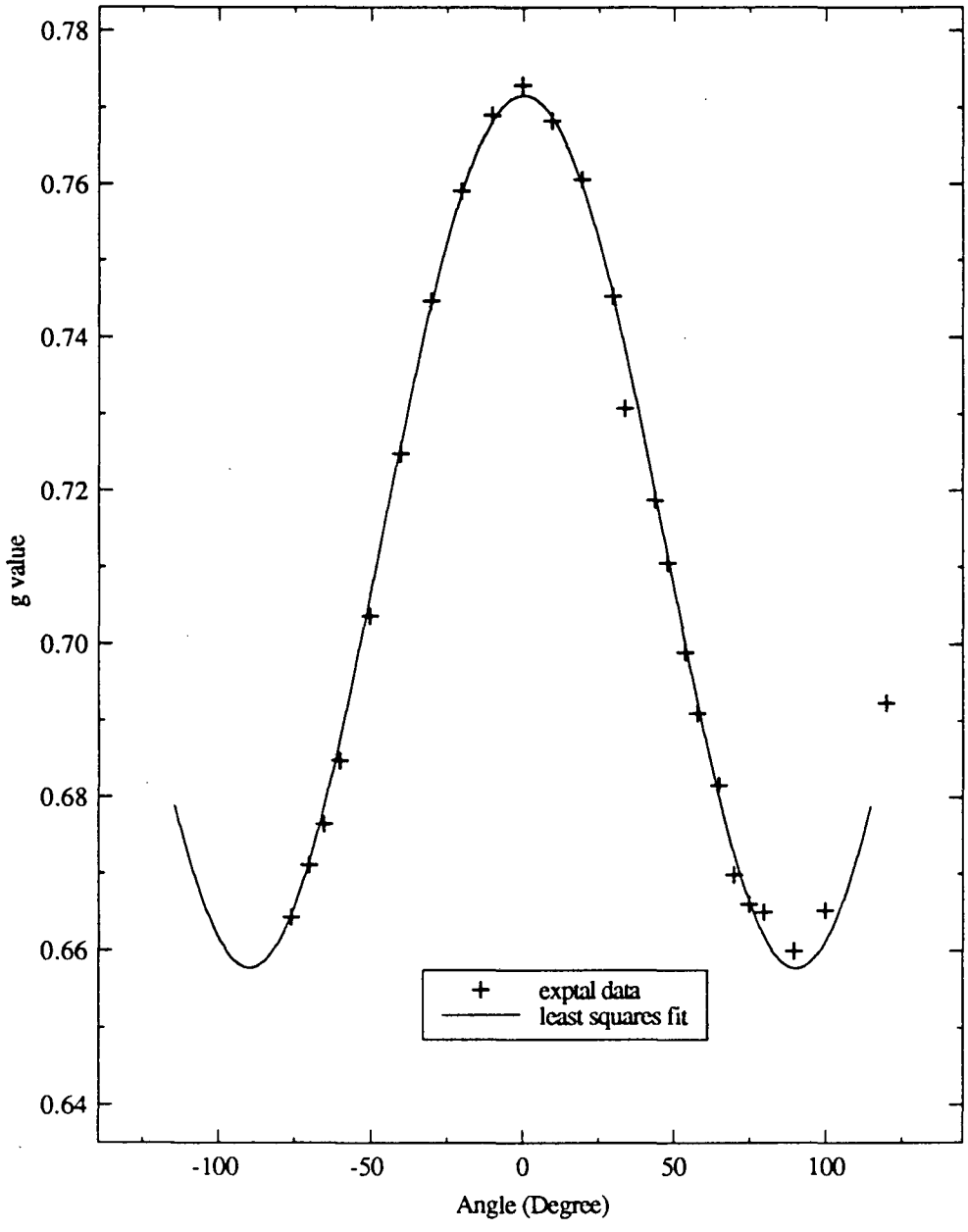

FIGURE 2.14 Experimental and least-squares fitted EPR result of Pu^{3+}:$LuPO_4$ as a functrion of the angle between the crystallographic *c* axis and the magnetic field. Microwave frequency = 9.223 GHz.

Pu^{3+} in $LuPO_4$ would be very different than those obtained from above for Cm^{3+}:$LuPO_4$. Furthermore, if the reasonable assumption is made that crystal-field parameters are very similar among neighboring actinides, it is then seen that the spin-Hamiltonian parameters found for Cm^{3+}:$LuPO_4$ do not bear any simple relationship with its crystal-field parameters.

2.7.2 EPR of Cf^{3+}:$LuPO_4$

Only one EPR study of Cf^{3+} has ever been reported [34] —— the Q-band spectrum of a crystalline powder of Cf^{3+}:$Cs_2NaLuCl_6$ (cubic site symmetry) showed ten hyperfine lines at 4K, confirming the nuclear spin of ^{249}Cf to be 9/2. The Russell-Saunders ground term of Cf^{3+} ($5f^9$) is $^6H_{15/2}$ and the ground crystal-field state was found to be a Γ_6 doublet with a g value of 6.273.

Crystals of $^{249}Cf^{3+}$:$LuPO_4$ were annealed as described above before EPR spectra were collected at X-band frequency at ≈ 4 K. The hyperfine structure was only partially resolved and the peak-to-peak width is 300 G. The experimental results are shown in Figure 2.15 along with the least-squares fit. The g-values found are: $g_{\parallel} = 3.561$ and $g_{\perp} = 7.789$.

The calculated ground state using parameters from Section 2.7 is a Γ_7 doublet with a $|J,M_J\rangle$ wavefunction of

$$-0.943\ |\tfrac{15}{2},\pm\tfrac{15}{2}\rangle + 0.303\ |\tfrac{15}{2},\pm\tfrac{7}{2}\rangle + \text{smaller terms}$$

which, with a g_J-value of 1.279 [34], gives a calculated $g_{\parallel}$ value of −17.89 and $g_{\perp} \approx 0$. An excited Γ_6 state was calculated to be 87 cm^{-1} above ground for which $g_{\parallel} = 4.144$ and $g_{\perp} = 8.242$. The ground $J = 15/2$ manifold of Cf^{3+} gives rise to 8 crystal-field states in D_{2d} symmetry and it is conceivable that a slight variation in crystal-field will result in a different ground state; however, it is evident that, as is the case with Pu^{3+}:$LuPO_4$, the ground state in Cf^{3+}:$LuPO_4$ cannot be predicted straightforwardly from the spin-Hamiltonian parameters of Cm^{3+}:$LuPO_4$.

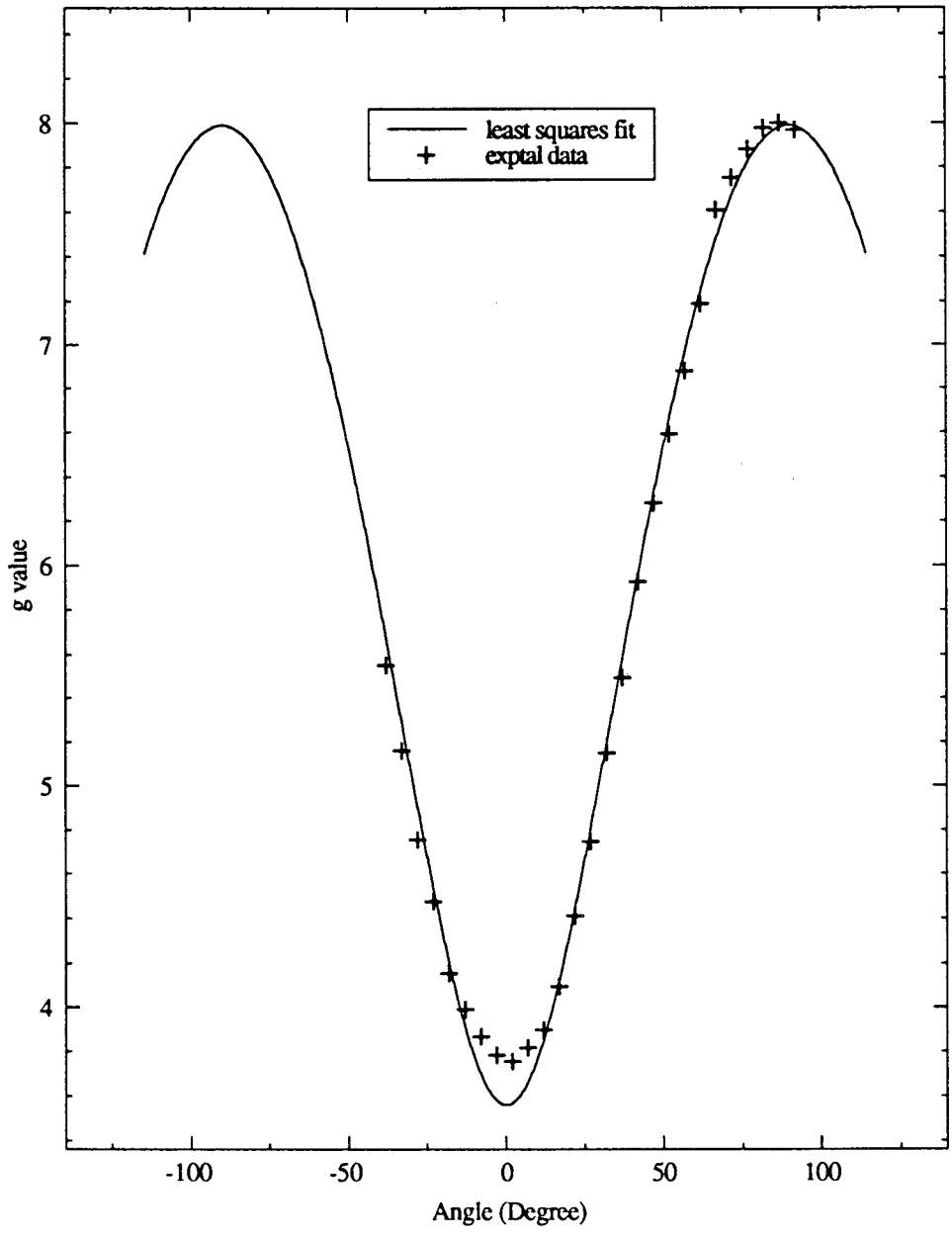

FIGURE 2.15 Experimental and least-squares fitted EPR result of Cf^{3+}:$LuPO_4$ as a functrion of the angle between the crystallographic *c* axis and the magnetic field. Microwave frequency = 9.217 GHz.

2.8 Summary

Zero-field splitting of Cm^{3+} incorporated into $LuPO_4$ has been determined by EPR and shows reasonable agreement with that found in fluorescence and absorption experiments. Although the splitting is large compared to the microwave frequencies employed, four transitions could be assigned and fitted to give a consistent set of spin-Hamiltonian parameters; improvement of these parameters, however, is likely should more data become available. Variable frequency EPR should be invaluable for its study.

The total splitting of $\approx 10\ cm^{-1}$ is considerably smaller than the only previously known Cm^{3+} ZFS of $20.4\ cm^{-1}$ found in $SrCl_2$. The somewhat unexpectedly small crystal-field is probably responsible for the first observation of room-temperature EPR of an actinide. The corresponding splitting found in Gd^{3+}: $LuPO_4$ is $0.78\ cm^{-1}$, the ratio of the two splittings of $\approx$ 12 is also substantially smaller than those found before which normally range in the hundreds. The cause of this dramatic decrease in total ZFS in Cm^{3+}, reflected by the size of b_2^0, is not known; higher-order perturbation is believed to be much more important than in Gd^{3+}, as is the case of Cm^{3+} and Gd^{3+} in $SrCl_2$. Study of Cm^{3+} in another low-symmetry host is desirable in order to determine if b_2^0 and the total ZFS are similarly small. It is perhaps unfortunate that crystal-field data for the excited states are not available such that a more detailed comparison can be made between splittings of the ground and the excited manifolds and light be thrown on the mechanisms that effect these splittings. The spin-Hamiltonian parameters obtained for Cm^{3+}:$LuPO_4$ cannot be used to correctly predict the ground electronic states for Pu^{3+}:$LuPO_4$ and Cf^{3+}:$LuPO_4$. This can be caused by the insufficient precision of the parameters or there may not indeed be a simple correspondence between these and the crystal-field parameters for the excited states.

Appendix 2.A Absorption Spectrum of Cm^{3+}:$LuPO_4$

SLJ state	Experimental (cm^{-1})			
	σ-spectrum		π-spectrum	
$^8S_{7/2}$				
$^6D_{7/2}$	16528.3 cm^{-1}		16528.3 cm^{-1}	
	16524.9	Δ = 3.4		
	16519.9	8.4	16519.9	Δ = 8.4
	16577.5		16577.3	
	—		—	
	—		—	
$^6D_{5/2}$	19775.3		19775.4	
	19771.8	Δ = 3.5		
	19767.9	7.4	19767.5	Δ = 7.9
	—		—	
	—		—	
$^6I_{7/2}$	—		—	
	—		—	
			21445.3	
	21441.6	(Δ = 3.7)		
	21437.7	(Δ = 8.4)	21437.1	Δ = 8.2
	21471.7			
			21468.6	(Δ = 3.1)
	21463.6	Δ = 8.1		

SLJ state	Experimental (cm^{-1})			
	σ-spectrum		π-spectrum	
$^6P_{3/2}$	22034.1		22034.1	
	22137.1		22137.0	
$^6I_{9/2}$	—		—	
	—		—	
	—		—	
	22585.0		—	
	22581.2	Δ = 3.8		
	22575.9	9.1	22575.0	(Δ = 10.0)
	22664.5		22664.8	
	22661.3	Δ = 3.2		
$^6I_{17/2}$ and	24612.3			
$^6I_{11/2}$	24608.9	Δ = 3.4	24608.7	(Δ = 3.4)
	24603.3	9.0		
	24690.8		24690.8	
	24687.0	Δ = 3.2		
	24682.8	8.0	24682.0	Δ = 8.8
	24792.5		24792.7	
	24784.0	Δ = 8.5		

References

[1] (a) M. Abraham, B. B. Cunningham, C. D. Jefferies, R. W. Kedzie and J. C. Wallman, Bull. Am. Phys. Soc. **1**, 396 (1956). (b) P. Fields, A. Friedman, B. Smaller and W. Low, Phys. Rev. **105**, 757 (1957).

[2] M. Abraham, B. R. Judd and H. H. Wickman, Phys. Rev. **130**, 611 (1963).

[3] W. Kolbe, N. Edelstein, C. B. Finch and M. M. Abraham, J. Chem. Phys. **58**, 820 (1973).

[4] D. J. Newman and W. Urban, Adv. Phys. **24**, 793 (1975).

[5] W. Kolbe, N. Edelstein, C. B. Finch and M. M. Abraham, J. Chem. Phys. **56**, 5432 (1972).

[6] R. D. Shannon, Acta. Cryst. **A32**, 751 (1976).

[7] Calculated from published structural parameters. See R. W. G. Wykoff, *Crystal Structures*, Second Edition, Vol. 3 (Wiley-Interscience, New York, 1965).

[8] M. Rappaz, L. A. Boatner and M. M. Abraham, J. Chem. Phys. **73**, 1095 (1980).

[9] G. M. Williams, Ph. D. Dissertation, University of California at Berkeley (1988).

[10] R. D. Cowan, *The Theory of Atomic Structure and Spectra*, (University of California Press, Berkeley, 1981).

[11] W. T. Carnall and B. G. Wybourne, J. Chem. Phys. **40**, 3428 (1964).

[12] D. J. Newman, Adv. Phys. **20**, 197 (1972).

[13] K. W. H. Stevens, Proc. Phys. Soc. (London) **A65**, 209 (1952).

[14] See A. Abragam and B. Bleaney, *Electronic Paramagnetic Resonance of Transition Ions*, (Oxford University Press, London, 1970).

[15] M. Hutchings, Solid State Phys. **16**, 227 edited by F. Sietz and D. Turnbull (Academic, New York, 1964).

[16] M. M. Abraham, G. W. Clark, C. B. Finch, R. W. Reynolds and H. Zeldes, J. Chem. Phys. **50**, 2057 (1969).

[17] M. M. Abraham, L. A. Boatner, C. B. Finch, R. W. Reynolds and W. P. Unruh, Phys. Lett. **44A**, 527 (1973).

[18] J. M. Baker, J. R. Chadwick, G. Garton and J. P. Hurrell, Proc. Roy. Soc. **A286**, 352 (1965).

[19] C. P. Poole, Jr. and H. A. Farach, Bull. Magn. Reson. **1**, 162 (1980).

[20] G. Pfister, W. Dreybrodt and W. Asssmus, Phys. Stat. Sol. **36**, 351 (1969).

[21] V. Koch, Phys. Stat. Sol. **47**, 543 (1971).

[22] H. G. Kahle, H. C. Schopper, W. Urban and W. Wüchner , Phys. St at. So.. **38**, 815 (1970).

[23] (a) B. G. Wybourne, Phys. Rev. **148**, 317 (1966). (b) R. R. Sharma, T. P. Das and R. Orbach, Phys. Rev. **149**, 257 (1966). (c) R. R. Sharma, T. P. Das and R. Orbach, Phys. Rev. **171**, 378 (1968). (d) D. J. Newman and W. Urban, J. Phys. C: Solid State Phys. **5**, 3101 (1972). (e) D. J. Newman, J. Phys. C: Solid State Phys. **8**, 1862 (1975). (f) G. G. Siu, D. J. Newman, J. Phys. C: Solid State Phys. **15**, 6753 (1982).

[24] M. M. Abraham, L. A. Boatner and E. J. Lee, Phys. Lett. **25A**, 230 (1967).

[25] C. A. Baumann, R. J. van Zee, J. K. Zeringue and W. Weltner, Jr., J. Chem. Phys. **75**, 5291 (1981).

[26] W. T. Carnall, Argonne National Laboratory ANL-89/39 (1989).

[27] J. B. Gruber, W. R. Cochran, J. G. Conway and A. T. Nicol, J. Chem. Phys. **45**, 1423 (1966).

[28] S. K. Misra and N. R. Lewis, Phys. Rev. B **31**, 8335 (1985).

[29] I. Poirot, W. Kot, N. Edelstein, M. M. Abraham, C. B. Finch and L. A. Boatner, Phys. Rev. B **37**, 3255 (1988).

[30] I. S. Poirot, W. K. Kot, N. Edelstein, M. M. Abraham, C. B. Finch and L. A. Boatner, Phys. Rev. B **39**, 6388 (1989).

[31] N. Edelstein and W. Easley, J. Chem. Phys. **48**, 2110 (1968).

[32] J. Kassman, J. Chem. Phys. **52**,2117 (1970).

[33] J. G. Conway and K. Rajnak, J. Chem. Phys. **44**, 348 (1966).

[34] N. Edelstein and D. G. Karraker, J. Chem. Phys. **62**, 938 (1975).

Chapter 3

Electronic Structure in Compounds of Trivalent Thorium

3.1 Introduction

The principal oxidation state of thorium is tetravalent; compounds of thorium with a lower oxidation state are exceedingly rare. In the solid state, binary compounds of thorium with the compositions ThX (X = O, S, P, N, Se), ThX_2 (X = I) and ThX_3 (X = Br, I) are known. Most of these compounds are diamagnetic, metallic in appearance, and superconducting at low temperature [1]. The absence of local magnetic moments agrees with band structure calculations which show that the *5f* electrons in the early actinides possess considerable metallic character [2]. Therefore, these compounds may more accurately be formulated as $Th^{4+}(X^{a+})(e^-)_{4-a}$, with unbound electrons filling the conduction bands. Organometallic compounds of trivalent thorium have also been studied for over ten years. However, the compounds in general are not well characterized and very often conflicting information exist. For example, two different forms of $(\eta^5\text{-}C_5H_5)_3Th$ have been reported —— one is purple in color with a magnetic moment of 0.403 μ_B at room temperature while the other is green and has a magnetic moment of 2.10 μ_B [3,4].

Electrochemical reduction [5], photolysis [6] and pulse radiolysis [7] are among the many techniques used to generate and study trivalent thorium species. In most cases, only indirect evidence of the existence of Th(III) has been observed. It was found that while $(C_5Me_5)_2UCl_2$ could be reduced electrochemically to give the relatively stable $(C_5Me_5)_2UCl_2^-$,

the thorium analogue could not be reduced down to a potential of –2.7 V (vs. SCE) [5]. The Th(IV)→ Th(III) reduction potential has been estimated to be as low as –3.7 V [8].

Photolysis of solutions of $(C_5H_5)_3ThR$ and $(C_9H_7)_3ThR$ (R = alkyl) yielded gaseous mixtures of the corresponding alkanes and alkenes. The remaining solutions showed absorption spectra in the visible region which were attributed to Th(III). A photoinduced β-hydride elimination mechanism was then proposed (Scheme 1), although the same organometallic product was found in the photolysis of $(C_5H_5)_3ThCH_3$. A secondary and less important reaction pathway involves intramolecular hydrogen atom abstraction from the ligands and, to a lesser extent, the solvent, resulting in different organometallic products. This second pathway was found to be the dominant pathway in the thermolysis of $(C_5H_5)_3ThR$ and the photolysis of $(C_5H_5)_3UR$ [6].

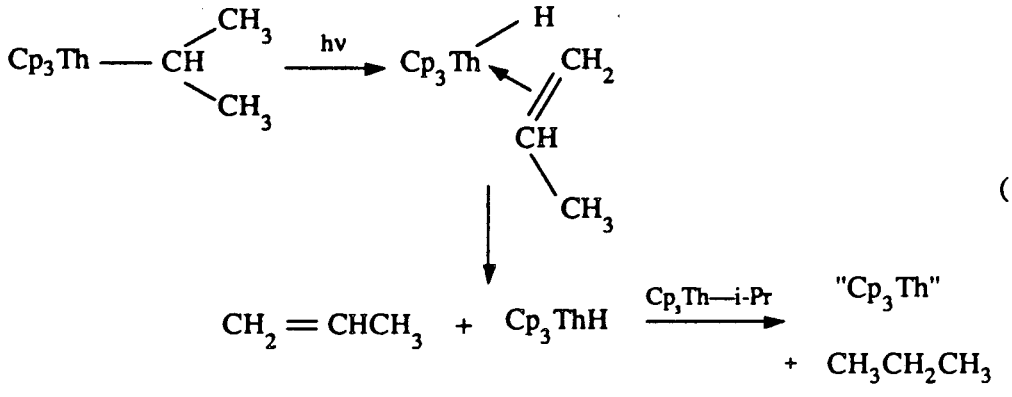

(1)

Pulse radiolysis employing solvated electrons in tetrahydrofuran (THF) was also used to reduce $(C_5Me_5)_2ThCl_2$ [7]. The resulting absorption spectrum of a transient species, which was similar to those in the photolysis experiment, was attributed to Th(III). The spectrum disappeared quickly with a first-order rate constant of $\approx 10^6\ s^{-1}$, leading to a different spectrum which was also attributed to Th(III). No other evidence of the existence of Th(III) was presented.

It is obvious that Th(IV) can only be reduced under extreme conditions and once generated, Th(III) is very reactive. However, using the bulky ligand $C_5H_3(SiMe_3)_2^-$, Blake *et al.* were able to isolate $[\eta^5\text{-}C_5H_3(SiMe_3)_2\text{–}1,3]_3Th$ [9]. It was structurally characterized and the

three cyclopentadienyl rings were found to be distributed symmetrically around the thorium atom, resulting in a pseudo-trigonal-planar geometry. It remains as the only structurally characterized Th(III) compound. The lanthanide analogue $[\eta^5\text{-}C_5H_3(SiMe_3)_2]_3Ce$ was found to be isostructural [10].

3.2 Electron Paramagnetic Resonance Spectroscopy of $[\eta^5\text{-}C_5H_3(SiMe_3)_2]_3Th$

A sample of $[\eta^5\text{-}C_5H_3(SiMe_3)_2]_3Th$ was received from Professor M. F. Lappert of the University of Sussex. Electron paramagnetic resonance (EPR) spectra of the blue powder and its solution in methylcyclohexane (MCH) are shown in Figures 3.1 and 3.2, respectively. The spectra can be fitted to the spin-Hamiltonian

$$\mathcal{H} = g_{\parallel}\,\beta H_z S_z + g_{\perp}\,\beta (H_x S_x + H_y S_y) \tag{3.1}$$

and the results are summarized in Table 3.1. The sample gave a strong EPR signal at room temperature. The powder spectrum is typical of a system with axial symmetry and remains essentially unchanged from 300 K to 10 K. The peak width is 8 G. From the difference in peak shapes, $g_{\parallel}$ and $g_{\perp}$ can easily be identified. No attempt was made to obtain a single crystal spectrum; but small single crystals, recrystallized from a hexane solution, gave strong signals in the same region, the exact signal varied according to the orientation of the crystals with respect to the magnetic field.

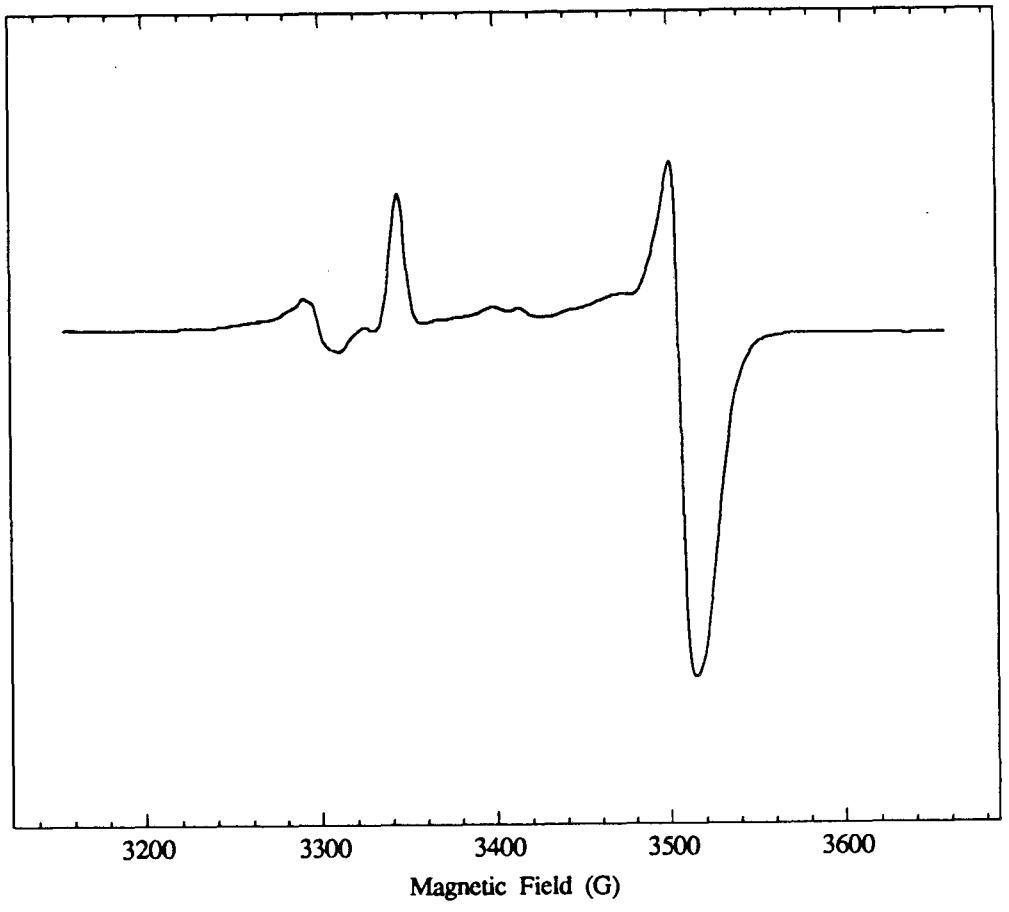

FIGURE 3.1 EPR spectrum of $[\eta^5\text{-}C_5H_3(SiMe_3)_2]_3Th$ powder at room temperature. Microwave frequency = 9.235 GHz. A g = 2.00 impurity is present.

	Temperature (K)	$g_{\parallel}$	$g_{\perp}$	g_{av}
Powder	10-300	1.972 ± 0.001	1.878 ± 0.001	1.909[a]
Solution	10-100	1.9725 ± 0.001	1.879 ± 0.001	1.910[a]
Solution	300			1.910 ± 0.001

[a] Calculated from $1/3(g_{\parallel} + 2g_{\perp})$.

TABLE 3.1 Spin Hamiltonian Parameters for $[\eta^5\text{-}C_5H_3(SiMe_3)_2]_3Th$.

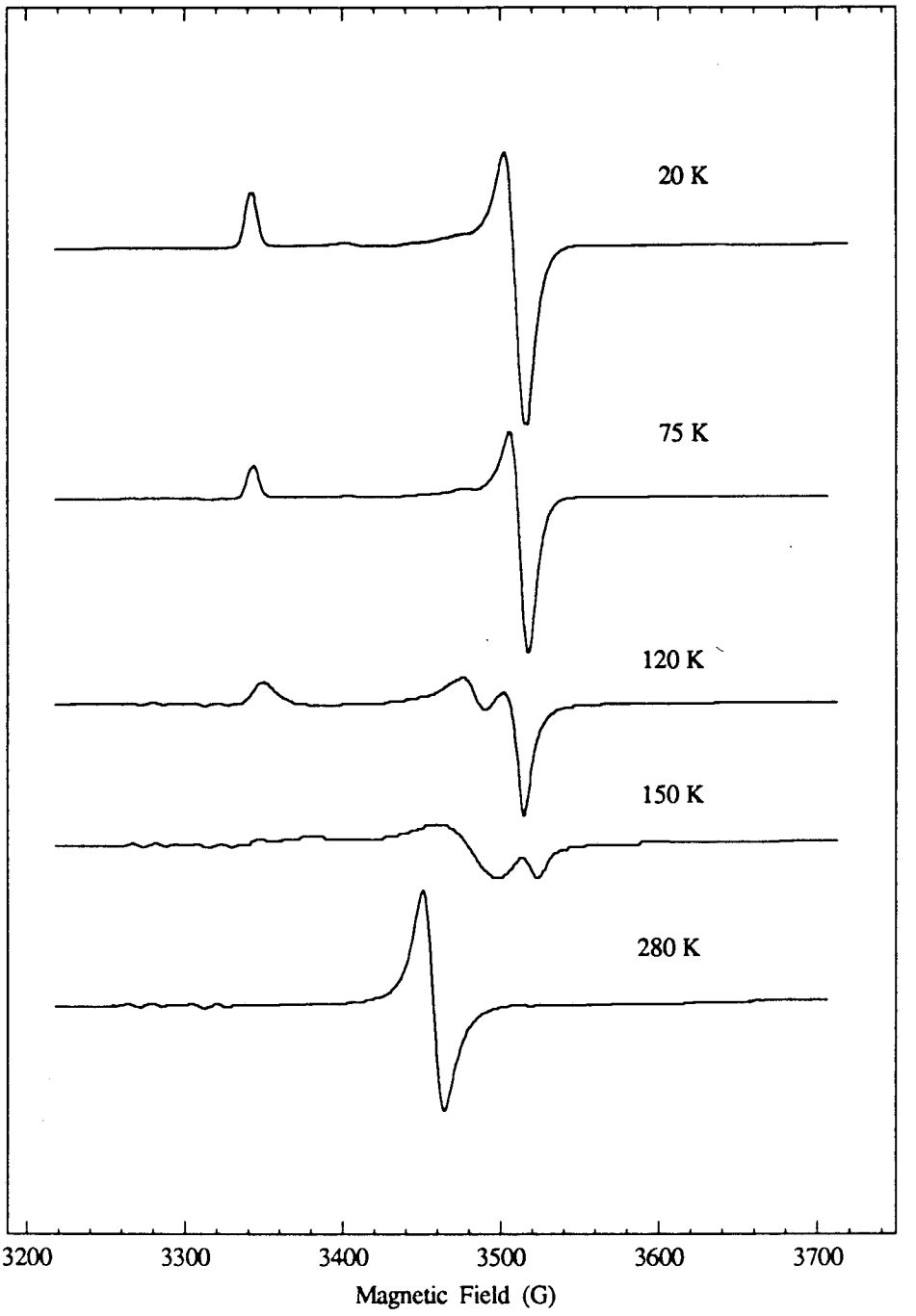

FIGURE 3.2 EPR spectra of $[\eta^5\text{-}C_5H_3(SiMe_3)_2]_3Th$ in methylcyclohexane at various temperatures. Microwave frequency = 9.255 GHz. The freezing point of MCH is 147 K.

The solution spectum at room temperature consists of a single peak (≈ 8 G wide) which is the weighted average of the powder spectrum. As the temperature was lowered, $g_{\parallel}$ and $g_{\perp}$ began to get resolved and at ≈ 80 K the spectrum became identical to that of the powder and remained so down to 10 K. This temperature dependence was reproducible upon cycles of raising and lowering of temperatures. The somewhat surprising result that Th(III) gives an EPR signal at room temperature has prompted the investigation of various other Th(III) compounds.

3.3 EPR of $(C_9H_7)_3Th$

The indenyl anion, $C_9H_7^-$, is formally analogous to the cyclopentadienyl anion, but differs in steric requirement and electronic structure. The greater non-bonded repulsions between ligands have been demonstrated by a comparison of the molecular structures of $(\eta^5\text{-}C_9H_7)_3UCl$ and $(\eta^5\text{-}C_5H_5)_3UCl$ [11] —— both have distorted tetrahedral geometries but $(\eta^5\text{-}C_9H_7)_3UCl$ has longer U–ligand distances and a more idealized tetrahedral geometry. Electronically, in contrast to the completely delocalized π-system in $C_5H_5^-$, charge is localized at positions 1 and 3 (1), as shown clearly by MO calculation and the crystal structure of indenyllithium tetramethylethylenediamine [12]. The structure of $(C_9H_7)_4Th$, with shorter Th—C distances for positions 1, 2 and 3 than 4 and 9, suggests a trihapto bonding between the metal and the five-membered rings [13]. Nuclear Magnetic Resonance (NMR) data have provided additional evidence for such a bonding scheme [14].

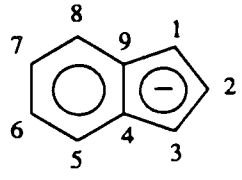

(1)

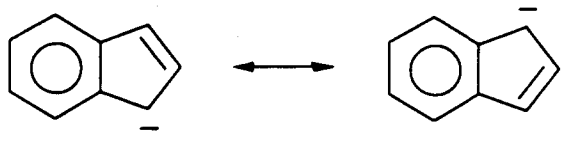

The compounds $(C_9H_7)_3M$ (M = Th, U) have been reported but little synthetic and spectroscopic information was given. As mentioned in Section 3.1, the presence of $(C_9H_7)_3Th(III)$ from photolysis was only indirectly inferred [6]. Because of its high sensitivity, EPR should be a very appropriate technique to study $(C_9H_7)_3Th$. It is expected that $(C_9H_7)_3Th$ will have a structure similar to that of $(C_9H_7)_3U$, which was found to consist of pentahapto indenyl rings surrounding the metal atom in a trigonal manner [15].

According to published procedure [16], $(C_9H_7)_3ThCl$ was prepared and identified by x-ray powder diffraction. A pale yellow solution of $(C_9H_7)_3ThCl$ in toluene was reduced in two different ways : i) by additon of a THF solution of sodium naphthalide and ii) by refluxing a toluene solution of the chloride with potassium metal. Stoichiometric amount as well as a large excess of the reductants were used in different runs. In all cases, the color of the solution darkened quickly, and in the case of i), to dark brown. Periodically, a portion of the solution was removed and examined by EPR but no signal was observed except for reaction i) where the presence of an intense $g = 2.00$ peak was attributed to the reductant. After 8 hours of reaction, the solvent (and naphthalene) was removed by vacuum, extraction with toluene followed by crystallization gave pale yellow crystals which were identified to be $(\eta^3\text{-}C_9H_7)_4Th$ by powder diffraction and its melting point (174-177 °C). The mass spectrum showed no parent ion, but $(M-C_9H_7)^+$ (relative intensity = 100), $(M-2C_9H_7)^+$ (95) and $(M-3C_9H_7)^+$ (10) were all present. No EPR could be observed on the crystals at any temperature. While one can only speculate on the exact mechanism of the above reactions, it is reasonable to assume that trivalent thorium is generated but goes on to react quickly to give the final product.

Since chemical reduction failed to produce $(C_9H_7)_3Th$, we turned to photolysis. The compound $(C_9H_7)_3ThCH_3$ was prepared by reacting $(C_9H_7)_3ThCl$ with methyl lithium in THF [17]. It was purified by sublimation (10^{-3}torr, 170°C) and identified by its mass spectrum, NMR spectrum (*vide infra*) and melting point (213-216°C). Its absorption spectrum in d_8-toluene is shown in Figure 3.3. Electronic spectra of $(C_5H_5)_3ThCH_3$ and $(C_5H_5)_3Th(n\text{-}C_4H_9)$, taken from reference 4, are included for comparison —— the intense absorption edges ($\log \varepsilon > 4.0$) in the UV region have been assigned as the $\eta^5\text{-}C_5H_5$ ligand to metal charge transfer (LMCT) transition. The absorption edge of the indenyl compound shows a considerable red-shift. A similar shift has been found to exist for the uranium pair, $(C_9H_7)_3UCl$ and

$(C_5H_5)_3UCl$ [16]. Such a shift can probably be predicted from the photoelectron spectroscopic (PES) data which show that $(C_9H_7)_3MX$ (M = Th, U and X = Cl, Br, CH_3) have lower ionization potentials than $(C_5H_5)_3MX$ [18]. The ligand-based highest occupied molecular orbital (HOMO) is 0.2-0.5 eV higher in energy in the indenyl compounds.

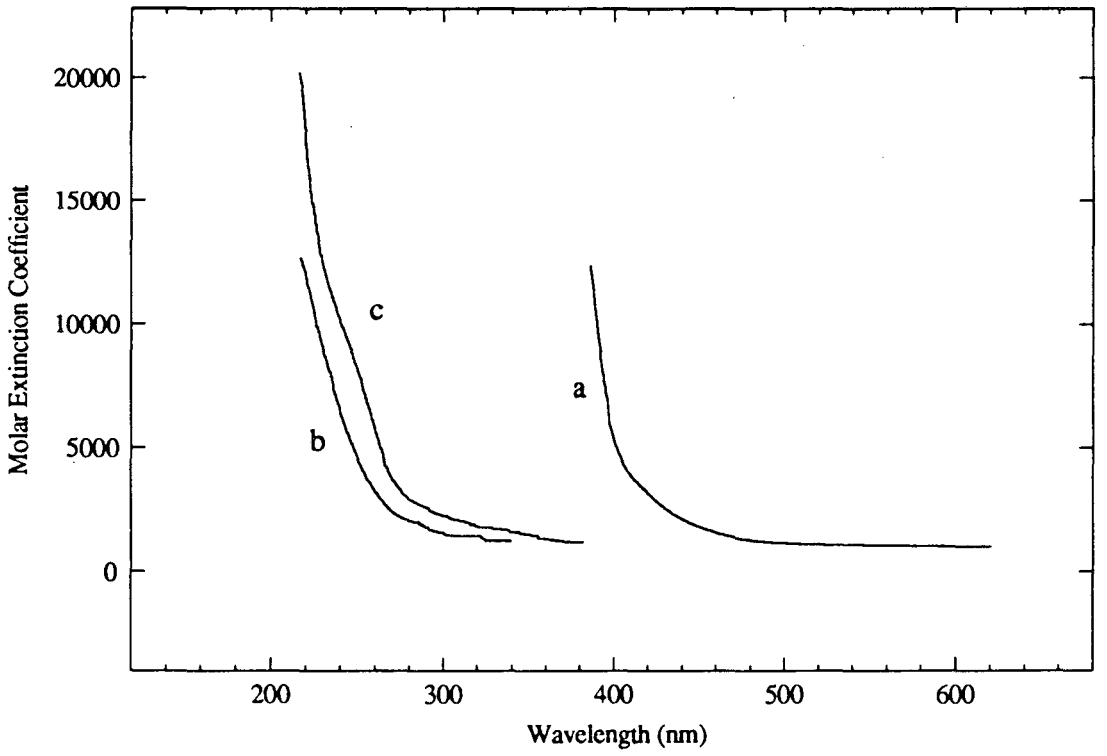

FIGURE 3.3 Electronic spectra of a) $(C_9H_7)_3ThCH_3$ in d_8-toluene, b) $(C_5H_5)_3ThCH_3$ and c) $(C_5H_5)_3Th(n\text{-}C_4H_9)$. b) and c) are from Reference 4 and are in cyclohexane.

Photolysis was carried out with a solution of $(C_9H_7)\,ThCH_3$ in d_8-toluene sealed inside an EPR tube. Radiation from a mercury lamp (Hanovia 616A-13) was collected and focused onto the sample with a quartz lens; the average power was ≈ 120 mW. The reaction was monitored by both NMR and EPR. The color of the solution changed quickly to orange upon irradiating and then to red after 4 hours with small amount of a pale yellow precipitate dropping out of solution. The NMR (Fig 3.4) showed a decrease in magnitude of the resonances due to the indenyl rings and the methyl group (normalized to the solvent peak) while a peak at 0.25 ppm grew in. This peak can be assigned as due to methane dissolved in toluene

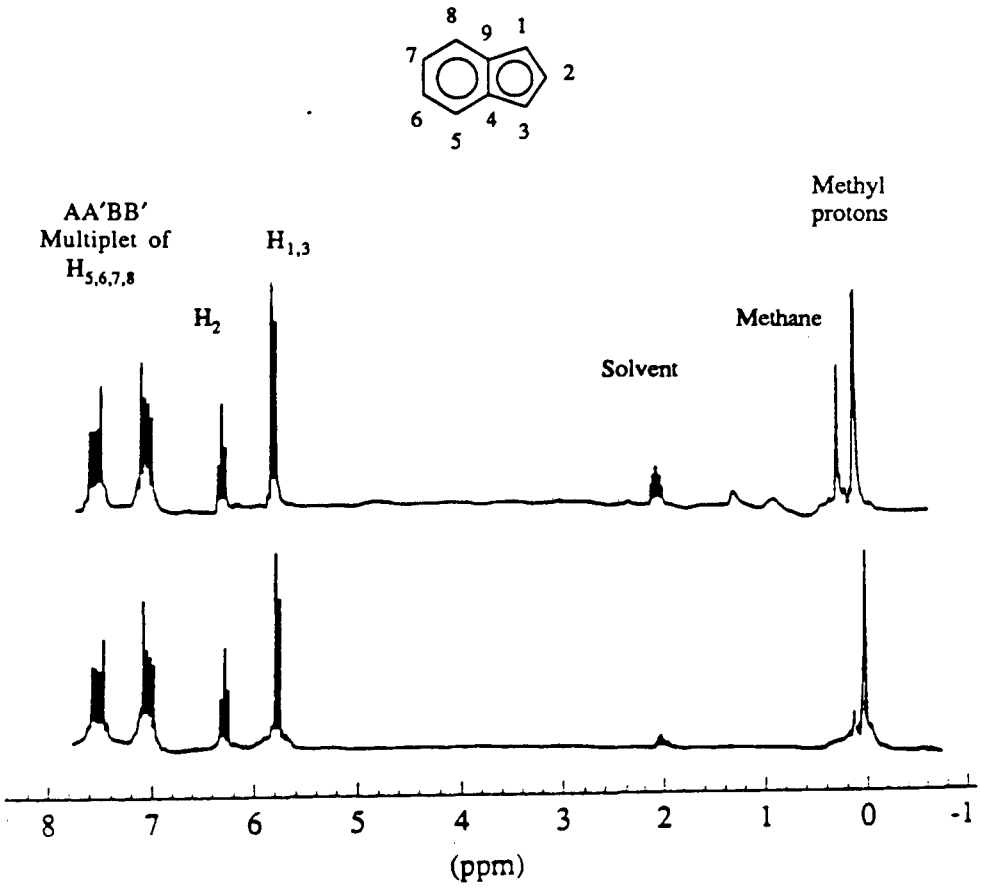

FIGURE 3.4 NMR spectrum of $(C_9H_7)_3ThCH_3$ before (bottom) and after 4 hours (top) of photolysis in d_8-toluene. Spectra were taken with a quartz EPR tube instead of a regular NMR tube. The H_2 resonance of $(C_9H_7)_4Th$ is at 5.20 ppm.

(compared with 0.23 ppm in benzene). Methane, together with traces of ethane and hydrogen, have been identified before by gas chromatography as the gaseous products in the photolysis of thorium and uranium methyl complexes [6]. Weak, broad signals at 0.5-1.5 ppm were also present but they could not be identified. In addition, no evidence of $(C_9H_7)_4Th$ or electron exchange between $(C_9H_7)_3ThCH_3$ and any Th(III) species was observed. However, an EPR signal was observed at room temperature (Fig 3.5a). It has a *g* value of 1.953 and a peak width of 14 G. This signal cannot be due to any organic radical or anion such as $CH_3\cdot$, $C_9H_7\cdot$ and $C_7D_8^-$ —— they have been studied extensively and all have *g* values of 2.00, sharper lines and

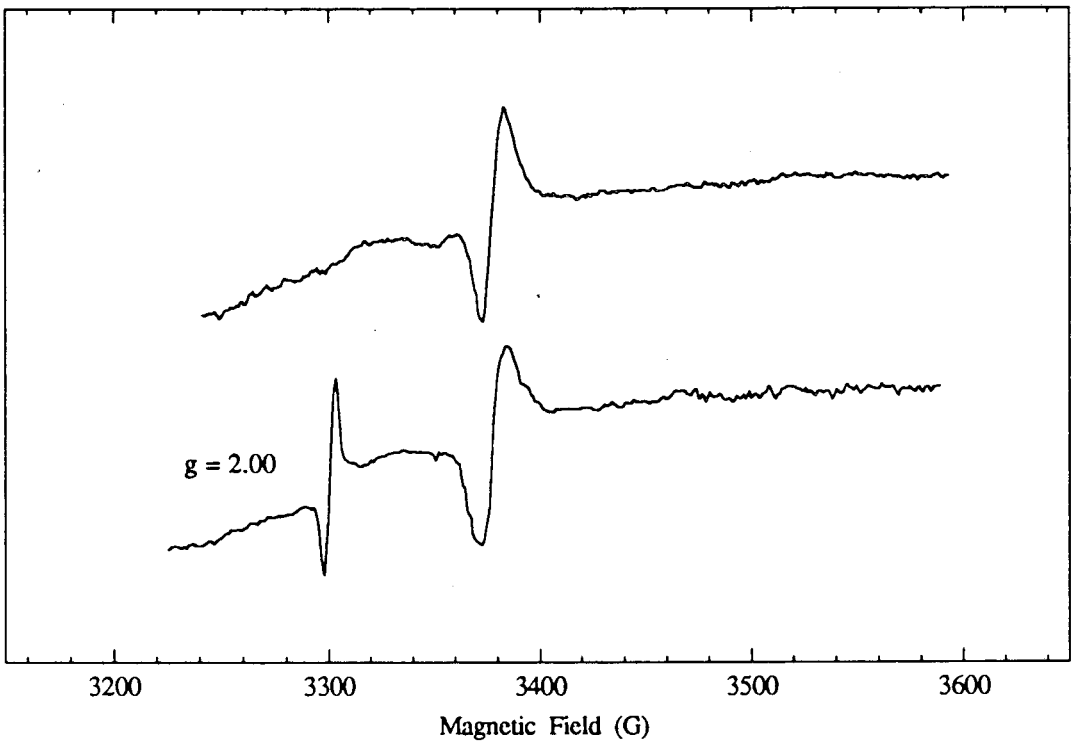

FIGURE 3.5 EPR spectrum of the photolysis product of (a, top) $(C_9H_7)_3ThCH_3$ and (b, bottom) $(C_9H_7)_3Th(n\text{-}C_4H_9)$ in d_8-toluene at room temperature. Microwave Frequency = (a) 9.238 GHz and (b) 9.229 GHz.

very distinctive hyperfine structures [19]. The EPR signal was shown to be due to the red solution as the yellow precipitate by itself, after filtration, did not give any spectrum. The precipitate was not studied further. A similar EPR spectrum was obtained with the photolysis product of $(C_9H_7)_3Th(n\text{-}C_4H_9)$ (Figure 3-5b), but with an extra peak at $g = 2.00$ which was not identified. Photolysis of $(C_9H_7)_3Th(n\text{-}C_4H_9)$ proceeded in an identical fashion as that of the methy compound.

As the temperature was lowered, the EPR signal showed very much the same behavior as that of $[\eta^5\text{-}C_5H_3(SiMe_3)_2]_3Th$ and the two components of the g tensor were clearly resolved at about 80 K, with $g_{\parallel} = 1.978$ and $g_{\perp} = 1.941$ and a calculated average g value of 1.9533. However, the spectra are much noisier in this case and this is primarily due to two reasons. Firstly, $(C_9H_7)_3ThCH_3$ has a rather limited solubility in toluene and the quantum yield of the photolysis is not known but presumed to be low, judging from the NMR signal of the residual alkyl. The concentration of $(C_9H_7)_3Th$ is therefore expected to be very low. Prolonged photolysis did not improve the signal; complete reaction also could not be achieved in the photolysis of Cp_3ThCH_3 and Cp_3UCH_3 [6]. Secondly, toluene as a solvent does not freeze into a uniform glass as does MCH; $(C_9H_7)_3Th$ is even less soluble in MCH.

Another Th(III) system chosen for study is the reduction of $ClTh[N(tms)_2]_3$ (tms = trimethylsilyl). Monomeric $M[N(tms)_2]_3$ (M = transition metal, rare earths and U) is known [20] and its formal low coordination of three is thought to be stabilized by the bulky tms groups. If it existed, $Th[N(tms)_2]_3$ should be of special interest because of the possibility of observing superhyperfine interaction between the unpaired electron and the nitrogen nuclei. Simpson *et al.* have synthesized $XTh[N(tms)_2]_3$ (X = Cl, BH_4 and CH_3) and found that the monomeric hydride $HTh[N(tms)_2]_3$ could be prepared from the reaction of $ClTh[N(tms)_2]_3$ with $NaN(tms)_2$ in THF [21]; the solvent was believed to be the source of hydrogen atom. Pyrolysis of $CH_3Th[N(tms)_2]_3$ gave the four-membered ring metallacycle $[(tms)_2N]_2Th\overline{CH_2SiMe_2N}tms$. While chemical reduction was not expected to result in stable $Th[N(tms)_2]_3$, as in the case of chemical reduction of In_3ThCl, it was hoped that $Th[N(tms)_2]_3$ would be kinetically stable enough such that an EPR spectrum of it could be recorded. Addition of a THF solution of sodium naphthalide to a hexane solution of $ClTh[N(tms)_2]_3$ resulted in an intense purplish-blue color which faded away almost instantaneously; the final product isolated was $HTh[N(tms)_2]_3$

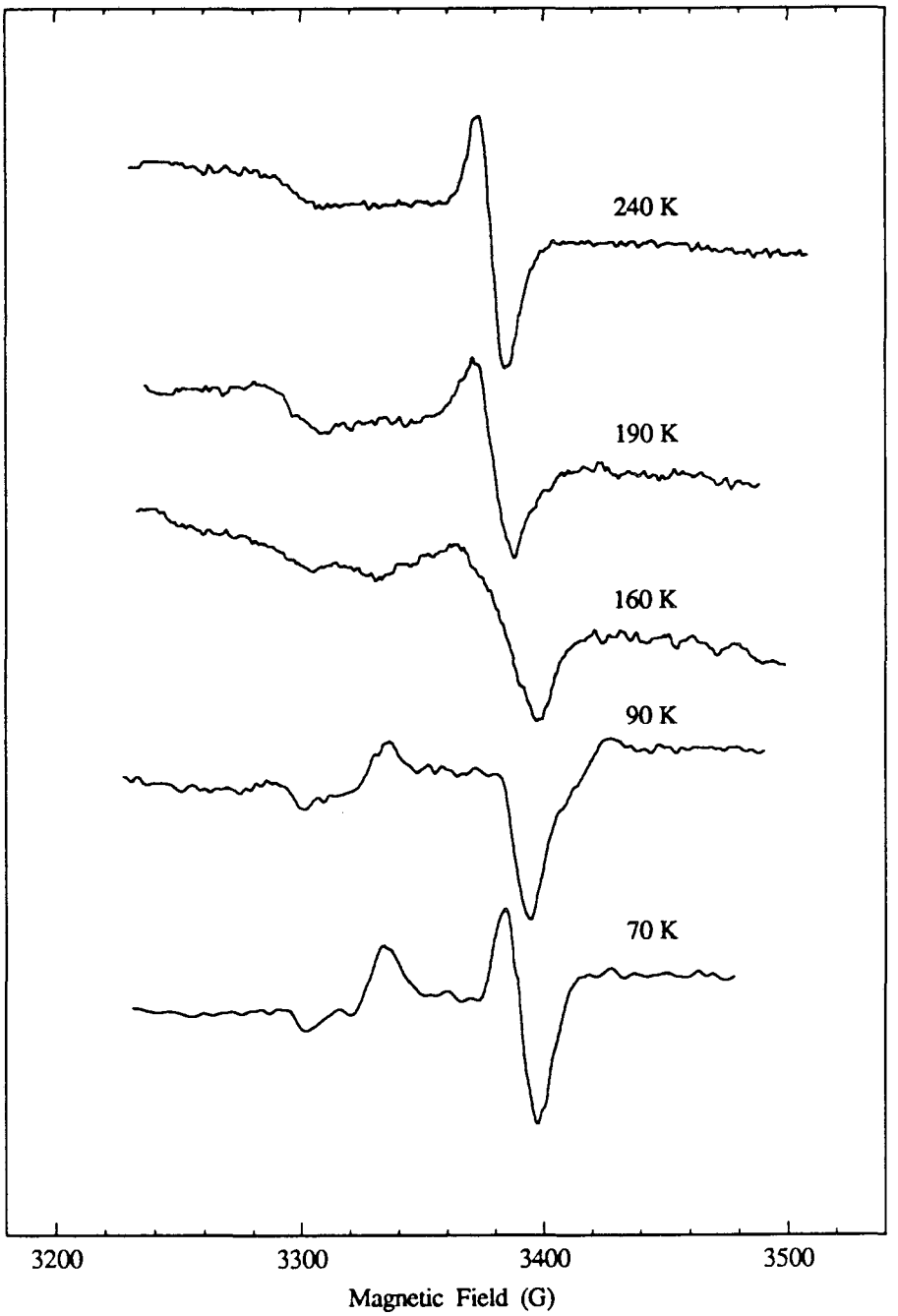

FIGURE 3.6 EPR of the photolysis product of $(C_9H_7)_3ThCH_3$ in d_8-toluene at various temperatures. Microwave frequency = 9.235 GHz. The freezing point of toluene is 180 K.

whose identity was verified by NMR. Performing the reaction at –78° C did not significantly increase the lifetime of the blue intermediate which disappeared before its EPR could be recorded. Photolysis of $CH_3Th[N(tms)_2]_3$ does not seem to be a viable route to $Th[N(tms)_2]_3$ either —— Bradley *et al.* found that photolysis of $CH_3Zr[N(tms)_2]_3$ yielded the metallacycle $[(tms)_2N]_2Zn\overline{CH_2SiMe_2}Ntms$ instead of $Zr[N(tms)_2]_3$ although $Ti[N(tms)_2]_3$ was the stable photolysis product of $CH_3Ti[N(tms)_2]_3$ [22]; the less stable trivalent state and the larger size of Zr was thought to be the difference. Thus one would expect photolysis of $CH_3Th[N(tms)_2]_3$ to give the same meatllacycle product as in pyrolysis. The problem of $Th[N(tms)_2]_3$ was not pursued further.

3.4 Absorption Spectrum of $[\eta^5\text{-}C_5H_3(SiMe_3)_2]_3Th$

The absorption spectra of Cp''_3Th ($Cp'' = \eta^5\text{-}C_5H_3(SiMe_3)_2$) in MCH were recorded at room temperature, 77 K and 4 K. The room temperature and 4 K spectra are shown in Figure 3.7; the 77 K spectrum shows little difference than the 4 K spectrum. Solid state specta were also obtained with a thin film of sublimate of Cp''_3Th at these temperatures and they were identical to the solution spectra; no extra peak was found in the region where the solvent absorbed. These spectra show a great similarity to those obtained in the pulse radiolysis experiment [7] and the photolysis experiment [6] in the number and positions of the absorption bands. They were assigned as $f \rightarrow f$ transitions of Th^{3+} in the radiolysis experiment. These absorption bands are extremely broad (1000 – 1500 cm^{-1} FWHM) and are distinctly different than the sharp $f \rightarrow f$ transitions (see section 2.6), lowering the temperature did not significantly reduce the linewidth. In addition, these bands are very intense; their oscillator strengths were measured according to [23]

$$f = 4.315 \times 10^{-9} \int_{\nu_1}^{\nu_2} \varepsilon \, d\nu \qquad (3.2)$$

where ε is the molar extinction coefficient and ν is the wavelength. The results are listed in Table 3.2. Also listed in Table 3.2 for comparison are oscillator strengths for typical $f \rightarrow f$ transitions found in organolanthanides [24].

Attempts were also made to record the absorption spectra of the photolysis product of In_3ThCH_3 (In = C_9H_7). The absorption edge of In_3ThCH_3 was found to shift to a lower energy at ≈ 15,000 cm^{-1}. No fine structure could be resolved since the photolysis was not complete and the intense charge transfer band of the methyl was still present.

The absorption spectra of Cp''_3Th, along with the EPR results from above, are discussed in the following section.

Cp''_3Th		$Cp_3Er{\cdot}MeTHF$	
Band Energy (cm^{-1})	Oscillator Strength ($\times 10^{-6}$)	Band Energy (cm^{-1})	Oscillator Strength ($\times 10^{-6}$)
		9400–10800	1.47
14800–15900	2210	12000–12900	1.05
16450–17600	1460	14800–15800	4.80
19120–20300	3025	18000–18700	2.55
25000	1520	18700–19800	68.50
		20000–21100	6.80
		21800–23000	0.77

TABLE 3.2 Measured Oscillator strengths for Cp''_3Th and $Cp_3Er{\cdot}MeTHF$ (from Ref. 24)

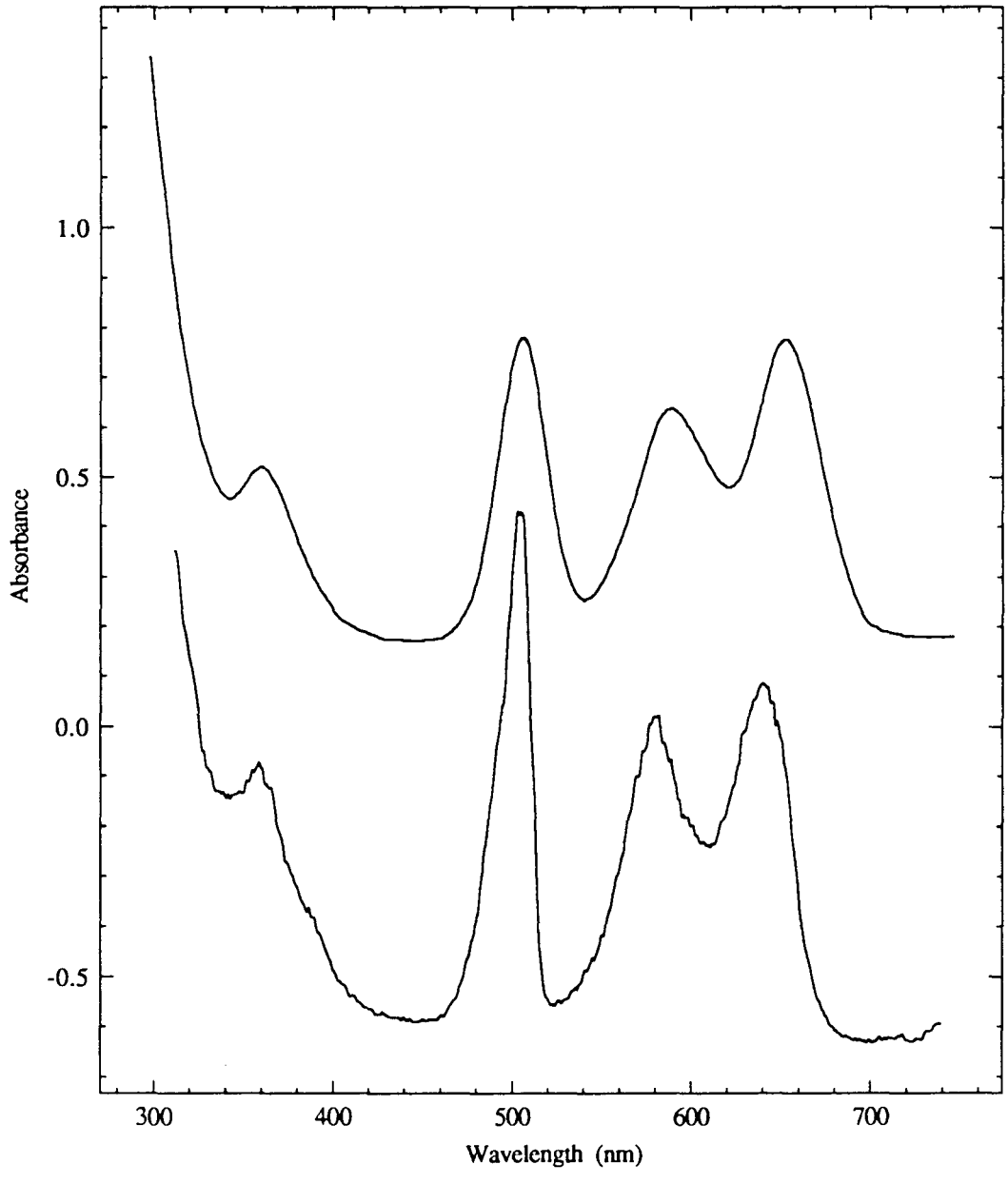

FIGURE 3.7 Absorption spectrum of Cp''_3Th in MCH at room temperature (top) and 4 K (bottom). Concentration of solution = 7.82×10^{-4} M and path length = 1 cm. Absorbance scale is for the room temperature spectrum only.

3.5 Electronic Structures of Cp''_3Th and In_3Th

At the beginning of the actinide series, the various electronic configurations outside the radon core are very close in energy. As one moves across the series, the *5f* becomes increasingly stable relative to the other configurations, mainly because the *5f* radial distribution is closer to the nucleus and is affected the most by the increasing effective nuclear charge. This is demonstrated in Figure 3.8 where the energies of the different configurations of the isoelectronic series $Ra^{1+} - U^{5+}$ are plotted. Note that this is not the same as the actinide contraction, but they are closely related. The same trend also exists in the lanthanide series, but a major difference between the two series is that the *4f* orbitals become stablized much faster than the *5f* and the energies of the different configurations are more closely spaced together in the actinides. For example, the *5f*, *6d*, *7s* and *7p* configurations are within ≈ 60,000 cm^{-1} of one another in Th^{3+}, compared to the *4f*, *5d*, *6s* and *6p* configurations in Ce^{3+} which span ≈ 120,000 cm^{-1}. This difference stems partly from the fact that the *5f* orbitals have a radial node and significant amplitude outside the outer shells. Pitzer [25] has also shown that relativistic effect makes the *5f* orbitals more loosely bound while the *7s* and *7p* become more compact and strongly bound, thus substantially narrowing the ranges of the orbital energies.

The free ion Th^{3+} has a ground configuration of $5f^1$, the first excited configuration $6d^1$ has a center of gravity that is only 9,978 cm^{-1} above that of the ground configuration [26]. A crystal-field surrounding the free ion will have a dramatic effect on these configurations.

As the spherical symmetry of the free ion is lowered by application of a crystal-field, the degeneracies of its electronic states are removed, and the energy levels begin to split, the number of levels and the magnitude of the splitting depend on the symmetry and the strength of the crystal-field. However, it is well established in classical crystal-field theory that the *d* orbitals, being spatially more diffuse and less shielded than the *f* (see Fig 3.9), experience a much greater crystal field and hence a much larger splitting. The crystal-field parameters describing these two configurations, based on an ionic point charge model, are related by:

$$\frac{(B^k_n)_d}{(B^k_n)_f} = \frac{\langle r^k \rangle_d}{\langle r^k \rangle_f} \tag{3.3}$$

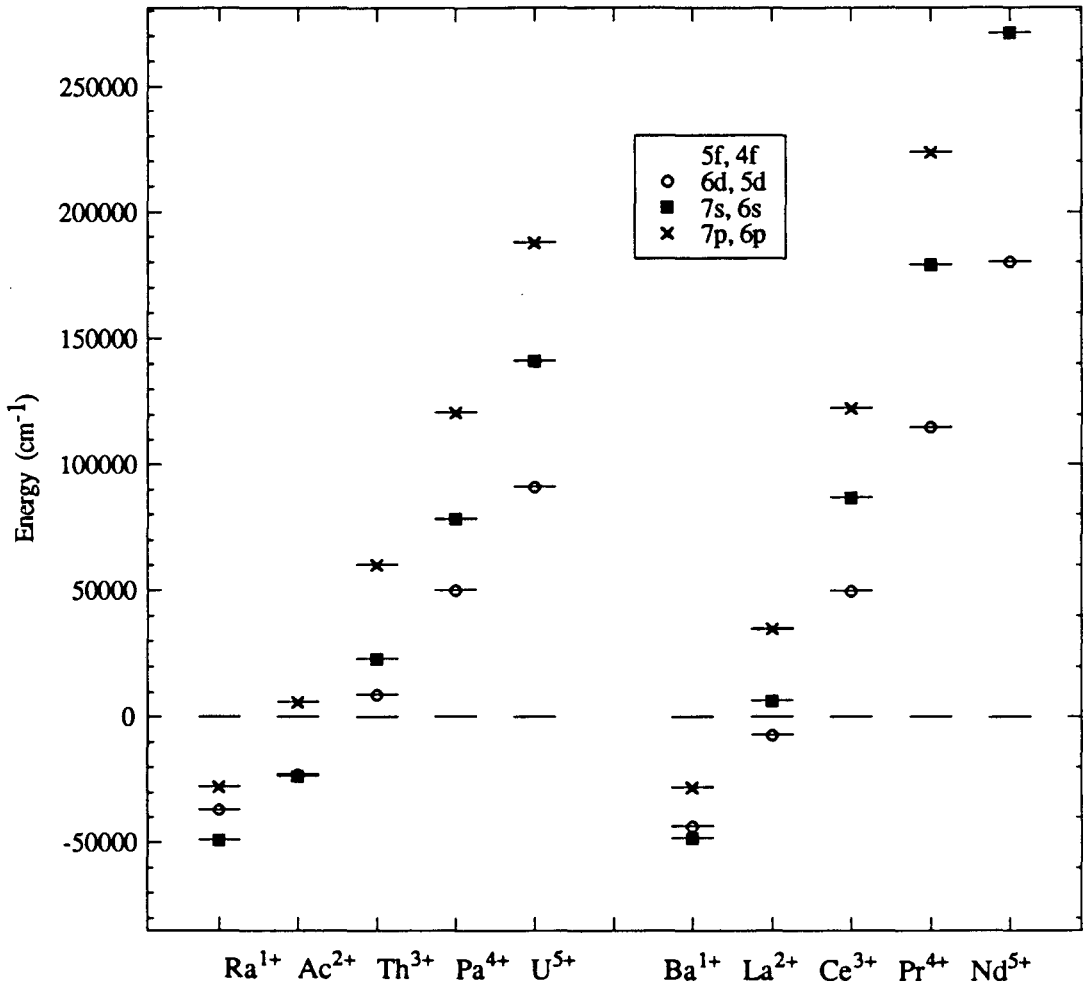

FIGURE 3.8 Energies of the various electronic configurations of the two isoelectronic series Ra^{1+} to U^{5+} and Ba^{1+} to Nd^{5+}.

where $\langle r^k \rangle$ is the expectation value of the k-th power of the radial distributions of the d and f orbitals. From a Hartree-Fock calculation [27], these ratios are 2.62 for $k = 2$ and 5.16 for $k = 4$. Most of the data illustrating this difference in crystal-field strengths have been amassed in Ce^{3+} where both the oxidation state and the energy ranges of the configurations are easily accessible. While the f orbital splittings are caused primarily by spin-orbit coupling and remain relatively constant at $\approx$ 2,200 cm^{-1}, the total d orbital splittings range from 10,000 cm^{-1} in Ce^{3+}:LaF_3 [28] to 20,000 cm^{-1} in Ce^{3+}:$LuPO_4$ [29].

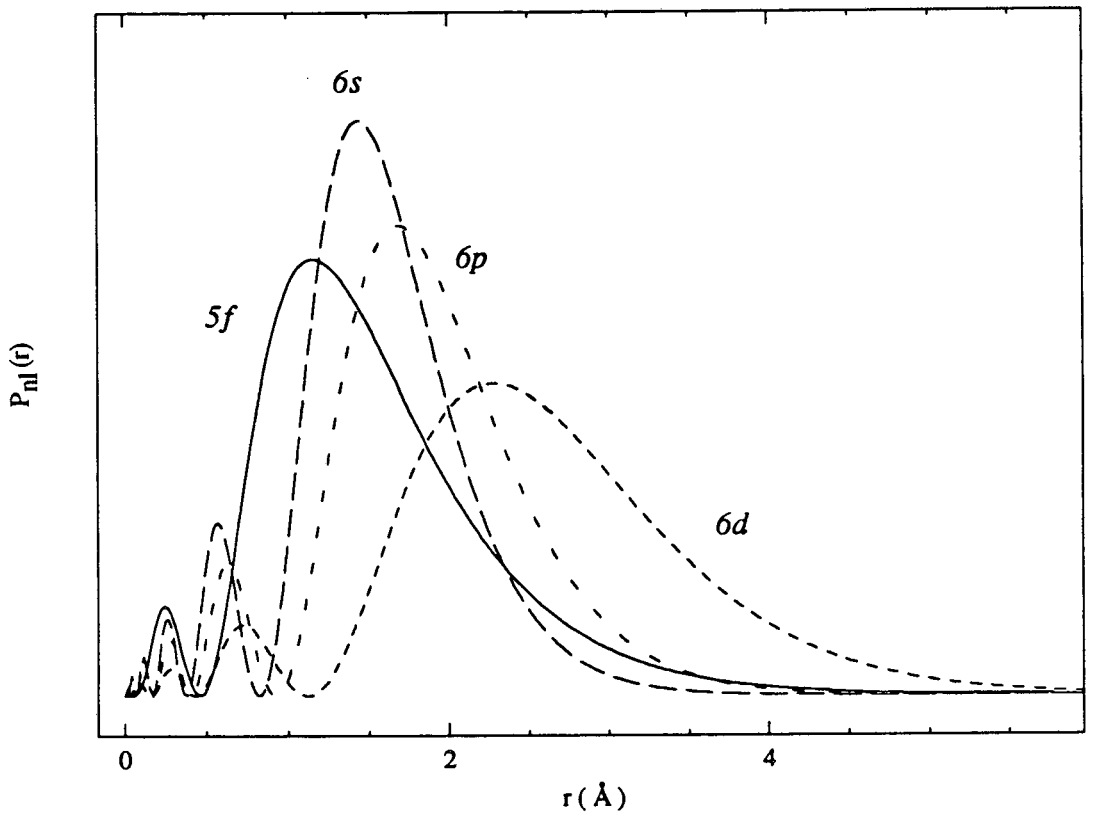

FIGURE 3.9 Radial distribution of the $5f$, $6d$, $7s$ and $7p$ wavefunctions of Th^{3+} from a Hartree-Fock calculation (From Ref. 27).

Secondly, the center of gravity of the d^1 configuration is lowered relative to that of the f^1 in a crystal field. Again this has been observed mostly in Ce^{3+}. In the Ce^{3+} free ion, the separation of the two centers of gravity is approximately 50,000 cm^{-1} [30], but shifts to ≈ 40,000 cm^{-1} [29] in Ce^{3+}:$LuPO_4$ and is even smaller at ≈ 35,000 cm^{-1} in Ce^{3+}:$YAlO_3$ [31]. The lowest energy band of the $f^n \rightarrow f^{n-1}d$ transition has been measured for the entire trivalent lanthanide series in CaF_2 [32] as well as for Pa^{4+} in $ThBr_4$ and $ThCl_4$ [33], they are found to be 18,000–20,000 cm^{-1} lower than the corresponding transition in the free ions. A similar shift has also been known to exist in other inter-configuration transitions such as the $6s^2 \rightarrow 6s6p$ transition in Tl^+, Pb^{2+} and Bi^{3+}[34]. It is noted with interest that the formally Laporte forbidden $d^{10} \rightarrow d^9s$ transition occurs at a higher energy in $Cu(NH_3)_2^+$ than in the Cu^+ free ion. This energy shift

cannot be explained by a purely electrostatic crystal-field model. Jørgensen and others have tried to correlate this shift with the "nephelauxetic effect" —— the reduction of interelectronic repulsion in a complex compared to the free ion —— an effect closely parallel to the tendency to form covalent bonding. For example, a metal *s* orbital is σ-antibonding in any symmetry while the *p* orbitals can be σ-, π-antibonding or nonbonding, depending on the symmetry of the compound. Thus the lowering of the $6s^2 \rightarrow 6s6p$ transition observed in thalium (I) halides compared to the free ion can be ascribed to the formation of covalent bond which destabilizes the *s* orbital more than the *p*. However, due to the various contributions to the nephelauxetic effect which are not easily separable experimentally, such correlations have only met with a varying degree of success and are at best qualitative. Athough there is only one single outermost electron in Th^{3+} and there is no interelectronic repulsion to speak of, as a manifestation of the inadequacy of the ionic crystal-field model, the relative energy shift between different configurations is expected to be important in the electronic structure of Cp''_3Th and In_3Th.

All these arguments suggest that the $6d^1$ configuration may compete favorably with the $5f^1$ as the ground electronic state in Cp''_3Th and In_3Th. The $7s^1$ configuration, at over 20,000 cm^{-1} away and not split by the crystal-field, is not expected to be important. *No* actinide compound with a ground configuration other than $5f^n$ is known. Indeed, the EPR results described in Sections 3.2 and 3.3 clearly indicate that the ground state does arise from the $6d^1$ configuration in Cp''_3Th and In_3Th. As discussed in Chapter 2, because of rapid spin-lattice relaxation, a $5f^1$ ground configuration will result in no room temperature spectrum and the *g*-values will be markedly different than 2.00. If the $7s^1$ configuration is lowest, only an isotropic $g = 2.00$ will be observed. As a comparison, EPR spectra of the $5f^1$ series Pa^{4+}, U^{5+} and Np^{6+} have all been measured in various matrices (no $5f^1$ complex with D_{3h} symmetry is known), invariably liquid-nitrogen or even lower temperature is required for observation of a spectrum; and the ground states all arise from the $5f^1$ $J = 5/2$ manifold with *g*-values ranging from 0.6 to 1.2 [36], the exact value depends on the crystal field. On the other hand, the EPR spectrum of $Ti[N(tms)_2]_3$ [37], a compound also with D_{3h} symmetry, is essentially identical to those of Cp''_3Th and In_3Th. Observation in a compound of a ground configuration that is different than the free ion ground configuration has been reported before —— the free ion Ce^{2+} has a ground

configuration of $4f^2$ whose lowest state is 3,277 cm^{-1} below that of the $4f5d$, but the ground confiuration in Ce^{2+}:CaF_2 is $4f5d$ and the lowest $4f^2$ state is now 7,080 cm^{-1} away [38]. Four years before the experimental confirmation, Wybourne had predicted a $4f5d$ ground state for Ce^{2+} in the solid state [39].

The coordination environment around the metal ion in Cp''_3Th is best described as D_{3h}, and the d orbitals will split accordingly : d_{z2} (a_1'), $d_{xz,yz}$ (e'') and $d_{x2-y2,\ xy}$ (e'). The observed EPR spectra indicates a $^2A_1'$ ground state. If an $^2E'$ or $^2E''$ state is lower, the increased spin-lattice relaxation would cause broadening of the spectrum, possibly to the point of making the room temperature spectrum unobservable. The peak width observed with Cp''_3Th, however, shows little change from room temperature to 10 K. Simple crystal-field arguments show that the e'' orbitals are the lowest with the a_1' low-lying [40]. However, the metal a_1' orbital does not interact with the π-orbitals of the ligands; the lowest π-level of the Cp^-, of a_1' symmetry, is stabilized mostly by interaction with the metal $7s$ (a_1') orbital while the metal e'' orbitals are greatly destabilized by the next π-level of the ligands, with the result that the metal a_1' orbital becoming the lowest-lying. Although the crystal field is of C_{3v} symmetry in the case of In_3Th, the same qualitative arguments are equally valid. With no axial ligand, the d_{z2} orbital, now of a_1 symmetry, should still be lowest although more admixture from the excited states is expected. This is observed in the broader peak widths found for In_3Th (14 G vs. 8 G for Cp''_3Th).

Quasi-relativistic Xα calculations have been carried out on Cp_3An (An = Th to Pu) [40]. Interestingly, both planar D_{3h} and pyramidal C_{3v} symmetries have been considered. It was found that the d_{z2} orbital, unable to interact effectively with the Cp ligands because of the symmetry, is not destabilized by metal-ligand bonding and is low-lying in Cp_3Th, Cp_3Pa and Cp_3U. In the case of planar Cp_3Th, the a_1' orbital is ca. 1 eV lower than the lowest $5f$ orbital. The $6d$ a_1 orbital in pyramidal Cp_3Th is also found to be the lowest, thus confirming the above conclusion. This a_1' (or a_1 in C_{3v} symmetry) orbital, however, is highly hybridized with the $7s$ and $7p$ and is directed toward the axial posistion, forming an ideal acceptor and coordination by a fourth ligand may destabilize it above the $5f$ orbital (*vide infra*).

The absorption spectrum of Cp''_3Th shows in the vis-UV region three very strong peaks and a fourth peak that overlaps partially with an intense absoption edge. The very large

oscillator strengths measured (Table 3.2) suggest that the transitions are electric dipole allowed and/or charge transfer transitions. The spin-orbit coupling constant for the $6d$ configuration in Th^{3+} is 2,117 cm^{-1} and that for the $5f$ is 1,236 cm^{-1} [26] and so the centers of gavity of the two free-ion states, $^2F_{7/2}$ and $^2F_{5/2}$, are separated by 4,325.4 cm^{-1}. Moreover, relatively detailed crystal-field analyses have only been performed on Cp_3Ln (Ln = lanthanides) but the parameters obtained are unlikely to be applicable here. It is, however, expected that spin-orbit coupling and the crystal-field are both important in determining the electronic structure of both configurations

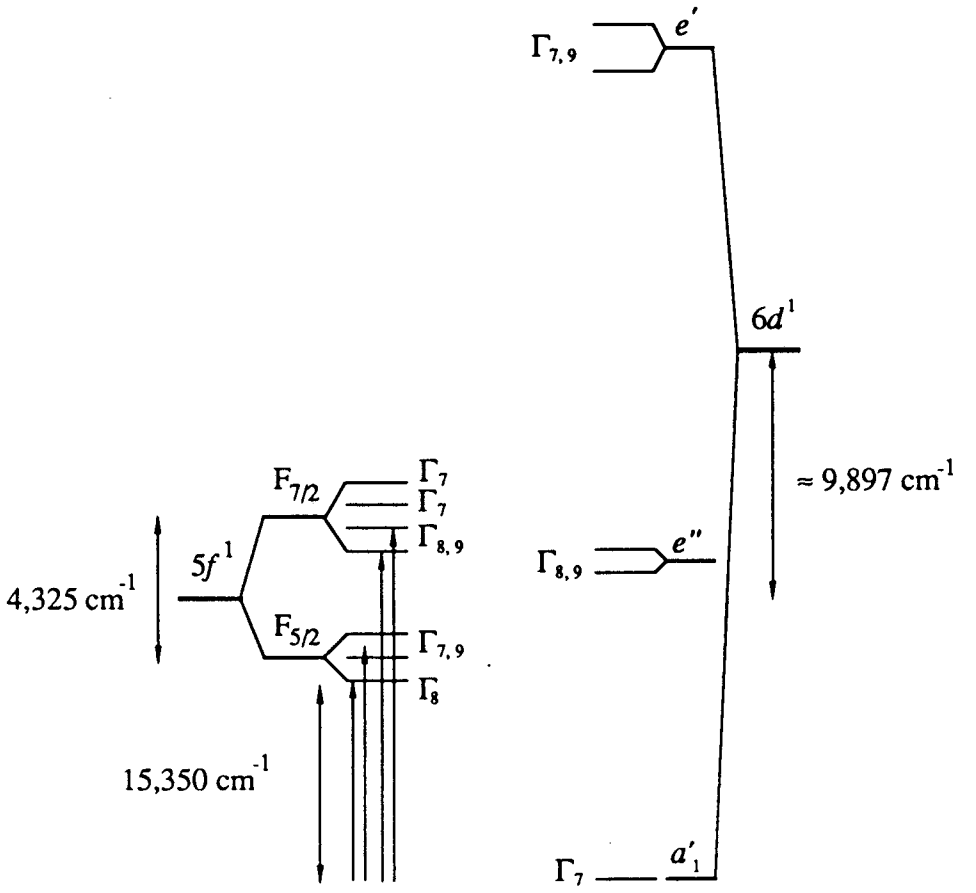

FIGURE 3.10 Schematic energy diagram of Cp''_3Th. Known energies are indicated, otherwise diagram is not drawn to scale and some of the energy orderings (e.g. crystal-field splitting of the $5f^1$ $^2F_{7/2}$ free ion manifold) are not known. Allowed electric-dipole transitions are represented by upward arrows.

which will then split into twelve states, leaving only Kramers degeneracies. All electronic states now carry symmetry labels corresponding to the irreducible representations of the double group $\overline{D}_{3h}$. A schematic energy diagram for both the $5f^1$ and $6d^1$ configurations is shown in Figure 3.10. The ground state has a symmetry of Γ_7 and the selcection rules for allowed transitions are $\Gamma_7 \rightarrow \Gamma_8, \Gamma_9$. Consequently, four strong transitions are expected. The absorption edge measured can be assigned as a metal to ligand charge transfer band. Of the four strong absorptions, the first three can be assigned as $6d \rightarrow 5f$ transitions with confidence but the fourth occurs at much higher energy than expected; assigning it as the fourth $6d \rightarrow 5f$ transition will place the separation between the centers of gravity of $^2F_{7/2}$ and $^2F_{5/2}$ at ≈ 9,000 cm^{-1} instead of 4,325 cm^{-1} and the total splitting of the $J = 7/2$ manifold will be greater than 12,000 cm^{-1}. A further complication arises as the $7s$ crystal-field state may also occur in the same region; the $7s$ configuration is only 12,000 cm^{-1} above the $6d$ in the free ion. While a $6d \rightarrow 7s$ transition is formally Laporte forbidden, unexpectedly large intensity has been observed for similar transitions [41]. As the temperature was lowered, all the transitions shifted to higher energy, showing the larger interaction and stablization of the d orbitals than those of the f orbitals due to the increased crystal-field. This is in contrast to the opposite temperature dependence that was observed in $f \rightarrow d$ transitions such as those in Ln^{3+}:CaF_2 [32].

As for the $6d^1$ configuration, again no previously studied system is useful as a guide. The compound $Ti[N(tms_2)]_3$ has a similar D_{3h} symmetry with no axial ligands but is expected to exhibit a very differnet crystal-field; its absorption spectrum shows that the E″ state is found at 4,800 cm^{-1} and the E′ state is at 17,400 cm^{-1} [20a]. A solution of Cp''_3Th with a much higher concentration (≈ 500 ×) than the one used before showed no additional absorption peak from 5,000 to 30,000 cm^{-1}. Fluorescence experiments at 10 K taking advantage of the strong allowed $5f \rightarrow 6d$ transition originating from the Γ_8 ($5f^1$) state also failed to locate any excited $6d$ crystal-field state; the detetactable energy ranges of the $6d$ states covered using a SPEX 1040 double monochromator and a Hamamatsu P819 PbS IR detector were 0–4000 cm^{-1} and 6,000–12,500 cm^{-1} respectively. While it is very likely that the E′ states may overlap with the $5f$ states, the E″ states is expected to be at < 10,000 cm^{-1}. A perturbation calculation, following Ballhausen [42], can be used to determine the g-values of the ground A_1' state which is mixed by spin-orbit coupling to the $A_1' - E''$ state using the energy separation and the orbital reduction

factor as parameters and the results are shown in Figure 3.11. It is seen that the E″ state is predicted at ≈ 8,000 cm^{-1}, a result that could not be confirmed by experiment.

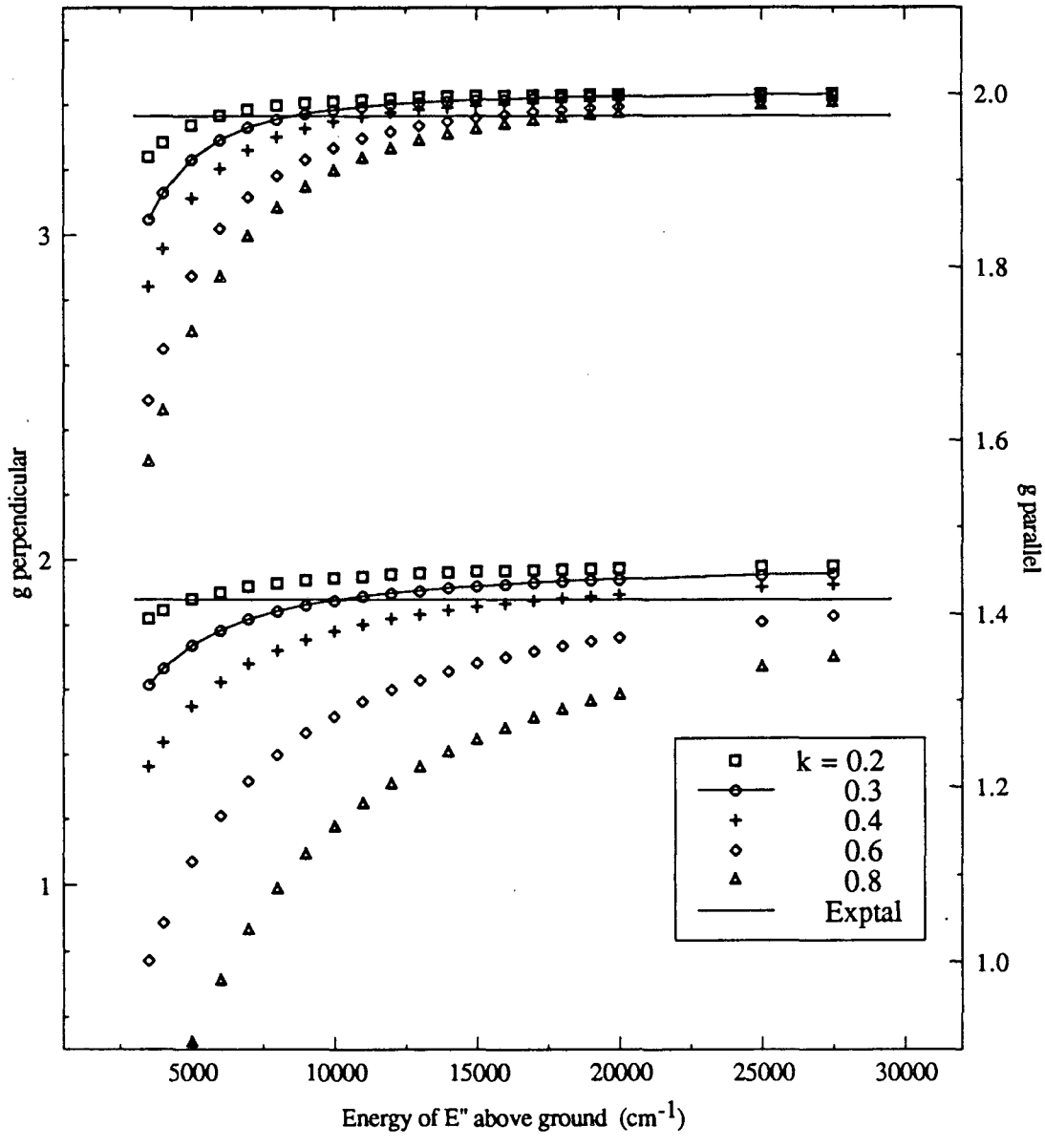

FIGURE 3.11 Calculated $g_{\parallel}$ (top, right scale) and $g_{\perp}$ (bottom, left scale) of the A_1' state in Cp''_3Th as a function of the A_1' – E″ energy separation and the orbital reduction factor *k*.

3.6 EPR of Ce^{3+} in Trigonal Symmetry

As mentioned in the previous section, no $5f^1$ complex with D_{3h} symmetry is known. However, complexes of Ce^{3+} with D_{3h} symmetry are not uncommon. While one cannot be sure about the ground electronic configuration of these complexes *a priori*, especially in view of the results presented above, it is highly unlikely that they will have a different ground configuration other than $4f^1$, remembering that the $4f$ is over 50,000 cm^{-1} lower than the first excited configuration $5d^1$ in the Ce^{3+} free ion. Nevertheless, these complexes are of interest as a comparison to the Th(III) results.

Stults *et al.* have synthesized Cp''_3Ce by treating $Ce[N(tms)_2]_3$ with Cp''H [10]. Its magnetic susceptibility has also been measured and found to be 2.28 μ_B for the temperature range 50 to 280 K, a value close to 2.54 μ_B predicted for a f^1 free ion. According to published procedure [44], $Ce[N(tms)_2]_3$ was prepared and its reaction with Cp''H [43] gave Cp''_3Ce in 45% yield. The EPR spectra of the blue powder was recorded and shown in Figure 3.12. No EPR signal was detected at room temperature but a strong signal was readily observed at < 50 K. The signal was rather broad (≈ 300 G) even at the low temperature of ≈ 4 K and from the peak shapes of the powder spectrum, $g_{\parallel}$ and $g_{\perp}$ caould be assigned the values of 2.39 and 2.77 respectively. These values are consistent with the susceptibility data, but a more detailed analysis of the crystal-field states for Cp''_3Ce is not possible without more data. However, it is obvious that the EPR of Cp''_3Th and Cp''_3Ce are qualitatively different and that while the two compounds are isostructural, they are not "isoelectronic" in the sense that Cp''_3Th has a $6d^1$ ground configuration but that of Cp''_3Ce is not $5d^1$.

EPR of $Ce[N(tms)_2]_3$ in the solid state is shown in Fig 3.13. The structure of $Ce[N(tms)_2]_3$ in the gas phase was determined to be C_{3v}, with the N–Ce–N angle equal to 117.5° [44]. Again very low temperature (≈ 20 K) was required for the observation of the very broad signal with a g-value of ≈ 2.2, suggesting that the ground configuration is $4f^1$. Yet this spectrum is noteworthy because of the fine structure which is only partially resolved and a rather different g-value than that of Cp''_3Ce. The difference in g-values indicates that the crystal-fields are very different in the two, despite the fact that they both possess very similar molecular symmetries. Absorption and EPR spectra of $M[N(tms)_2]_3$ (M = Ti, Cr, Fe, Gd) have

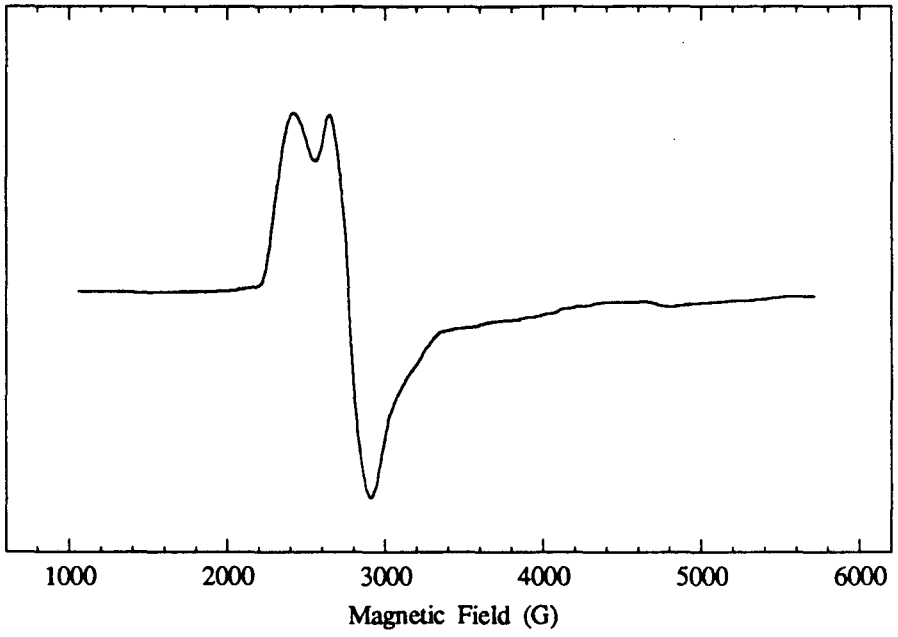

FIGURE 3.12 EPR spectrum of Cp''_3Ce in the solid state. Microwave frequency = 9.227 GHz, temperature = 4K.

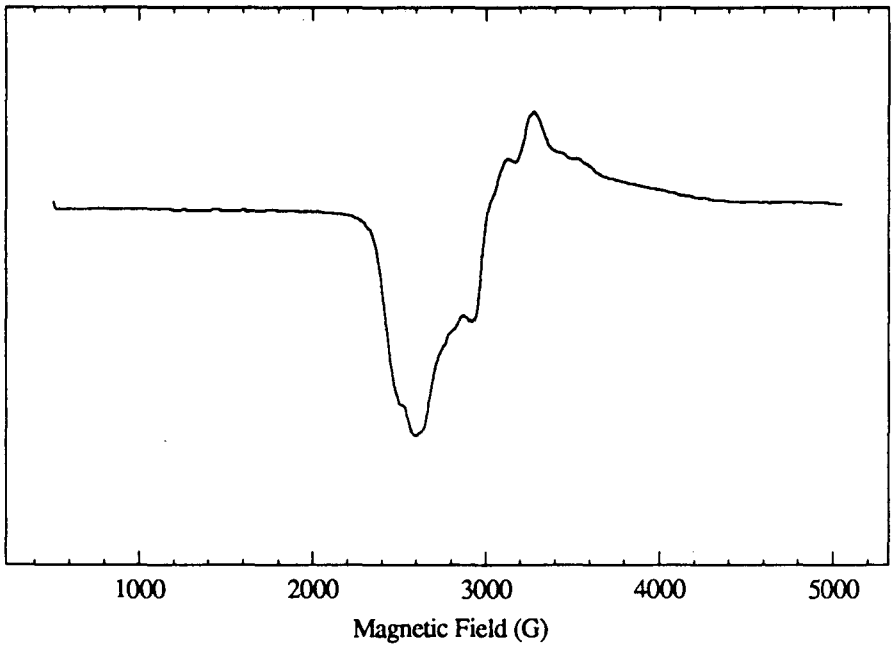

FIGURE 3.13 EPR spectrum of $Ce[N(tms)_2]_3$ in the solid state. Microwave frequency = 9.238 GHz, temperature = 2.8 K.

been studied before and it is found that the ZFS and the crystal-field parameters are in general very large [45]; the ZFS of $Gd[N(tms)_2]_3$ is 4.66 cm^{-1} [46], an order of magnitude larger than any of the previously reported (see Table 2.2). It is then argued because of the strongly nucleophilic nature of the ligand $(tms)_2N^-$, the M–N bond can be expected to have a high degree of covalent character, resulting in an unusually large crystal-field. The EPR spectrum of $Ti[N(tms)_2]_3$ also shows an unresolved fine structure, but is thought to be the hyperfine structure due to the nuclei ^{47}Ti and ^{49}Ti [36]. None of the four natural isotopes of Ce has a nuclear spin and any fine structure can only originate from interaction with the ^{14}N nuclei. Superhyperfine interaction is little known in the lanthanides; bonding in the lanthanides is normally considered ionic because the $4f$ electrons are well shielded. The powder spectrum does not show a well resolved seven-line pattern; simulation is not helpful because too many parameters are unknown (e.g. peak width, coupling constant and unresolved components of the g-tensor). Attempts to reduce the peak widths by doping $Ce[N(tms)_2]_3$ into $La[N(tms)_2]_3$ were unsuccessful and the same spectrum was observed. While the coupling constant appears to be very large from the spectrum and no definite conclusion can be drawn, $Ce[N(tms)_2]_3$ certainly deserves further study (e.g. by ENDOR).

The absorption spectrum of Cp''_3Ce in the UV-vis region is shown in Figure 3.14. Two very strong and broad bands were observed in addition to an edge which can be again be assigned as a charge transfer band. The two broad bands are centered at 17,650 and 22,125 cm^{-1} with measured oscillator strengths of 2,725 and 870×10^{-6} respectively. The energy diagram of Cp''_3Ce is similar to that of Cp''_3Th shown in Figure 3.10, except that the free-ion $5d$ configuration is now over 50,000 cm^{-1} above that of the $4f$ (Fig 3.8) and the ground electronic state is Γ_8 (f^1, $^2F_{5/2}$). Allowed electric-allowed transitions are $\Gamma_8 \rightarrow \Gamma_7$, Γ_9 and so three to four strong $f \rightarrow d$ transitions are expected, depending on the peak widths and the separation of the states arising from the E′ states. The total splitting of the $5d^1$ configuration is expected to be larger than 15,000 cm^{-1} and so the transition to the E′ ($\Gamma_{7,9}$) states should occur at an energy beyond 30,000 cm^{-1}. The band centered at (520 nm) ≈ 17,650 cm^{-1} can be assigned as $\Gamma_8 \rightarrow \Gamma_7$. Piehler has collected values of the $f \rightarrow d$ transition energies found for Ce^{3+} in various matrices [47], the lowest $f \rightarrow d$ band occurred in $Ce^{3+}:Y_3Al_5O_{12}$ (YAG) at ≈ 22,000 cm^{-1} [48].

The $f \rightarrow d$ absorption bands found in $Ce^{3+}:Y_3Al_5O_{12}$ are included in Figure 3.14 for comparison. Thus it is seen that the site symmetries in Cp''_3Th and Cp''_3Ce, with no axial ligands, give extra stablization to the d_{z^2} orbitals. In the case of Cp''_3Ce, it gives rise to the lowest $f \rightarrow d$ transition ever observed while for Cp''_3Th, the $6d$ becomes the ground electronic configuration.

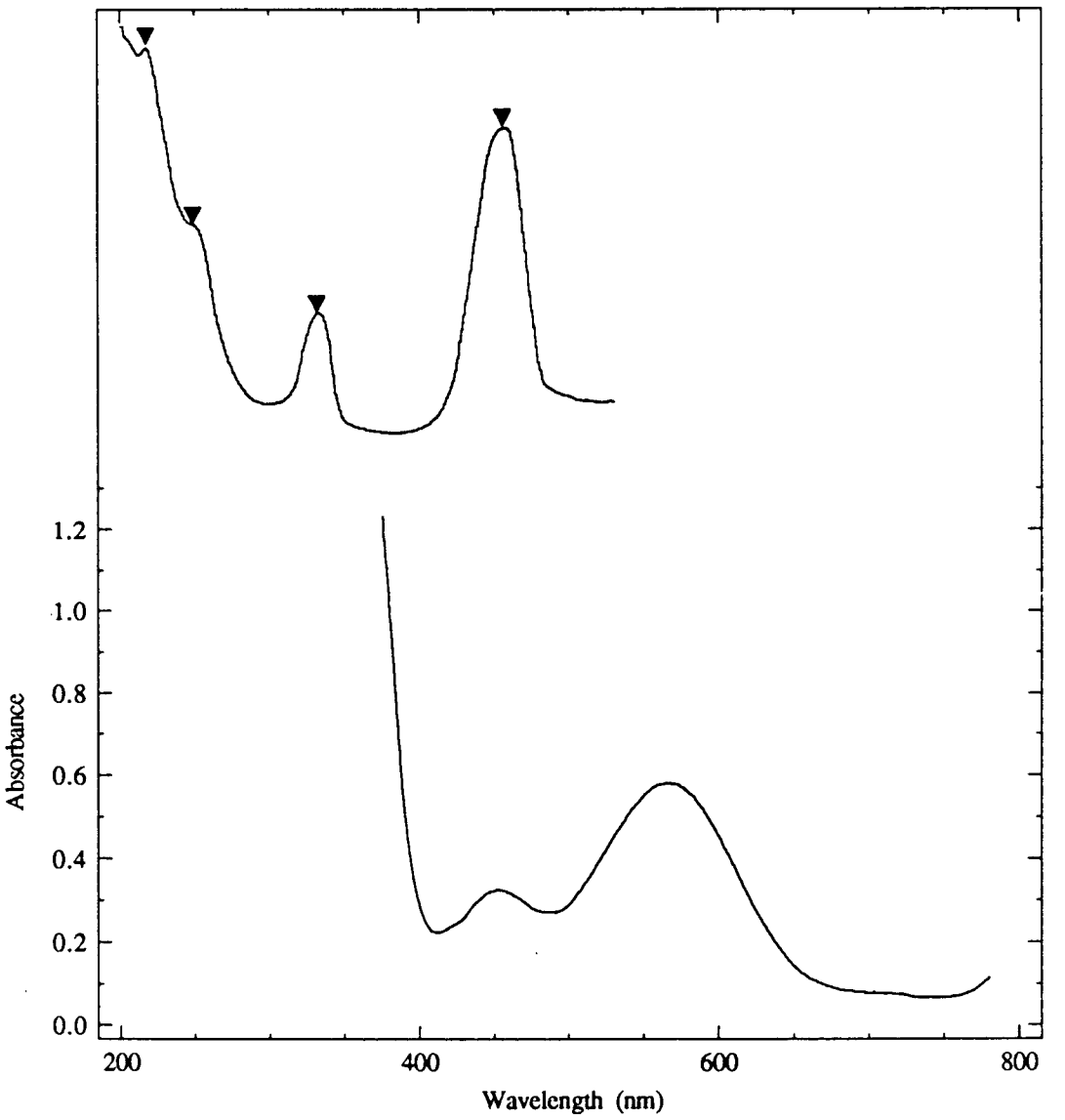

FIGURE 3.14 Absorption spectrum of Cp''_3Ce in MCH at room temperature. Concentration of solution = 4.77×10^{-4} M and path length = 1 cm. Included for comparison is the $f \rightarrow d$ transitions (marked with arrows) found in $Ce^{3+}:Y_3Al_5O_{12}$(YAG) (Ref. 48).

3.7 Attempts to Prepare Lewis Base Adducts of Cp''_3Th

Coordination chemistry involving $Cp_3M{\cdot}L$ (M = lanthanides and actinides, L = Lewis base) has received much study and proved to be a fruitful area of research. While coordination chemistry of Cp''_3Th is very interesting in its own right, complexes of the kind $Cp''_3Th{\cdot}L$ are relevant in the present context because, as alluded to in Section 3.5, the d_{z2} orbital is an ideal electron acceptor and coordination by a Lewis-base ligand may destablize it such that the $5f$ may become the ground elecronic configuration as in the free ion.

In attempts to prepare $Cp''_3Th{\cdot}L$, a series of N-, O- and P- ligands were reacted with Cp''_3Th. No reaction was observed to take place. Lewis bases employed included the following: C_2H_5CN, $(C_2H_5)_3N$, C_6H_5N, $(CH_3)_3PO$, C_4H_8O, $(C_2H_5)_2O$, $(CH_3)_3P$, $(CH_3O)_3P$ and CO all of which form stable adducts with $(RC_5H_4)_3U$ (R = CH_3, tms) [49]. In a typical reaction, the ligand was added to a MCH solution of Cp''_3Th with stirring; no observable change occurred and the resulting solution gave identical EPR and optical spectra as the base free Cp''_3Th. The reaction was then heated gradually up to ≈ 100° C, still no detactable change was observed.

The inability to isolate $Cp''_3Th{\cdot}L$ can in large part be attributed to steric congestion. The extent to which Cp''_3Th is kinetically stablilized by the use of bulky Cp″s can be gauged by the non-existence of Cp_3Th and MO studies which show that, in Cp_3An, the $6d_{z2}$ orbital is stabilized by pyramidalization because of increased hybridization with the $7p_z$ [50]; a C_{3v} Cp''_3Th would be more stable than one with D_{3h} symmetry for electonic reasons alone but its structure was determined to be trigonal planar. For the isostructural Cp''_3Ce, the only adduct reported is prepared with a 'stick-like' ligand, *t*-butyl isocyanide, to give $Cp''_3Ce{\cdot}CN^tBu$ [10]. The structure of $Cp''_3Ce{\cdot}CN^tBu$ indicates no perturbation to the trigonal framework of the Cp''_3Ce fragment by the coordination of the Lewis base; the Cp″–Ce–Cp″ angles are 119.5° in the adduct and 119.7° in the base-free compound, demonstrating the sterically demanding nature of the Cp″ ligand. It is not understood why sterically non-demanding ligands like C_2H_5CN and $(CH_3)_3PO$ did not show any reaction with Cp''_3Th.

A reaction was indeed observed with *t*-butyl isocyanide when the blue colored solution of Cp''_3Th decolorized immediately upon contact with the ligand. The colorless solution gave

no EPR spectrum at room or cryogenic temperature; no absorption spectrum in the UV-vis region was detected up to 28,000 cm^{-1}. Pale yellow crystals could be isolated from the solution and were analyzed to be Cp''_3ThCN by IR, NMR and mass spectroscopies. The mass spectrum showed a parent ion at 885 (relative intensity = 1.8) with fragmentations found at 870 $(M–CH_3)^+$ (1.5) and 676 $(M–Cp'')^+$ (45). The ν_{CN} stretch was found at 2,155 cm^{-1}. This number can be compared to 2,096 – 2,125 cm^{-1} found for the uranium analogues with various Cp's.

Reduction of isocyanides normally involves addition to the C≡N multiple bonds, reducing agents like $LiAlH_4$ react with isocyanides to give N-methylamines. Reductive cleavage of the C–N single bond to give cyanide anions, though not unknown, can only be accomplished under rather harsh conditions such as Li or Na in liquid ammonia [51]:

$$RNC + 2\,Li + NH_3 \longrightarrow LiCN + LiNH_2 + RH$$

Thus the formation of Cp''_3ThCN demonstrates the powerful reactivity of Cp''_3Th. Similar reductive cleavage of isocyanides by an organometallic has only been reported for the low-valent $(C_5Me_5)_2Sm(THF)_2$ [52], a compound noted for its extremely high reactivity. Most of the reactivity of $(C_5Me_5)_2Sm(THF)_2$ can be described as that of a one-electron reducing agent, resulting in Sm(III) species [53]. The reduction potential for Sm(III) → Sm(II) is –1.50 V while that for Th(IV) → Th(III) was estimated to be as high as –3.70 V [8]; Cp''_3Th can therefore be expected to undergo similar reactions as $(C_5Me_5)_2Sm(THF)_2$, but with an even greater reducing power.

Because of the steric demands and the extremely high reducing power of Cp''_3Th, its coordination chemistry probably is not as rich as that found in compounds such as $(MeCp)_3U$; no adduct of the type $Cp''_3Th{\cdot}L$ could be isolated. The prediction that $Cp''_3Th{\cdot}L$ possesses a $5f^1$ ground configuration consequently remains to be tested.

3.8 Summary

Uncommon electronic properties that occur in uncommon oxidation states of the lanthanides, especially at the beginning of the series, have been reported and studied years earlier [38]. A similar situation is now found to also exist in the actinides —— trivalent thorium in a crystal-field of D_{3h} or C_{3v} symmetry has a $6d^1$ ground configuration, states arising from the $5f^1$ configuration in Cp''_3Th are found to be over 15,000 cm^{-1} away. Theoretical calculations have arrived at the same conclusion [40]. This represents the first instance where the ground configuration in an actinide compound is observed to be $6d^1$. Cotton and Wilkinson [54] might have anticipated it when they wrote that electronic energies between different congurations in the actinides "may lie within the range of chemical binding energy. Thus the electronic structure of the element in a given oxidation state may vary between compounds."

In going from the Th^{3+} free ion to Cp''_3Th, the lowest d state is stablized by ≈ 25,000 cm^{-1} compared to the lowest f state. This relatively large shift can partly be ascribed to the symmetry of the crystal-field with no axial ligands, giving extra stabilization to the d_{z2} orbital; while the ground configuration of Ce^{3+} in a similar crystal-field is still $4f^1$, the d levels occur at a lower energy than was ever found previously in any symmetry. Low-lying d levels are found to be of primary importance in many spectroscopic processes in the lanthanides [29]. The interest in the further study of trivalent thorium, especially in compounds with a symmetry other than D_{3h} and C_{3v}, is obvious. Its study, unfortunately, is severely hampered by the difficulty in synthesizing and characterizing new Th(III) compounds —— the inability to isolate Lewis-base adducts $Cp''_3Th{\cdot}L$ being a case in point —— and the less-than-ideal experimental conditions in spectroscopic studies of organometallics (e.g. the lack of suitable single crystals). Generation of Th^{3+} in a single crystal (e.g. by γ-irradiation) should prove to be an appealing alternative.

References

[1] E. D. Eastman, L. Brewer, L. A. Bromley, P. W. Giles and N. L. Lofgren, J. Am. Chem. Soc. **72**, 4019 (1950).

[2] J. L. Smith and L. Kmetko, J. Less-Common Metal **90**, 83 (1983).

[3] B. Kanellakopulos, E. Dornberger and F. Baumgärtner, Inorg. Nucl. Chem. Lett. **10**, 155 (1974).

[4] D. G. Kalina, T. J. Marks and W. A. Wachter, J. Am. Chem. Soc. **99**, 3877 (1977).

[5] R. G. Finke, G. Gaughan and R. Voegeli, J. Organomet. Chem. **104**, 1860 (1982).

[6] J. W. Bruno, D. G. Kalina, E. A. Mintz and T. J. Marks, J. Am. Chem. Soc. **104**, 1860 (1982).

[7] A. M. Koulkes-Pujo, J. F. Le Marechal, A. Dormond and G. Folcher, Inorg. Chem. **26**, 3171 (1987).

[8] L. J. Nugent, R. D. Baybarz, J. L. Burnett and J. L. Ryan, J. Phy. Chem. **77**, 1528 (1973).

[9] P. C. Blake, M. F. Lappert, J. L. Atwood and J. Zhang, J. Chem. Soc. Chem. Commun., 1148 (1986).

[10] S. D. Stults, R. A. Andersen and A. Zalkin, Organometallics **9**, 115 (1990).

[11] (a) C. Wong, T. Yen and T. Lee, Acta Crystallogr. **18**, 340 (1965). (b) J. H. Burns and P. G. Laubereau, Inorg. Chem. **10**, 2789 (1971).

[12] W. E. Rhine and G. D. Stucky, J. Am. Chem. Soc. **97**, 737 (1975).

[13] J. Rebizant and M. R. Spirlet, Acta Crystallogr. **C42**, 1497 (1986).

[14] J. Goffart and S. Bettonville, J. Organomet. Chem. **361**, 17 (1989).

[15] J. Meunier-Piret, J. P. Declercq, G. Germain and M. Van Meerssche, Bull. Soc. Chim. Belg. **89**, 121 (1980).

[16] P. G. Laubereau, L. Ganguly, J. H. Burns, B. M. Benjamin, J. L. Atwood and J. Selbin, Inorg. Chem. **10**, 2274 (1971).

[17] J. Goffart, B. Gilbert and G. Duyckaerts, Inorg. Nucl. Chem. Lett. **13**, 189 (1977).

[18] (a) I. L. Fragalà, J. Goffart, G. Granozzi and E. Ciliberto, Inorg. Chem. **22**, 216 (1983). (b) I. L. Fragalà, E. Ciliberto, R. D. Fischer, G. R. Sienel and P. J. Zanella, J. Organomet. Chem. **120**, C9 (1976).

[19] (a) S. Ohnishi, T. Tadayoshi and I. Nitta, J. Chem. Phys. **37**, 2402 (1962). (b) R. W. Fessenden and R. H. Schuler, J. Chem. Phys. **39**, 2147 (1963). (c) A. Atto, A. Hudson, R. A. Jackson and N. P. C. Simmons, Chem. Phys. Lett. **33**, 477 (1975).

[20] (a) D. C. Bradley, J. S. Ghotra and A. A. Hart, J. Chem. Soc. Dalton Trans., 1021 (1973). (b) R. A. Andersen, D. H. Templeton and A. Zalkin, Inorg. Chem. **17**, 2317 (1978). (c) R. A. Andersen, Inorg. Chem. **18**, 1507 (1979).

[21] S. J. Simpson, H. W. Turner and R. A. Andersen, Inorg. Chem. **20**, 2991 (1981).

[22] D. C. Bradley, H. Chudzynska, J. D. J. Backer-Dirks, M. B. Hursthouse, A. A. Ibrahim, M. Motevalli and A. C. Sullivan, Polyhedron **9**, 1423 (1990).

[23] A. B. P. Lever, *Inorganic Electron Spectroscopy*, (Elsevier, Amsterdam, 1968), p. 124.

[24] W. T. Carnall in *Organometallics of the f-Elements*, edited by T. J. Marks and R. D. Fischer (D. Reidel, Dordrecht, 1979).

[25] K. S. Pitzer, Acc. Chem. Res. **12**, 271 (1979).

[26] P. F. A. Klinkenberg and R. J. Lang, Physica **15**, 774 (1949).

[27] N. Edelstein, personal communication.

[28] D. J. Ehrlich, P. F. Moulton and J. R. M. Osgood, Opt. Lett. **5**, 339 (1980).

[29] G. M. Williams, Ph. D. Dissertation, Universtiy of California at Berkeley (1988).

[30] R. J. Lange, Can. J. Res. A **14**, 127 (1935).

[31] M. J. Weber, J. Appl. Phys. **44**, 3205 (1973).

[32] E. Loh, Phys. Rev. **147**, 332 (1960).

[33] (a) J. C. Krupa, M. Hussonnois, M. Genet and R. Guillaumont, J. Chem. Phys. **77**, 154 (1982). (b) N. Edelstein, J. C. Krupa, R. C. Naik, K. Rajnak, B. Whittaker and D. Brown, Inorg. Chem. **27**, 3186 (1988).

[34] (a) F. Seitz, J. Chem. Phys. **6**, 150 (1938). (b) A. K. MacBeth and N. I. Maxwell, J. Chem. Soc. 370 (1923).

[35] R. Reisfeld and C. K. Jørgensen, *Lasers and Excited States of Rare Earths*, (Springer Verlag, Berlin, 1977).

[36] L. Boatner and M. M. Abraham, Rep. Prog. Phys. **41**, 87 (1978).

[37] D. C. Bradley, R. G. Copperthwaite, S. A. Cotton, K. D. Sales and J. F. Gibson, J. Chem. Soc. Dalton Trans., 191 (1973).

[38] (a) D. S. McClure and Z. Kiss, J. Chem. Phys. **39**, 3251 (1963). (b) R. C. Alig, Z. J. Kiss, J. P. Brown and D. S. McClure, Phys. Rev. **186**, 276 (1969). (c) A. Kiel and J. F. Scott, Phys. Rev. B **2**, 2033 (1970).

[39] B. G. Wybourne, *Spectroscopic Properties of the Rare Earths*, (Wiley, New York, 1965).

[40] See, for example, J. K. Burdett, *Molecular Shapes*, (Wiley-Interscience, New York, 1980), p.133.

[41] B. E. Bursten, L. F. Rhodes and R. J. Strittmatter, J. Am. Chem. Soc. **111**, 2756 (1989).

[41] C. K. Jørgensen, *Absorption Spectra and Chemical Bonding in Complexes*, (Pergamon, Oxford, 1962).

[42] C. J. Ballhausen, *Introduction to Ligand Field Theory*, (McGraw Hill, New York, 1962), p.133.

[43] Synthesis by S. Stults.

[44] T. Fjeldberg and R. A. Andersen, J. Mol. Struct. **129**, 93 (1985).

[45] J. S. Wood, Inorg. chem. **7**,852 (1968).

[46] D. S. Katoch and K. D. Sales, J. Chem. Soc. Dalton Trans., 2476 (1980).

[47] D. Piehler, Ph. D. Dissertation, Universtiy of California at Berkeley (1990).

[48] W. J. Miniscales, J. M. Pellegrino and W. M. Yen, J. Appl. Phys. **49**, 6109 (1978).

[49] J. G. Brennan, Ph. D. Dissertation, University of California at Berkeley (1985).

[50] K. Tatsumi and A. Nakamure, J. Organomet. Chem. **272**, 141 (1984).

[51] I. Ugi and F. Bodesheim, Chem. Ber. **94**, 1157 (1961).

[52] W. J. Evans and D. K. Drummond, Organometallics **7**, 797 (1988).

[53] W. J. Evans, Polyhedron **6**, 803 (1987).

[54] F. A. Cotton and G. Wilkinson, Advanced Inorganic Chemistry, Fifth Edition (Wiley-Interscience, New York, 1988), p. 983.

Chapter 4

Synthesis, Electronic Structure and NMR Studies of $Pa(BH_3CH_3)_4$

4.1 Introduction

"Actinide research has presented unique challenges both for experimentalists and theorists ... these elements have "unfortunate properties" —— scarcity, radioactivity, toxicity and reactivity —— which cause severe complications for their preparation and handling. The unusual behavior of their *5f* electrons —— which causes questions such as localization versus delocalization to come to the forefront —— has added complexity not found in the other elements," so wrote Freeman in *Handbook on the Physics and Chemistry of the Actinides* [1]. Perhaps the one actinide that most exemplifies these "unique challenges" and "unfortunate properties" is protactinium.

Protactinium is the first actinide in which the *5f* shell is occupied in both the metal and compounds with a common oxidation state. As already mentioned in Section 3.1, the *5f* electrons are involved in bonding in the earlier actinide metals; experiments and calculations have shown this to be the case up to plutonium while electrons in heavier actinides are localized, much like a rare-earth metal [2]. The delocalized nature of the *5f* electrons in the early actinides also manifests itself in stoichiometric and molecular compounds. In the low-valent Pu^{3+}:CaF_2, superhyperfine interaction with the fluoride ions is known [3]. For tetravalent protactinium, the high transition temperature of 182 K at which $PaCl_4$ becomes ferromagnetic, compared to the

Curie temperature of 6.7 K for the isostructural $NpCl_4$ [4], is perceived as a great degree of covalency [5]; $PuCl_3$ becomes antiferromagnetic only at 4.5 K [6]. With its relatively large radial distribution, the sole unpaired *5f* electron in Pa^{4+} is expected to undergo extensive interaction with the ligands. Moreover, with a low-lying *6d* configuration (see Fig 3.8), Pa^{4+} is also of special interest spectroscopically.

In spite of the apparent interest in the chemical nature and the spectroscopic properties of protactinium, progress has been generally slow in virtually every experimental aspect about it. For example, after the first report that protactinium metal is superconducting below 1.4 K [7], and despite a firm theoretical guide [8], it took almost 15 years and a number of unsuccessful attempts before the result could be reproduced, thus confirming that protactinium is a true actinide [9]. This undoubtedly is due to the many "unfortunate properties" associated with the element.

Protactinium is one of the rarest naturally-occurring elements. The only isotope amenable to chemical study is ^{231}Pa which, being the granddaughter of ^{235}U, is present in many different minerals; but only at a very low concentration of ≈ 0.3 ppm [10]. Recovery of ^{231}Pa is difficult and tedious. Furthermore, its production by nuclear reactions is not practical owing to the high cross-sections of the competing reactions. Consequently, less than 150 g of ^{231}Pa has ever been isolated. Availability of Pa turned out to be the primary problem for the present study, a total of less than 600 mg was made available after much effort whereas, as a comparison, $\geq$ 10 g each of ^{237}Np and $^{239,242}Pu$ was accessible. The half-life of ^{231}Pa is 34,300 *y* and it decays solely through α-emission. While its relatively high specific α-activity does not entail any extra precaution in its handling than, say, ^{237}Np and $^{239,242}Pu$, many of its decay daughters are high-energy β- and γ-emitters (e.g. ^{227}Ac, ^{227}Th and ^{211}Pb), adding further complications to its manipulation. Even with much shielding and use of tongs whenever possible, no more than 50 mg of ^{231}Pa was handled at one time during this study.

The chemistry of Pa, with a stable pentavalent state, bears some resemblance to that of Nb and Ta; its tetravalent state is unstable toward oxidation by air and the trivalent state has been reported but is not well studied at all [11]. Comparison of Pa with Nb and Ta will be made throughout this chapter. In aqueous solution, the chemistry of Pa is even less tractable than that of Nb and Ta and "the difficulties are almost insuperable [12]" because of its high tendency to

hydrolyze and form polymeric species. This tendency to hydrolyze is carried over into non-aqueous media. For example, $PaCl_5$ is known to be soluble in THF but solvolysis and polymerization happen readily such that THF is not useful at all as a solvent for $PaCl_5$ (*vide infra*). This perhaps is expected of Pa^{5+}, with its very high charge to radius ratio, as an extremely hard acid but compounds problems associated with its study.

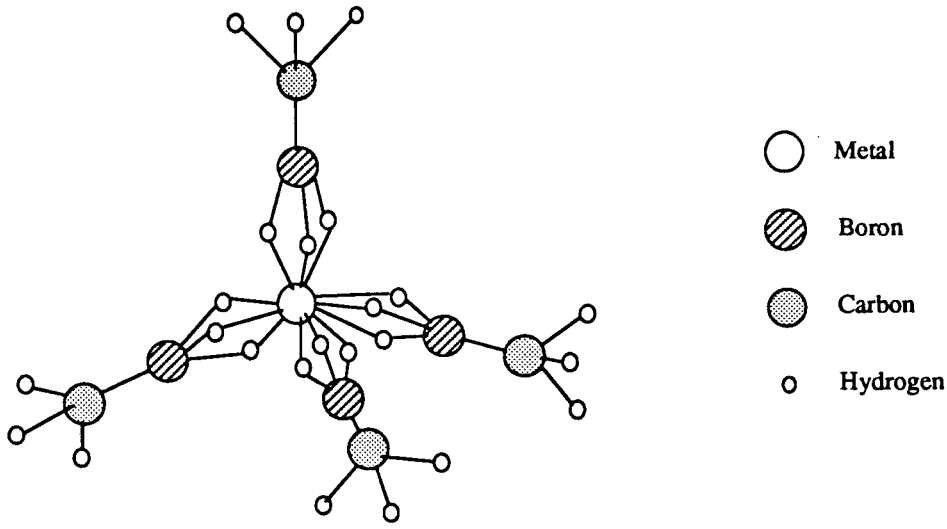

FIGURE 4.1 The $M(BH_3CH_3)_4$ (M = Zr, Hf, Th, U and Np) molecule showing the T_d symmetry about the metal.

Outside the regime of classical inorganic chemistry, few compounds of protactinium are known; only three organometallic compounds have ever been reported [13-15], the polymeric $Pa(BH_4)_4$ is also known [16]. This chapter describes the attempts to prepare $Pa(BH_3CH_3)_4$ and study of its electronic structure. Monomeric $M(BH_3CH_3)_4$ (M = Zr, Hf, Th, U and Np) are found to be highly volatile and possess rigorous T_d symmetry at the metal sites with four triply hydrogen-bridging methyltrihydroborato groups, resulting in a formal coordination of 12 (Fig 4.1). They are therefore of special spectroscopic interest. The paramagnetic $U(BH_3CH_3)_4$ [17] and $Np(BH_3CH_3)_4$ [18], and the structurally-similar $Np(BH_4)_4$

[18] and $U(BH_4)_4$:$Hf(BH_4)_4$ [19] have been studied extensively. Together they represent the few actinide molecular systems suitable for detailed electronic study; most other actinide compounds are either polymeric or of low-symmetry. No example of an f^1 crystal-field with T_d symmetry is known [20].

4.2 Reaction of $LiBH_3CH_3$ with Niobium and Tantalum Halides, Cs_2MCl_6 (M=Zr, U, Np, Pu) and $CsMCl_6$

The obvious synthetic route to $Pa(BH_3CH_3)_4$ is the reaction between $PaCl_4$ and $LiBH_3CH_3$, following the syntheses of the thorium and uranium analogues [21]. In view of the scarcity of and the intense radiation associated with Pa, however, it is sought to minimize its handling and multi-step syntheses should be avoided. Preparation of $PaCl_4$ involves reduction of $PaCl_5$ and the yield is known to be erratic [22, 23]. Alternate routes have been explored and this section summarizes them.

In addition to being good hydride sources, $LiAlH_4$, $LiBH_4$ and, to a lesser extent, $LiBH_3R$ (R = ethyl, *n*-butyl) are extensively used as reducing agents, especially in organic synthesis. They are used routinely to reduce esters and acyl halides to give alcohols. In certain cases, even conjugated carbon double bonds are found to be reduced by $LiBH_4$ [24], for example,

Reduction of $PaCl_5$ with $LiBH_3CH_3$ to give $Pa(BH_3CH_3)_4$ therefore appears to be a logical and attractive alternative. Pentahalides of niobium and tantalum were used as models for $PaCl_5$ in preliminary reactions. In addition, hexachloroprotactinates (IV) and (V) can be useful starting materials; they have the advantage of being relatively easy to prepare in high yield and they are more stable to the atmosphere than the halides. To further investigate the reducing properties of

$LiBH_3CH_3$, its reactions with chloro complexes of U(V), Np(IV) and Pu(IV) have been attempted.

Reactions of excess $LiBH_3CH_3$ with $NbCl_5$ and TaI_5 appeared to have begun even in the solid state, the white $LiBH_3CH_3$ turning bluish-gray upon contact with the halides. When solvent was added (chlorobenzene or diethyl ether), the reaction was vigorous, liberating large amount of heat and gas. A series of color changes were observed in the Nb reaction, the color changed from yellow to blue, then brown and finally black. The product in all cases was a black insoluble solid that did not sublime. Elemental analyses gave inconsistent results but both carbon and hydrogen were found to be present. The solid gave no EPR. Performing the reaction at –78° C apparently resulted in the same product.

There are few tetrahydroborate complexes of niobium; and none of tantalum is known. The niobium tetrahydroborates known are $(C_5H_5)_2Nb(Cl)BH_4$ [25], prepared from C_5H_5Na, $NbCl_5$ and $LiBH_4$, and $(C_5H_5)_2NbBH_4$ [26], obtained from reaction between $(C_5H_5)_2NbCl_4$ and $LiBH_4$. It is therefore seen that both the Nb(V)→Nb(IV) and Nb(IV)→Nb(III) reductions can be achieved by the use of $LiBH_4$. In addition, the use of Cp^- is thought to saturate the metal coordination sphere as attempts to isolate $Nb(BH_4)_3$ have been unsuccessful [27]. In view of these results and the fact that both Nb^{5+} and Ta^{5+} are highly electropositive, it is not surprising that $Nb(BH_3CH_3)_4$ or $Ta(BH_3CH_3)_4$ could not be isolated and the resulting black solids are probably low-valent polymeric hydrides. The trivalent state of protactinium is in general not as easily accessible as those of Nb and Ta; $Pa(BH_4)_4$ was known to exist and was isolated from the reaction between PaF_4 and $Al(BH_4)_3$ [28].

Cesium hexachlorozirconate (IV) and uranate (IV) reacted with $LiBH_3CH_3$ to give $Zr(BH_3CH_3)_4$ and $U(BH_3CH_3)_4$ respectively; the yields were ≈ 35%, comparable to those using $ZrCl_4$ and UCl_4 as starting materials [29]. Substituting $(CH_3)_4N^+$ or $(C_2H_5)_4N^+$ for Cs^+ did not improve the yield as the resulting complexes appeared to be equally insoluble in the solvent (chlorobenzene) as the cesium analogue. The pentavalent $CsUCl_6$ showed no reaction with excess $LiBH_3CH_3$ in CH_2Cl_2, but produced purple $U(BH_3CH_3)_4$ when diethyl ether or chlorobenzene was used as solvent. The yield was ≈ 30%. Reduction of U(V) to U(IV), not unexpectedly, appeared facile in diethyl ether because of the increased solubility of $LiBH_3CH_3$. The solvent assumed a green color within minutes, indicating the formation of

$U(BH_3CH_3)_4 \cdot OEt_2$; the etherate lost the coordinating solvent during sublimation. Reaction in chlorobenzene typically took much longer due to the low solubilities of the reactants.

In attempts to prepare $Np(BH_3CH_3)_4$ and $Pu(BH_3CH_3)_4$, tetravalent neptunium and plutonium species were used to react with $LiBH_3CH_3$. Stirring Cs_2NpCl_6 with excess $LiBH_3CH_3$ in chlorobenzene for two days resulted in no sublimable product but $NpCl_4$ gave green $Np(BH_3CH_3)_4$ in 40% yield after 6 hours; the product was identified by powder diffraction as well as ^1H and ^{11}B NMR (*vide infra*). The difference apparently was due to the fact that tetravalent neptunium is relatively stable kinetically toward reduction by $BH_3CH_3^-$. This was confirmed by running the reaction between $NpCl_4$ and $LiBH_3CH_3$ for a longer period of time. The solvent (toluene or chlorobenzene) attained a green color after a few hours but gradually changed to reddish brown if the reaction was not terminated. No $Np(BH_3CH_3)_4$ could be isolated from the brown solution. The filtered solution, after neutralization by a mineral acid, gave an absorption spectrum ascribable to Np(III) and a positive lithium flame test. No Np(IV) was found. Monomeric $M(BH_3CH_3)_3$ (M = Ln, An) cannot be isolated from solution while volatile $M(BH_3CH_3)_3 \cdot L$ exists only for the smaller lanthanides like Ho and Yb [29]. Shinomoto argued that for large cations the coordination sphere in $M(BH_3CH_3)_3 \cdot L$ was not saturated and they could not be isolated; $Sm(BH_3CH_3)_3 \cdot L$ could not be recovered in a similar way as $Ho(BH_3CH_3)_3 \cdot L$ (ionic radii for 6-coordinated Sm(III) and Ho(III) are 0.958 Å and 0.90 Å, respectively [30]). Bis-adducts of the kind $M(BH_3CH_3)_3 \cdot 2L$ are not volatile and decompose to the mono-adducts when sublimed. Following the same argument and noting that Np(III) is much larger than Ho(III) (1.01 Å for 6-coordination), one does not expect to recover $Np(BH_3CH_3)_3$ or $Np(BH_3CH_3)_3 \cdot L$ by sublimation (the brown solution turned green upon addition of diethyl ether but resulted in no sublimable product) and, consistent with the lithium flame test, the brown solution is very likely to contain the lithium salt of $Np(BH_3CH_3)_n^{[n-3]-}$, where n may range from 4 to 6; complexes such as $U(BH_4)_6^{2-}$ and $Zr(BH_4)_5^-$ have been reported [31].

The tetrachloride of plutonium exists only in the gas phase; light yellow Cs_2PuCl_6 reacted with $LiBH_3CH_3$ in chlorobenzene to give a purple solution. Again no product could be isolated by sublimation. Presence of Pu(III) was established by its absorption spectrum; lithium flame test was inconclusive when a red to orange flame was observed. Addition of dmpe (dmpe

= 1,2-bis(dimethylphosphino)ethane) or diethyl ether to the purple solution did not result in sublimable product either. As the ionic radii of Pu(III) (1.00 Å) and Np(III) are very similar, arguments from above are equally applicable here.

Experimental and calculated reduction potentials for actinides are available; it should, however, be stressed that they are highly system dependent and so cannot be used to predict reliably whether $PaCl_5$ may be reduced to give $Pa(BH_3CH_3)_4$. Nevertheless, reduction potentials for selected couples are listed in Table 4.1 as a general guide.

Element	(V)→(IV)	(IV)→(III)
Th		−3.8
Pa	−0.05, (0.02(V)→(III))[a]	−2.0, (−1.25 (IV)→(O))[b]
U	0.38	−0.63, (−0.98)[b]
Np		0.15, (−0.23)[b]
Pu		0.97
Nb	(−0.02)[a]	
Ta	(−0.92 (V)→(II))[a]	

Values in parentheses are measured by polarography under identical experimental conditions, [a]MCl_5 in acetonitrile (Ref. 32), [b]MCl_4 in DMSO (Ref. 23); other values are either calculated or measured in a different way (Ref. 33).

TABLE 4.1 Standard Reduction Potentials for Selected Couples (All values are referenced to SHE (Standard Hydrogen Electrode) and are in Volts)

The most useful comparison appears to be the reductions of MCl_5 (M = Pa, Nb, Ta) in acetonitrile. Thus $NbCl_5$ was reduced at −0.02 V (vs. SHE) to the tetravalent state, $PaCl_5$ under identical conditions was reduced at 0.02 V (assigned to the trivalent state based on the height of the wave). Since both Nb(V) and Ta(V) are reduced to a lower oxidation state by $LiBH_4$ and $LiBH_3CH_3$, it seems almost certain that $PaCl_5$ will be reduced by $LiBH_3CH_3$.

4.3 Reaction of $LiBH_3CH_3$ with Cp_2ZrCl_2 and Cp_2TiCl_2

Similar to the tetrahydroborate anion, the methyltrihydroborate anion as a ligand supposedly can bond to metal ions via mono-, bi- and tridentate hydrogen bridges. Although there are a multitude of tetrahydroborato compounds with either bi- or tridentate bridges reported, most of the methyltrihydroborato compounds studied so far consist of only tridentate bridges, with but a few exceptions that consist of metal-center-bridging BH_3CH_3 group and only one compound that possesses a bidentate BH_3CH_3 ligation [29]. For example, the structures of $U(BH_4)_3 \cdot 2dmpe$ and $U(BH_3CH_3)_3 \cdot 2dmpe$ have both been determined to be pseudo pentagonal-bipyramidal; both have tridentate axial BH_4 (or BH_3CH_3) groups, but the equatorial BH_3CH_3 group in $U(BH_3CH_3)_3 \cdot 2dmpe$ [29] is tridentate instead of being bidentate as the equatorial BH_4 group in $U(BH_4)_3 \cdot 2dmpe$ [34]. While it is expected that bonding will be such that the coordination sphere around the metal ion is satisfied, there does not seem to be a simple rule useful in predicting the ligation modes of these ligands. *Ab initio* calculation [35] and MO studies [36] have shown that there is indeed little difference in ligand-orbital energies, metal ligand overlap (while M–B overlap increases going from a bidentate to tridentate structure, the $M–H_{bridge}$ overlap decreases) and symmetry requirement between the bi- and tridentate modes. The only instance where bidentate BH_3CH_3 occurs is $U(BH_3CH_3)_4 \cdot tmed$ (tmed = tetramethylethylenediammine) which has three tridentate and one bidentate bridges. An explanation based on steric crowding alone cannot be applied here as the coordination sphere of $U(BH_3CH_3)_4 \cdot dmpe$ is found to be even more crowded than $U(BH_3CH_3)_4 \cdot tmed$ based on a cone angle argument but only tridentate bridges are present in $U(BH_3CH_3)_4 \cdot dmpe$ [29]. It is therefore of interest, in addition to studying its reducing properties, to see if $BH_3CH_3^-$ exhibits an unexpected bonding mode.

The compound $Cp_2Zr(BH_4)_2$ has been isolated from the reaction of Cp_2ZrCl_2 with $LiBH_4$ and found to consist of only bidentate bridges by IR spectroscopy [37, 38]. Reaction of Cp_2ZrCl_2 with $LiBH_3CH_3$, however, did not yield the expected $Cp_2Zr(BH_3CH_3)_2$. The monomeric hydride, $Cp_2Zr(H)BH_3CH_3$, was isolated instead by sublimation. The mass spectrum of the hydride did not show a parent ion; its identity was established by NMR and IR —— the hydride resonance was found at 4.16 ppm and the Zr–hydride stretch at 1,595 cm^{-1}.

The deuterated analogue, prepared by the reaction of Cp_2ZrCl_2 with $LiBD_3CH_3$ (which in turn was prepared by reacting $LiAlD_4$ with $B(CH_3)_3$), gave the expected NMR spectrum with marked decreases in intensities of the hydride and BH_3 peaks. The Zr–D stretch was found at 1,150 cm^{-1} (ν(M–H)/ ν(M–D) = 1.387). The Zr–H stretch compares well with those found in $Cp_2Zr(H)BH_4$ (1,620 cm^{-1}) [38] and $(\eta^5\text{-}C_5Me_5)_2ZrH_2$ (1,555 cm^{-1}) [39].

The rest of the IR spectrum shows a great similarity to that of $Cp_2Zr(H)BH_4$, especially in the B–H_{bridge} stretch region, suggesting that the BH_3CH_3 group is bidentate. The ^1H and ^{11}B NMR spectra (*vide infra*), on the other hand, clearly indicate that the three hydrogen atoms bonded to the boron atom are equivalent in solution and remain so down to a temperature of –60° C; fluxional behavior of BH_4^- in solution is well-known. No coupling between the hydride and the methyltrihydroborate protons could be observed. The bidentate ligation in the solid state was confirmed by an x-ray crystal structure determination.

The crystal is orthorhombic and belongs to the space group $Cmc2_1$ with Z = 4, the cell dimensions being a = 13.775 (3) Å, b = 9.520 (3) Å and c = 8.816 (2) Å. Selected distances and angles are given in Table 4.2. The zirconium atom is at the center of a distorted tetrahedron

Zr–H$^-$	1.79(4)	Zr–C(6)	2.461(3)
Zr–H(1)	2.04(4)	Zr–B	2.558(4)
Zr–H(2)	2.00(3)	B–C(1)	1.585(8)
Zr–C(2)	2.481(2)	B–H(1)	1.19(4)
Zr–C(3)	2.495(2)	B–H(2)	1.24(4)
Zr–C(4)	2.493(2)	B–H(3)	1.32(10)
Zr–C(5)	2.464(2)	Cp–Zr	2.177
H$^-$–Zr–B	98.6(14)	B–Zr–Cp	102.6
Zr–B–C(1)	130.4(4)	B–Zr–Cp′	116.9
H$^-$–Zr–Cp[a]	95.7	Cp–Zr–Cp′	137.1

[a] Cp represents the center of the Cp ring C(2) – C(6); Cp′ represents the equivalent group at $-x, y, z$.

TABLE 4.2 Selected Distances (Å) and Angles (degree) of $Cp_2Zr(H)BH_3CH_3$

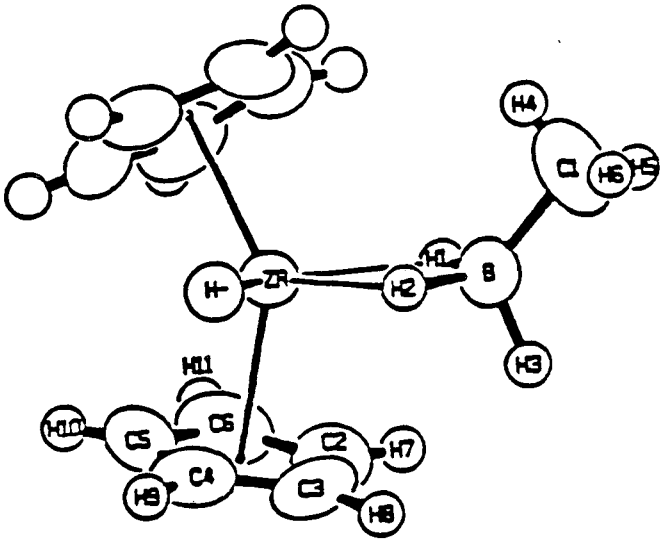

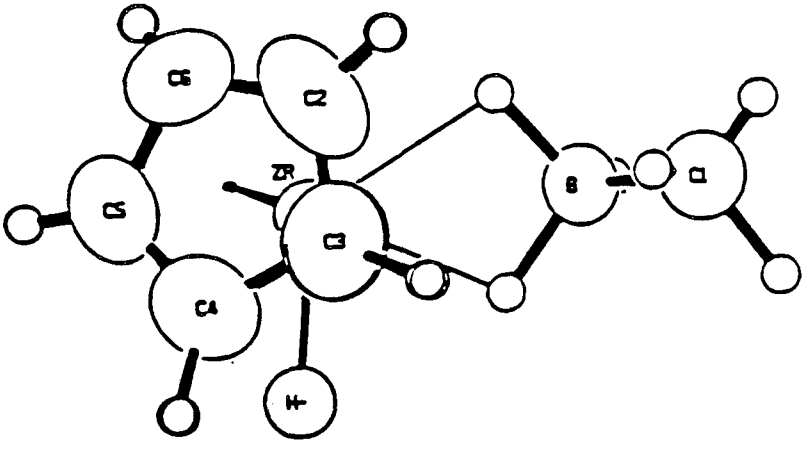

FIGURE 4.2 ORTEP drawings of $Cp_2Zr(H)BH_3CH_3$. Only one conformation of the disordered methyltrihydroborate group is shown (top), molecule more or less edge on to the rings when viewed down the *a* axis (bottom).

consisting of the centers of the two Cp rings, the hydride ion and the boron atom (See Fig 4.2). The zirconium atom is bridge-bonded to the boron atom via two hydrogen atoms; both the Zr–B–C angle of 130.4° and the Zr–B distance of 2.558 Å are indicative of a bidentate ligation. The Zr–B distance in $Zr(BH_3CH_3)_4$ with tridentate $BH_3CH_3^-$ groups is 2.335 Å [29]. It has been proposed that BH_4^- can be treated as an ionic ligand and assigned an ionic radius —— 1.6 ± 0.1 Å for a bidentate ligand and 1.36 ± 0.06 Å for a tridentate one [40]. The difference of the Zr–B distances found in $Cp_2Zr(H)BH_3CH_3$ and $Zr(BH_3CH_3)_4$ (0.223 Å, or 0.31 Å after correcting for the difference in coordination numbers) appears to be consistent with those radii, suggesting that $BH_3CH_3^-$ can similarly be treated as an ionic ligand. The zirconium atom and the hydride ion are in special positions on a mirror plane across which the Cp rings are located, the rings are in a rigorously eclipsed configuration when viewed down the *a* axis. The BH_3CH_3 group is disordered across the mirror plane and is randomly located on one side of the plane or the other with the boron atom displaced slightly away from the plane.

The inability to isolate $Cp_2Zr(BH_3CH_3)_2$ is somewhat surprising. The tetrahydroborato analogue can be prepared with relative ease from Cp_2ZrCl_2 and $LiBH_4$; $Cp_2Zr(H)BH_4$ (and polymeric Cp_2ZrH_2) is only obtained as the product of a bridge-cleavage reaction of $Cp_2Zr(BH_4)_2$ with $(CH_3)_3N$ (Equation 4.1) [37].

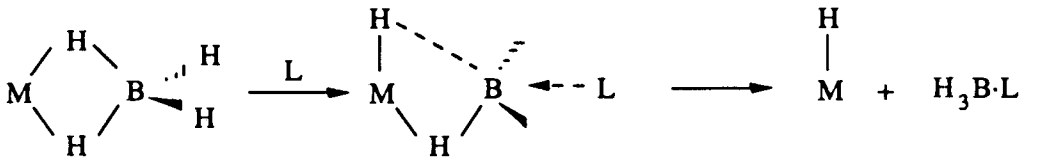

(4.1)

One would expect $Cp_2Zr(BH_3CH_3)_2$ to be more stable than $Cp_2Zr(BH_4)_2$ since the boron atom is now partially shielded by the methyl group. Yet, even in the absence of a Lewis base, only $Cp_2Zr(H)BH_3CH_3$ can be isolated. The hydride does not result from the thermal decomposition of $Cp_2Zr(BH_3CH_3)_2$ during sublimation since similar NMR and IR spectra were obtained before and after sublimation. Moreover, the same hydride results from the reaction of $Zr(BH_3CH_3)_4$

with two equivalents of CpNa. In contrast, both $Cp_2U(BH_3CH_3)_2$ and $Cp_2U(BH_4)_2$ have been prepared and found to contain only tridentate BH_3CH_3 and BH_4 groups, respectively. Similar to the case of $U(BH_3CH_3)_4 \cdot$tmed, steric crowding around the metal ion does not seem to be important here since the average Zr–C and the Zr–ring centroid distances are both shorter than those found in comparable compounds such as Cp_2ZrF_2 and Cp_2ZrCl_2 [41] and the zirconium-hydride distance of 1.79 Å agrees well with the few other Zr–H bond lengths known (1.78 and 1.81 Å in $(\eta^5\text{-}C_5Me_5)Zr(\eta^8\text{-}C_8H_8)H$ [42] and 1.78 Å in $\{ZrH(\mu\text{-}H)(\eta^5\text{-}C_5H_4Me)_2\}_2$ [43]). One can certainly pursue the argument that secondary crowding is responsible for the non-existence of $Cp_2Zr(BH_3CH_3)_2$ and the bidentate BH_3CH_3 ligation in $Cp_2Zr(H)BH_3CH_3$; however, no data exist for a suitable comparison. Furthermore, the detail of the mechanism is not known, although the source of the hydride ion is found to be from the hydroborato hydrogen.

In addition, no $Cp_2U(H)BH_3CH_3$ could be isolated by reacting Cp_2UCl_2 with $LiBH_3CH_3$, only $Cp_2U(BH_3CH_3)_2$, which was previously isolated from the reaction of $U(BH_3CH_3)_4$ with Cp^-, was recovered.

Another group IV B element whose tetrahydroborato complexes that have received extensive studies is titanium. Unlike zirconium and hafnium, and not unexpectedly, no tetravalent tetrahydroborate of titanium is known since all Ti(IV) starting materials are invariably reduced by BH_4^- and even diborane. The 9-coordinated $Ti(BH_4)_3$ does not have a saturated coordination sphere and can only be obtained from a gas-solid reaction between $TiBr_4$ and $LiBH_4$ [44]. In the presence of a weak coordinating solvent L, reaction of TiX_4 (X = halides and alkoxide) with $LiBH_4$ or diborane yields $Ti(BH_4)_3 \cdot nL$ (n = 1,2) [45]; but when non-coordinating solvents were used, an intractable blue-black solid with no definite stoichiometry resulted [46], an observation similar to those described for the reaction between niobium and tantalum halides with $LiBH_3CH_3$ in Section 4.2. However, the monomeric Cp_2TiBH_4 can be isolated from both coordinating and non-coordinating solvents [47]. It is obvious that, in terms of steric requirement, the 3-coordination of a tridentate BH_4 group cannot be equated to the formal 3-coordination of a Cp ligand. Saturating the metal coordination sphere with bulky ligands is also thought to play an important role in kinetically stabilizing the tetrahydroborate; any reaction that requires expansion of the coordination sphere such as (4.1) is hindered.

Furthermore, soft electron-donating ligands reduce the oxidizing power of the metal ion. Such generalizations are consistent with the fact that Cp_2NbBH_4 is known but not, say, $Nb(BH_4)_3$.

Reaction of Cp_2TiCl_2 with $LiBH_3CH_3$ in either chlorobenzene or diethyl ether, followed by sublimation, afforded violet needle-shaped crystals of $Cp_2TiBH_3CH_3$. The trivalent state was established by EPR and magnetic susceptibility measurements. The measured susceptibility (Fig 4.3) is typical of a d^1 system with no low-lying excited state; it exhibited Curie-Weiss behavior from 5 to 300 K with $\theta = -0.43$ K, C = 0.396 emu K/mole and an effective moment of $1.779 \pm 0.003\ \mu_B$. The room temperature solution EPR (MCH) consists of a sharp peak (5G) with $g = 1.981$ which, upon cooling to 2 K, resolved into $g_{\parallel} = 1.960$ and $g_{\perp} = 1.9902$ and is the same as the spectrum obtained with the powder at room temperature. This is in good agreement with the g-value of 1.982 found for Cp_2TiBH_4 in solution [48]. By single crystal and powder diffraction, the cell dimensions have also been determined; the crystal is orthorhombic and belongs to the space group of $Fmm2$ with $a = 13.192(5)$ Å, $b = 9.330(2)$ Å and $c = 8.931(3)$ Å. The molecular structure was not solved. The ligation mode of the BH_3CH_3 group was determined by IR spectroscopy instead (Fig 4.4). The figure also includes the spectra of $Cp_2Zr(H)BH_3CH_3$, $Cp_2U(BH_3CH_3)_2$ and $Cp_2LuBH_3CH_3$ in the same region; the BH_3CH_3 groups in $Cp_2U(BH_3CH_3)_2$ and Cp_2LuBH_3CH are tridentate [29]. These spectra unambiguously identify the BH_3CH_3 group in $Cp_2TiBH_3CH_3$ to be doubly bridging; the BH_4 group in Cp_2TiBH_4 is also found to be doubly bridging by x-ray crystallography [49]. The rest of the IR spectrum also shows a great resemblance to that of $Cp_2Zr(H)BH_3CH_3$ with the exception of the missing Zr–H stretch.

It is therefore seen that the bidentate bonding mode in methyltrihydroborates is apparently more common than originally believed. However, as with the tetrahydroborates, consistent prediction of the ligation does not seem straightforward. While $Cp_2TiBH_3CH_3$ behaves very much like Cp_2TiBH_4, reaction of Cp_2ZrCl_2 with $LiBH_3CH_3$ yielded the unexpected product of $Cp_2Zr(H)BH_3CH_3$ instead of $Cp_2Zr(BH_3CH_3)_2$.

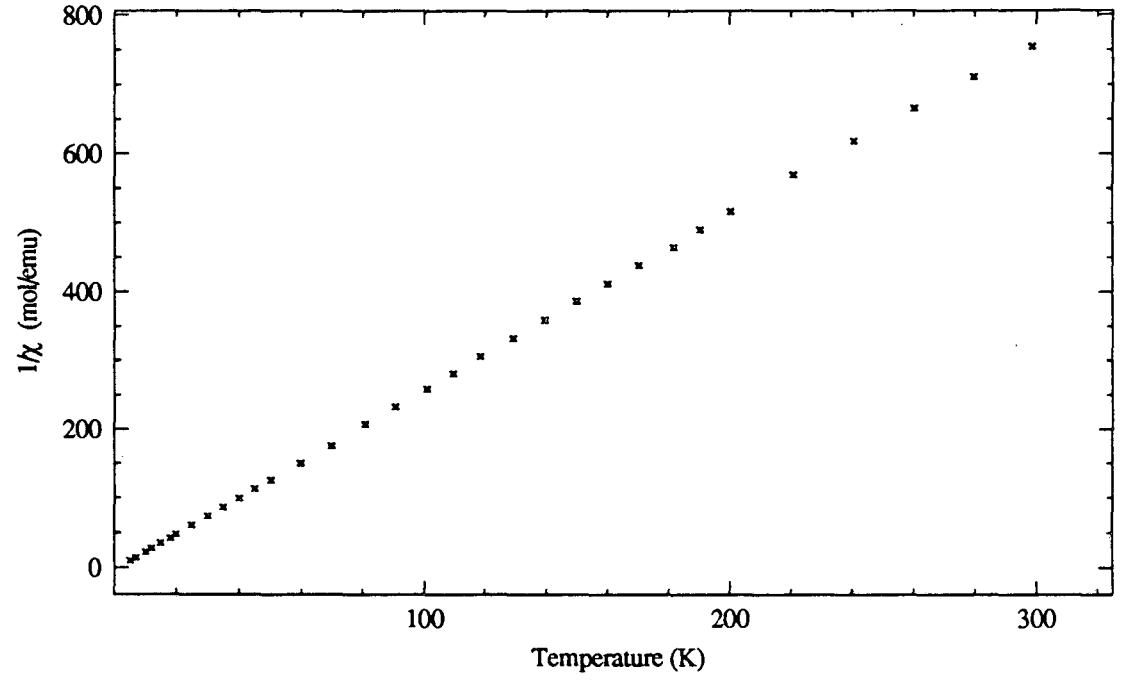

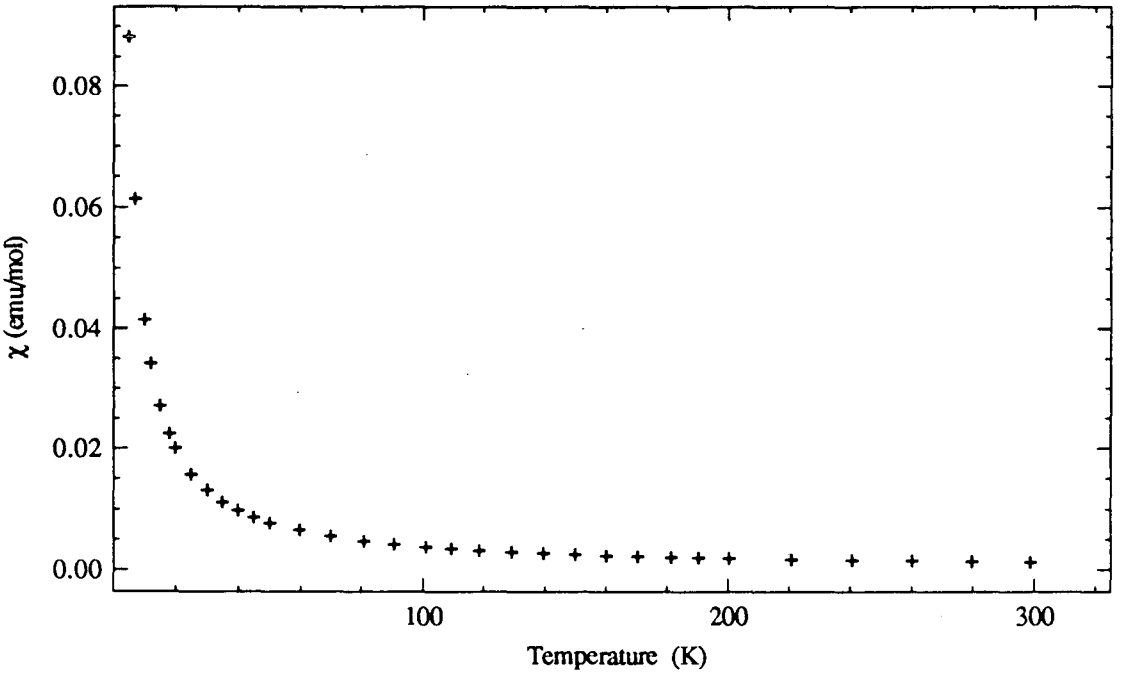

FIGURE 4.3 Measured magnetic susceptibility of $Cp_2TiBH_3CH_3$, (top) $1/\chi$ vs. temperature and (bottom) χ vs. temperature.

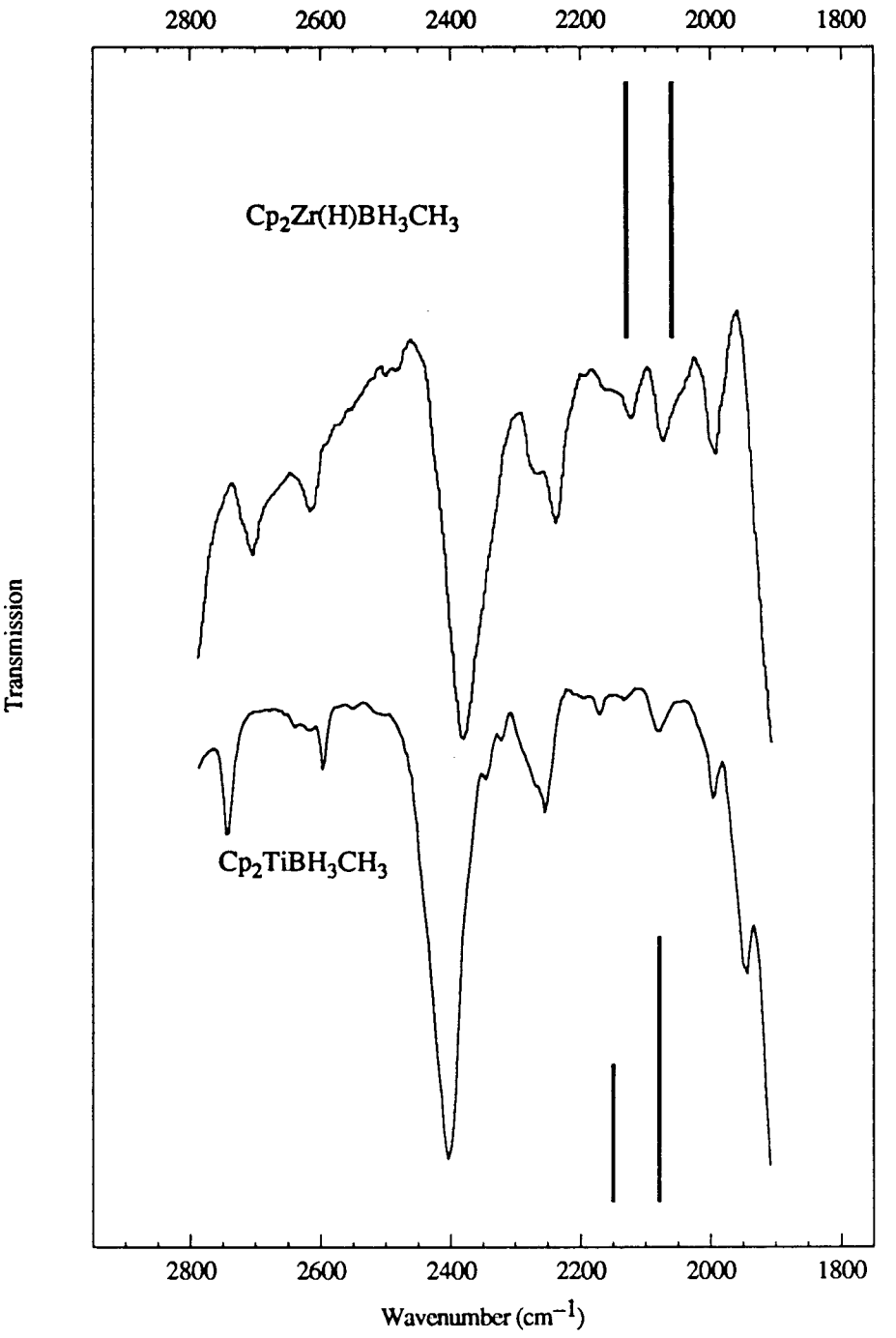

FIGURE 4.4 IR spectra of $Cp_2TiBH_3CH_3$ in toluene (bottom) and $Cp_2Zr(H)BH_3CH_3$ (top) in the BH stretching region. Absorption peaks found in $Cp_2U(BH_3CH_3)_2$ (bottom) and (top) $Cp_2LuBH_3CH_3$ are shown as sticks.

4.4 Syntheses of Protactinium Chlorides

The binary halides of Pa(IV) and Pa(V) are all well-established; all are moisture-sensitive and with the exception of the fluorides, all are oxygen-sensitive. Consequently, their preparations and handling require dry and anaerobic conditions, especially when only milligram amounts are involved. Convenient, high-yield synthetic routes to these halides are of critical importance to any synthesis that requires them as starting materials. Over the course of this study, $PaCl_4$, $PaCl_5$ and hexachloroprotactinates have been prepared with a variety of methods and this section serves as a summary of these preparations.

4.4.1 Preparation of Pa^{4+}:Cs_2ZrCl_6 and its Reaction with $LiBH_3CH_3$

As shown earlier, chloro complexes of the kind $M'MCl_6$ and M'_2MCl_6 (M'= Cs, $(CH_3)_4N$, $(C_2H_5)_4N$ and M = U and tetravalent Zr) are all useful starting materials for the syntheses of $M(BH_3CH_3)_4$. The complexes $CsPaCl_6$ and Cs_2PaCl_6 are both known and $CsPaCl_6$ can easily be precipitated from a thionyl chloride solution containing the Pa cation; it has the further advantage of being stable to oxygen. Axe has also shown that $PaCl_6^{2-}$ can be formed by melting Cs_2ZrCl_6 with $PaCl_4$ or PaO_2 ; the crystal thus obtained, Pa^{4+}:Cs_2ZrCl_6, was used in the first detailed electronic study of Pa^{4+} in the solid state [50]. In the first attempt at preparing $Pa(BH_3CH_3)_4$, it was decided that Pa^{5+}:Cs_2ZrCl_6 would make a convenient starting material. It has the advantage of minimizing the amount of Pa ($\leq$ 1 mg) to be handled while maintaining all operations in a 'macro' scale; a technique equivalent to the use of carriers in radiochemistry. The resulting material, presumably $Pa(BH_3CH_3)_4$ diluted in $Zr(BH_3CH_3)_4$, can be studied by EPR with relative ease.

Single crystals of Cs_2ZrCl_6 could be obtained by melting a mixture of dry CsCl and $ZrCl_4$ in the correct stoichiometry at 860° C and then slowly cooling the melt; the evacuated quartz ampoule passed through the furnace at a rate of 1–2 mm/hr. Dry Pa_2O_5 ($\approx$ 1 mg) was added to a 2 g crystal of Cs_2ZrCl_6 which was then regrown, resulting in a bright yellow crystal. Fluorescence, ERS (electronic Raman scattering) and EPR (see Fig 4.5) spectroscopies have

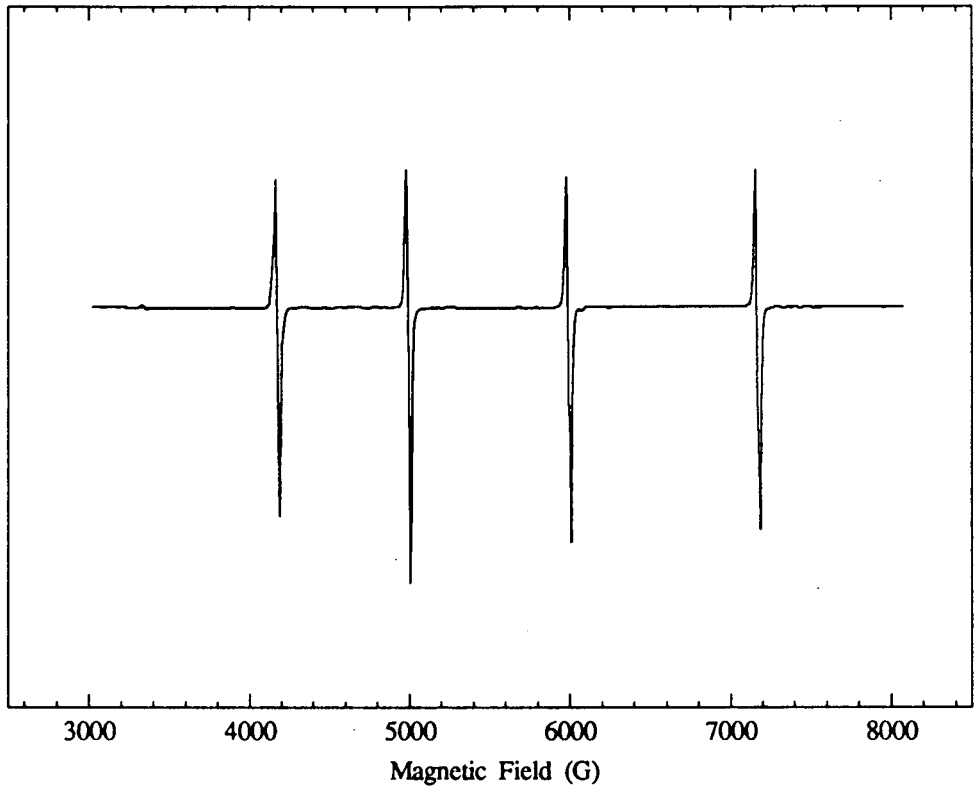

FIGURE 4.5 EPR spectrum of Pa^{4+}:$CsZrCl_6$ at 20 K (I = 3/2 for ^{231}Pa). Microwave frequency = 9.225 GHz. This spectrum is identical to the one obtained with $PaCl_4$ doped in Cs_2ZrCl_6 [50].

shown that $PaCl_6^{2-}$ was present [51]. The extent and mechanism of the Pa(V)→Pa(IV) reduction are not known, although intense β radiation has been observed as a source of reductant [52]. Both Pa^{4+}:Cs_2ZrCl_6 and Pa^{5+}:Cs_2ZrCl_6, however, are expected to yield $Pa(BH_3CH_3)_4$. In addition, this crystal, unlike $PaCl_4$, is relatively stable in open atmosphere and can be so handled for minutes without appreciable change. The crystal was pulverized and then reacted with excess $LiBH_3CH_3$ in chlorobenzene which acquired a pale yellow color after ≈ 10 hours. After 2 days of reaction, slow sublimation at 50° C afforded crystals of $Zr(BH_3CH_3)_4$ in relatively good yield (40 %). *No* EPR was observed with the crystals at room or cryogenic temperature. By γ-counting, it was found that only less than 1% of the starting protactinium

was present in the final product. The basic principle behind carrier chemistry depends on the fact that both the radionuclide and the carrier have similar chemical and physical properties, an assumption that has not been proven in the present case for $Zr(BH_3CH_3)_4$ and $Pa(BH_3CH_3)_4$ (*vide infra*). As $Pa(BH_3CH_3)_4$ could not be isolated in reasonable yield, other synthetic routes were examined.

4.4.2 Syntheses of $PaCl_5$ and $PaCl_4$

All of the published syntheses of $PaCl_5$ involve chlorination of Pa_2O_5 with various reagents, but most of them suffer from low yield. The most satisfactory procedure is the chlorination with $SOCl_2$ in a sealed tube; $PaCl_5$ can be isolated in 90% yield [53]. When this was attempted, however, the yield was inconsistent and generally low, apparently because the $SOCl_2$ vapor did not come into good contact with the oxide. Modification of the procedure by periodically admitting fresh $SOCl_2$ vapor into the reaction vessel only slightly improved the yield and was extremely tedious. The following modification was found to work well. A pyrex reaction vessel is depicted in Fig 4.6. In a typical reaction, one sidearm was filled with 0.5 ml of $SOCl_2$. Freshly precipitated protactinium (V) hydroxide (≈ 25 mg) was dried in air at 250° C and then loaded into the vessel between the sidearms. After the $SOCl_2$ was degassed by several cycles of 'freeze-thaw', the reaction tube was sealed off. The empty sidearm was cooled to –20° C before the oxide was heated to 400° C. Pale yellow needle-shaped crystals of $PaCl_5$ began to deposit on the cooler zones on both sides of the furnace within minutes. A good continuous flow of $SOCl_2$ vapor over the hydroxide was maintained by alternately cooling the two sidearms. The reaction was found to be complete within an hour after which the excess $SOCl_2$ was condensed into a sidearm which was then sealed off. The identity of $PaCl_5$ was confirmed by x-ray powder diffraction. It is noted that although $PaCl_5$ appeared to be stable indefinitely when stored under an inert atmosphere, invariably a small amount of decomposition was observed to occur when a stored sample was purified by sublimation —— a gray powder that did not sublime was left behind. The decomposition probably was a result of radiation damage since it appeared to be a function of time and always happened regardless of how much care

was taken in drying and degassing the glassware. Subsequently, $PaCl_5$ was prepared just before use and was kept for no more than 24 hours.

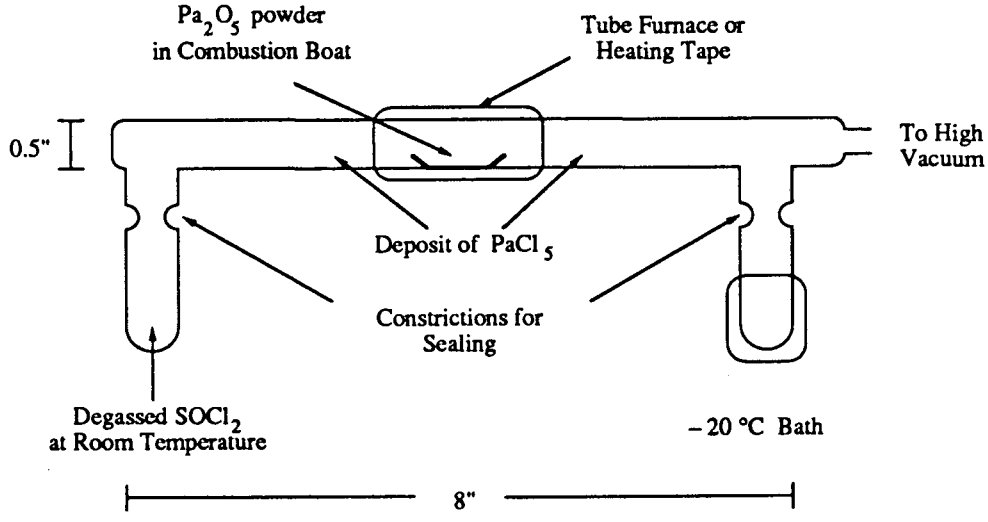

FIGURE 4.6 Reaction vessel for synthesis of $PaCl_5$. Similar design of quartz vessel for synthesis of larger quantities of $NpCl_4$ has larger dimensions.

Preparation of $PaCl_5$ is known to result in radiochemical purity; γ-spectra of the Pa stock solution, $PaCl_5$ synthesis product and residue are shown in Figure 4.7. High-energy β- and γ-radiation due to decay daughters build up rapidly in ^{231}Pa; the stock solution used in this study has not been purified radiochemically for years and was difficult to handle because of the intense radiation. However, over 80% of the β- and γ-activities was eliminated after separation of $PaCl_5$, making its manipulation much easier. Moreover, as seen from the absence in the synthesis residue of the 27.4 keV gamma ray, characteristic of ^{231}Pa, the yield of $PaCl_5$ is practically quantitative. Substitution of CCl_4 for $SOCl_2$ was found not to work as satisfactorily.

The same technique has been extended to the syntheses of $NpCl_4$ and $PuCl_3$ from NpO_2 and plutonium (IV) oxalate, respectively. In the case of $NpCl_4$, the reaction temperature required is 550° C and so quartz has to be substituted for pyrex and the yield is also 100%. Up to 2 g of $NpCl_4$ could be isolated within 2 hours. The procedure, however, is not recommended for preparing $PuCl_3$ since it sublimes only at a temperature of >800° C and although some $PuCl_3$ was seen to form at a reaction temperature of 880° C, the reaction was far from complete, probably because of the decomposition of $SOCl_2$ at such a high temperature.

In addition to achieving radiochemical purity, it was found that the procedure described above could be used to purify the Pa chemically up to a certain extent. Equal parts (by weight) of Pa and impurities such as silicon could be used to synthesize $PaCl_5$ while the impurities remained unreacted. The same procedure unfortunately was not found to be satisfactory in recovering Pa from large amount of impurities; otherwise it would be invaluable in minimizing the loss of Pa during its recycling. Solution containing up to 50 mg of Pa collected after various synthetic reactions was evaporated to dryness and the residue was boiled with concentrated HNO_3 to destroy all organics. Addition of concentrated ammonia precipitated Pa (V) hydroxide and removed impurities that form soluble hydroxides such as Li and Al. The final mass contained ≈ 10% of Pa; impurities might include insoluble borates. The yield of $PaCl_5$ using this solid and the above procedure was ≈ 10%. The low yield was probably due to insufficient surface area for the reaction to take place.

The best method for the preparation of $PaCl_4$ was reported to be the reduction of $PaCl_5$ by Al metal or H_2 gas [54], and a small amount of $PaCl_4$ has been made by chlorination of PaO_2 [55]. Although the above procedure for preparing $NpCl_4$ is expected to work well for $PaCl_4$, Pa_2O_5 can only be reduced to give PaO_2 at the very high temperature of over 1,500° C [55]; reduction of $PaCl_5$ was attempted instead.

Reaction was observed to take place at ≈ 200° C between $PaCl_5$ (28–33 mg) and excess Al metal in an evacuated glass tube, yellowish-green $PaCl_4$ was seen to deposit on the surface of the Al metal and white crystals of $AlCl_3$ were collected at the cold end of the tube. Following published procedure [54], the temperature was then raised to ≈ 480° C in order to separate $PaCl_4$ from the reductant; however, no separation resulted and the $PaCl_4$ crystals turned

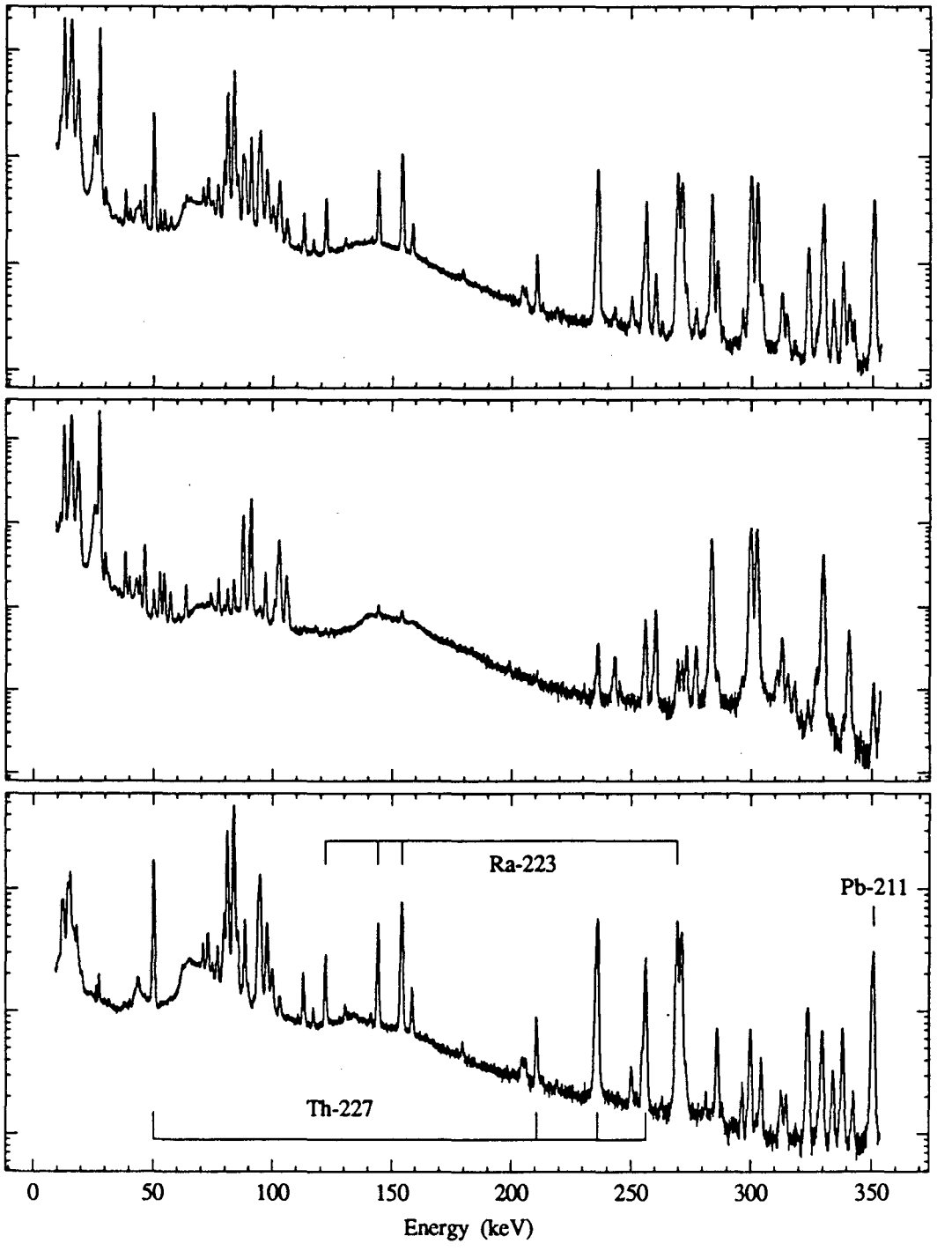

FIGURE 4.7 Gamma-spectra of (top) Pa stock solution, (center) $PaCl_5$ synthesis product and (bottom) synthesis residue from 0 to 360 keV. The residue left behind after isolation of $PaCl_5$ was not visible to the naked eye, the ceramic boat used to hold the Pa_2O_5 was counted. Some of the decay daughters are identified.

grey and acquired a metallic luster. Raising the temperature to ≈ 550° C produced no further change. Surface oxide on the Al metal was removed in the present case by amalgamation with Hg followed by washes with THF; alternatively, freshly cut slivers of high purity Al metal were polished before use. Both resulted in the same observation; one that has been reported before [22, 23]. As green $PaCl_4$ crystals were seen to form, oxide impurities that cause formation of oxychlorides cannot be the reason for the inability to isolate $PaCl_4$. Reaction between $PaCl_4$ and Al metal at elevated temperatures appears to be a more likely cause.

Reduction of $PaCl_5$ by H_2 gas at 500° C in a sealed tube only produced $PaCl_4$ in 40–60 % yield with formation of an unidentified white powder; $PaCl_4$ could be purified by sublimation at ≈ 580° C. The reason for the poor yield is not known.

4.4.3 Solubility of $PaCl_5$ in Aromatic Solvents

Similar to $NbCl_5$ and $TaCl_5$, $PaCl_5$ is soluble in various coordinating solvents; for example, it is soluble in CCl_4 and CH_3CN with the formation of adducts such as $PaCl_5 \cdot 4CH_3CN$. Most of these solvents unfortunately are not suitable for the syntheses of organometallics and Lewis-base free compounds such as $Pa(BH_3CH_3)_4$. During one attempted reaction of $PaCl_5$ with $LiBH_3CH_3$ in THF, polymerization of THF took place so quickly that a very viscous wax-like substance was formed instantaneously when $PaCl_5$ was dissolved in THF and before any reaction with $LiBH_3CH_3$ could occur. Presumably a similar reaction will happen with other ether solvents such as diethyl ether.

Being dimers consisting of two edge-sharing octahedra in the solid state, both $NbCl_5$ and $TaCl_5$ are also soluble in aromatic solvents such as toluene. While it is very likely that the solvent is coordinating using its π-electrons, the exact interaction in solution is not clearly understood. Pentachlorides of antimony and phosphorus are known to regioselectively chlorinate aromatic hydrocarbons and a π-complex intermediate is postulated for $SbCl_5$ [56]; but $NbCl_5$ and $TaCl_5$ do not undergo similar reactions. Dissolution of $NbCl_5$ and $TaCl_5$ in benzene and toluene occurs with no detectable heat change and the IR spectra of the mixture show the unperturbed absorption of the hydrocarbons [57], suggesting the interaction is weak.

Equilibrium studies also show that the interaction is very weak [58]; in particular, it is not even known if the pentachlorides are monomeric or dimeric in solution. The colors of the two in toluene were distinctly different than the solids, $NbCl_5$ being red orange in toluene instead of yellow in the solid state and $TaCl_5$ being pale yellow instead of white. The solvent could not be removed completely by vacuum, the resulting solids were colored like the solutions and gave positive carbon and hydrogen analyses but with no definite stoichiometry. A solution of these solids in either CCl_4 or d_{14}-methylcyclohexane showed the ^1H NMR spectrum of free toluene. Finally, single crystals different than the pure chlorides could be isolated from the solution but desolvated quickly and turned amorphous in an inert atmosphere.

In the course of reacting $PaCl_5$ with $LiBH_3CH_3$, it was found that $PaCl_5$ was soluble in chlorobenzene, toluene or benzene to give a pale yellow solution. Up to 25 mg of the chloride is soluble in 5 ml of toluene. This was unexpected considering that the interaction between these solvents and the pentachlorides of Nb and Ta is very weak and that the structure of $PaCl_5$, unlike those of dimeric $NbCl_5$,$TaCl_5$ and UCl_5, is polymeric and consists of chains of edge-sharing pentagonal bipyramids. No other chloride is known to have a similar structure. These solutions of $PaCl_5$ are stable up to weeks and show no sign of polymerization as in THF. The residual solid after removal of the solvent is soluble in methylcyclohexane and shows ^1H NMR of free toluene. Absorption spectra of $PaCl_5$, $NbCl_5$ and $TaCl_5$ in d_8-toluene are shown in Fig 4.8. The absorption edges of $NbCl_5$ and $TaCl_5$ in various aromatic solvents have been assigned as charge-transfer bands [59] and their relative positions correlated with electron affinities of the metal which were found to increase in the order Ta < Nb < V. Figure 4.8 suggests that $PaCl_5$ will show redox behavior closer to that of $TaCl_5$ than $NbCl_5$. The complex $PaCl_5 \cdot SOCl_2$ was also found to be soluble in toluene, resulting in a reddish brown solution.

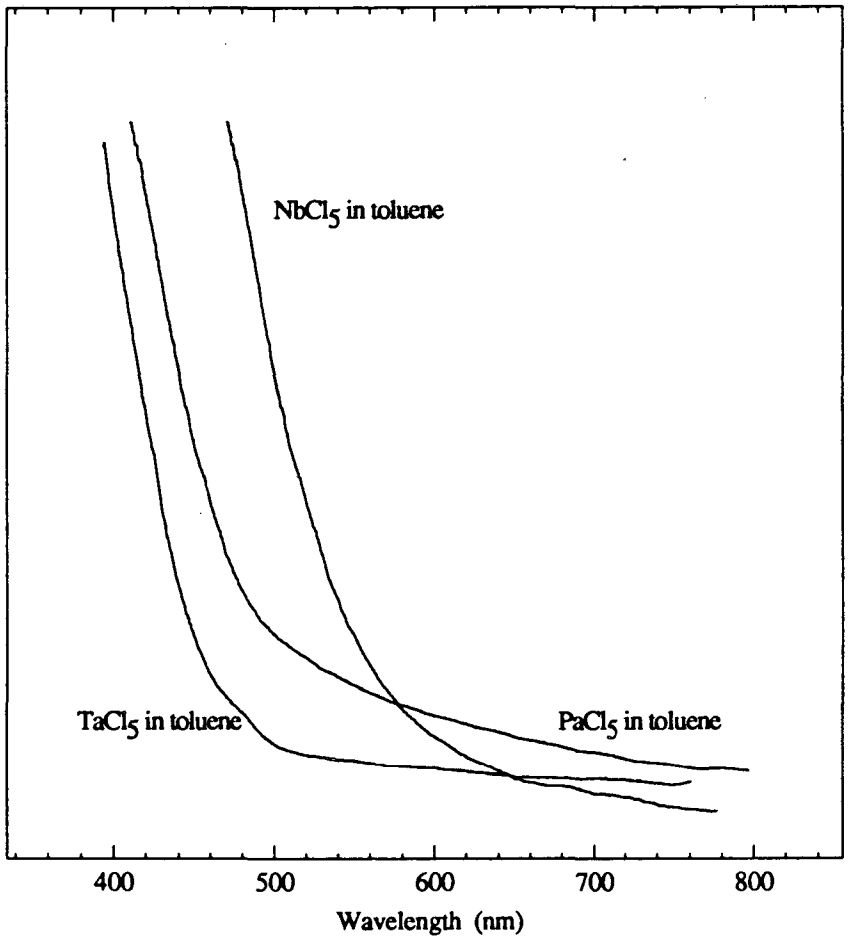

FIGURE 4.8 Absorption spectra of $PaCl_5$, $NbCl_5$ and $TaCl_5$ in d_8-toluene.

4.5 Reaction of $PaCl_5$ with $LiBH_4$ and $(CH_3C_5H_4)Na$

Although the exact interaction is not known, the solubility of $PaCl_5$ in aromatic solvents can be of value in synthesis, especially of Pa(IV) species the yield of which is generally low. Difficulties associated with making $PaCl_4$ can also be avoided. For instance, only 1.5 mg of $PaCl_4$ could be synthesized to be the starting material in the preparation of $Pa(COT)_2$ (COT = cyclooctatetraene), earlier attempts reacting $PaCl_5$ with K_2COT were

unsuccessful because of the lack of a suitable solvent (THF as a solvent was found to polymerize, similar to the observation described above) and no convenient solvent-free route existed [14]. Only a very small amount of $Pa(COT)_2$ could be isolated and, as a result, no physical or chemical studies were performed on the compound. Reaction of $PaCl_5$ with K_2COT in toluene is almost certain to produce $Pa(COT)_2$ in good yield. Use of $PaBr_5$ and PaI_5 is also expected to work well. The pentabromide is isostructural to $NbCl_5$ and both will very likely be soluble in aromatic solvents. However, syntheses of $PaBr_5$ and PaI_5 do not seem to work as satisfactorily as that described for $PaCl_5$; for instance, $PaOBr_3$ invariably results as a byproduct in the preparation of $PaBr_5$ [60].

Polymeric $Pa(BH_4)_4$ was prepared in very low yield (< 10%) by treating PaF_4 with the liquid $Al(BH_4)_3$ and the reaction took days [28]. In contrast, freshly prepared $PaCl_5$ (31 mg), dissolved in d_8-toluene, showed a reaction with excess $LiBH_4$ (15 mg) in minutes when the color of the solution turned from pale yellow to orange. By sublimation at 45° C, orange $Pa(BH_4)_4$ could be isolated in ≈ 45% yield (by γ-counting). The product was identified by x-ray powder diffraction. It should be noted that the yield was probably depleted by formation of $Pa(BH_4)_n^{[n-4]-}$ (n = 5, 6) as in another attempt of the reaction, the orange color returned to yellow upon prolonged stirring and no product could be isolated by sublimation (*c.f.* reaction of $NpCl_4$ and Cs_2PuCl_6 with $LiBH_3CH_3$ in Section 4.2).

Other than $Pa(COT)_2$ [14] and $Pa(TMCOT)_2$ (TMCOT = tetramethylcyclooctatetraene) [15], the only organometallic compound of Pa ever reported is Cp_4Pa [13] (Cp_3PaCl was mentioned but no detail was given [61]). It was obtained from the solvent-free reaction between $PaCl_5$ and Cp_2Be at 65° C with a yield of 54% and characterized by IR and MS. In the present case, $PaCl_5$ (28 mg) in d_8-toluene was used to react with excess MeCpNa (32 mg) [62]. The solution turned orange almost instantaneously and was filtered after 2 h of stirring. An NMR spectrum of the solution is shown in Figure 4.9; a plot of the chemical shifts versus 1/T is shown in Figure 4.10. Removal of solvent resulted in a yellowish orange powder. The yield of $(MeCp)_4Pa$ is over 80% by γ-counting. Attempts were made to detect EPR of the powder and its solution in MCH but were unsuccessful from 4 – 300 K. No signal could be detected either with a powder that resulted from evaporation of a solution that contained $(MeCp)_4Pa$ and $(MeCp)_4Th$ (Pa/Th ≈ 5%). These spectroscopic results will be discussed in a later section.

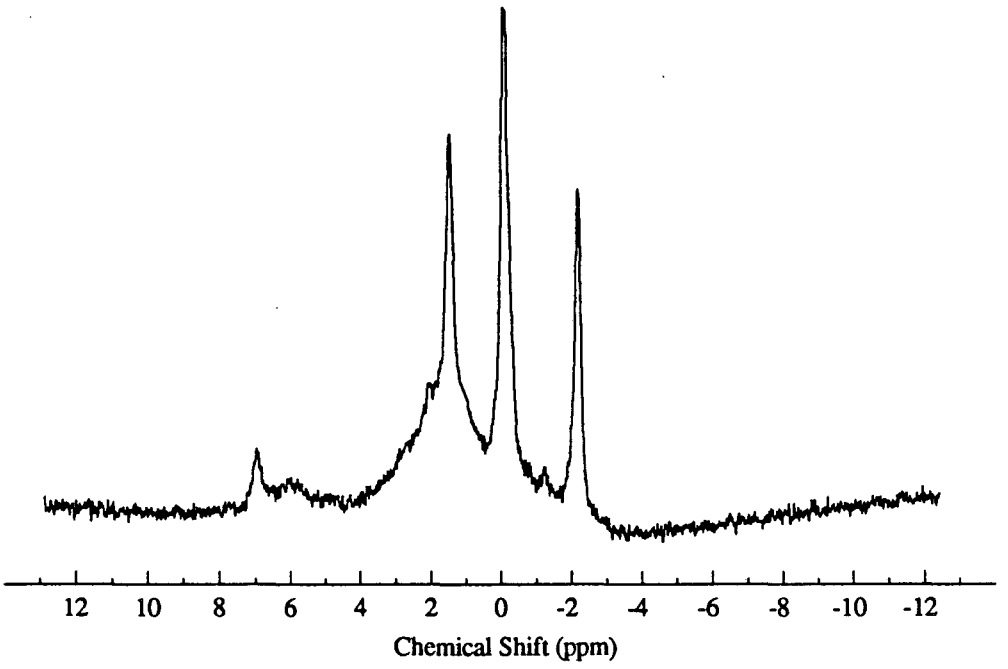

FIGURE 4.9 ^{1}H NMR of $(MeCp)_4Pa$ in d_8-toluene at room temperature. The methyl proton is at –0.03 ppm and the ring protons are at 1.47 and –2.16 ppm.

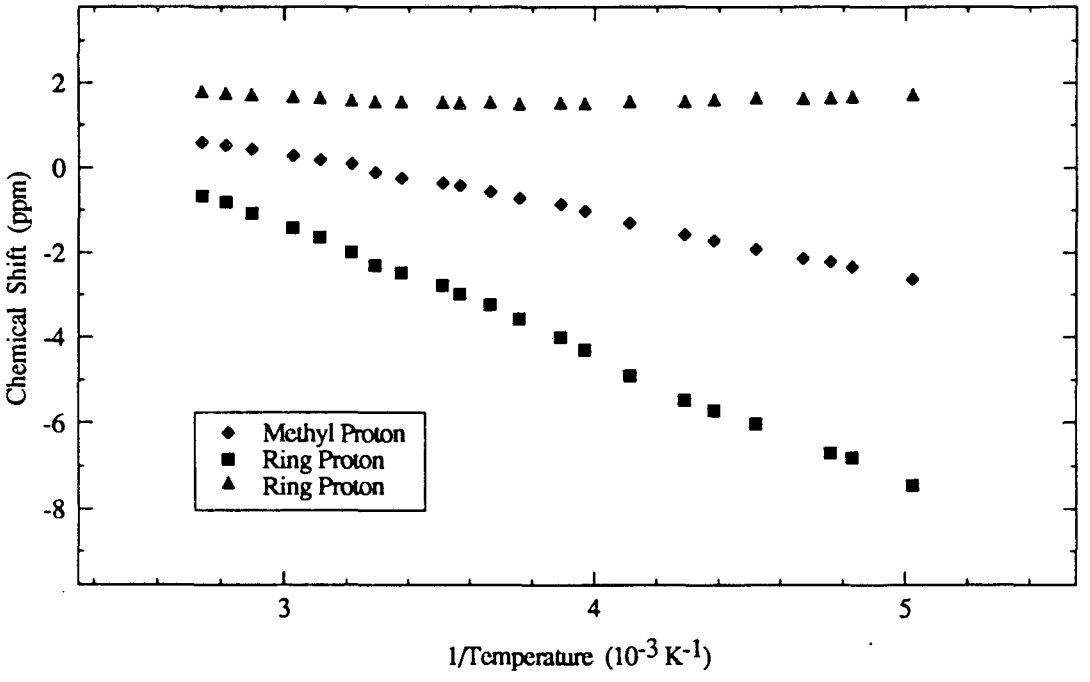

FIGURE 4.10 Variable temperature ^{1}H NMR data of $(MeCp)_4Pa$ in d_8-toluene.

It is therefore seen that while Pa(IV) is known to be quite unstable toward oxidation to Pa(V), a variety of procedures have resulted in the Pa(V)→Pa(IV) reduction —— melting Cs_2ZrCl_6 together with Pa_2O_5 gave $PaCl_6^{2-}$, both BH_4^- and $MeCp^-$ reduced $PaCl_5$ in toluene to give the corresponding tetravalent compounds respectively in relatively good yield.

4.6 Reaction of Protactinium Chlorides with $LiBH_3CH_3$

A pale yellow solution of $PaCl_5$ (22 – 37 mg) in either chlorobenzene or toluene was mixed with excess $LiBH_3CH_3$ and the color immediately turned green. It gradually returned to yellow and the reaction was stopped after ≈ 3 h to avoid the possible formation of anionic complex such as $Pa(BH_3CH_3)_5^-$. The solvent was then removed under vacuum. The remaining residue was sublimed at room temperature and a pale yellow crystalline solid was collected on a 0° C cold finger. The average yield was ≈ 50% by γ-counting. The solid is extremely volatile as no extra sublimable product was observed after ≈ 30 minutes even at room temperature and under a static vacuum of 50 mTorr. It was found that when chlorobenzene was used (b. p. = 132° C), part of the yellow sublimate was removed together with the solvent and so lower-boiling toluene (or benzene) was substituted in subsequent attempts. By placing the sublimate in one end of an evacuated glass tube and shinning a light on it, large needle-shaped single crystals could be obtained at the other end of the glass tube after ≈ 3 days. The pale yellow crystals darkened and became dark brown after ≈ 2 weeks, presumably due to radiation damage, but could be restored to pale yellow by regrowing. These crystals appeared to be suitable for x-ray structure determination but it was not attempted because of the high radioactivity. A partial x-ray powder pattern is shown in Table 4.3. No attempt was made to index these lines because i) several more lines than listed were recorded but were too weak for an accurate determination of their positions and ii) no two of the known monomeric $An(BH_3CH_3)_4$ (An = Th, U, Np) are isomorphic and the volatility of the product appears to be much higher than those of $Th(BH_3CH_3)_4$ and $U(BH_3CH_3)_4$, suggesting that it possesses a different crystal structure. This is unfortunate because many of the standard characterization techniques are not practicable with compounds of protactinium and powder diffraction has been

$\sin^2\theta$	Intensity	d (Å)
0.00671	w,broad	9.4110
0.00927	M,broad	8.0068
0.01466	w,broad	6.3669
0.02327	M	5.0535
0.02639	S	4.7454
0.03479	w	4.1331
0.04565	w	3.6081

TABLE 4.3 Partial Powder Pattern of Reaction Product of $PaCl_5 + LiBH_3CH_3$

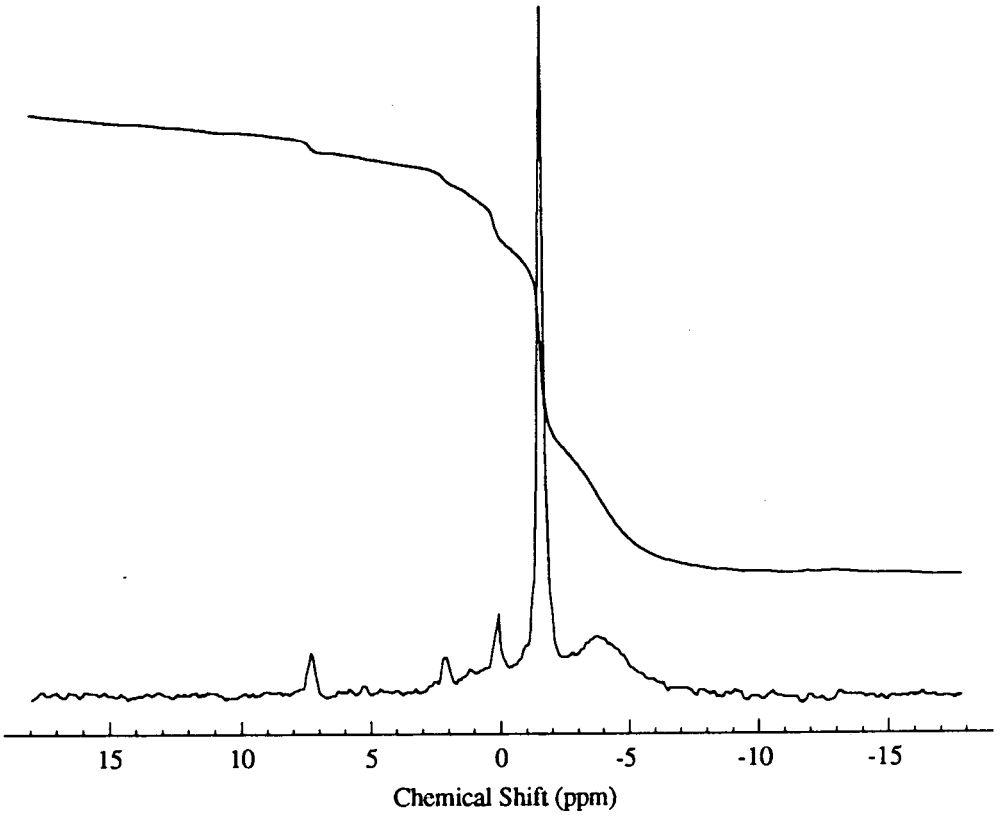

FIGURE 4.11 ^1H NMR spectrum of the reaction product of $PaCl_5$ with $LiBH_3CH_3$ in d_8-toluene at room temperature.

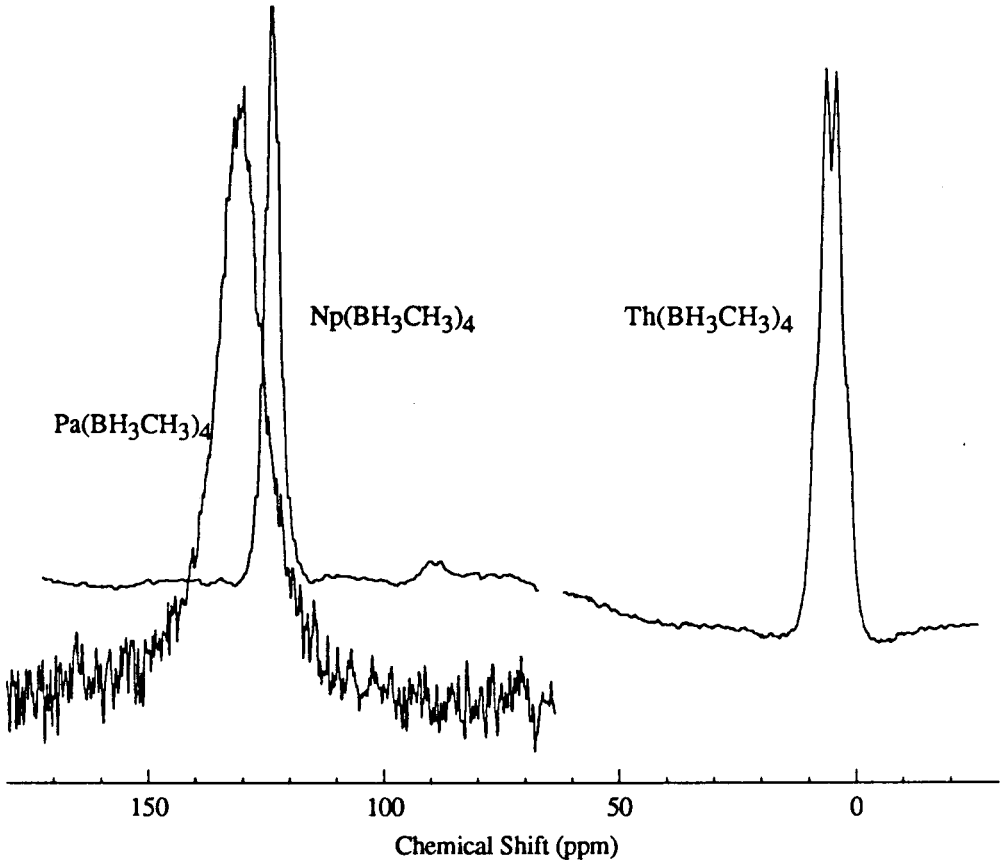

FIGURE 4.12 ^{11}B NMR spectrum of the reaction product of $PaCl_5$ with $LiBH_3CH_3$ at room temperature. Those of $Np(BH_3CH_3)_4$ and $Th(BH_3CH_3)_4$ are included for comparison. Referenced to $BF_3{\cdot}OEt_2$. The quartet in $Th(BH_3CH_3)_4$ could be resolved.

the primary technique in characterizing them.

Figures 4.11 and 4.12 show respectively ^1H and ^{11}B NMR spectra of the product; no attempt was made to collect ^{13}C spectrum. *No* EPR could be found with the powder, the single crystals or a dilute MCH solution of the powder. The MCH solution did not show any absorption in the 5,000 – 22,000 cm^{-1} range.

The absence of an EPR signal and absorption bands, together with the relatively small ^1H chemical shifts (chemical shifts found for the bridging protons in $Np(BH_3CH_3)_4$ and $U(BH_3CH_3)_4$ are over 150 ppm, *vide infra*), cast much uncertainty over the identity of the

product, although the green color observed was reminiscent of $PaCl_4$ and its extraordinarily high volatility suggested it to be a monomeric methyltrihydroborate. In particular, the product was thought to be a pentavalent species such as $Pa(BH_3CH_3)_5$ or $PaCl_n(BH_3CH_3)_{5-n}$ since the ^1H chemical shifts observed were very close to those of diamagnetic $Th(BH_3CH_3)_4$ (0.11 ppm for CH_3 and 3.43 ppm for BH_3). However, in consideration of the results from above, it appeared highly unlikely that $LiBH_3CH_3$ cannot realize the Pa(V)→Pa(IV) reduction. Moreover, the large downfield ^{11}B chemical shift observed was similar to those found in $Np(BH_3CH_3)_4$ and $U(BH_3CH_3)_4$ (Fig 4.12). Since many of the other characterization techniques were not accessible because of the associated radioactivity (e.g. mass spectroscopy) and the small amount of material available, we turned to the reaction between $PaCl_4$ and $LiBH_3CH_3$.

As described in Section 4.4.2, $PaCl_4$ could only be isolated in 40–60% yield by hydrogen reduction of $PaCl_5$. This, together with the anticipated low yield (≈ 35%) and the small amount of Pa available, made the reaction between $PaCl_4$ and $LiBH_3CH_3$ unattractive and difficult. A total of 14 mg (0.0375 mmole) of $PaCl_4$, purified by sublimation at 580° C, was used to react with excess $LiBH_3CH_3$ (6.5 mg, 0.18 mmole) in chlorobenzene. The solution acquired a yellow color after ≈ 1 day and the reaction was stopped after 2 days. After removal of solvent, sublimation at room temperature yielded < 3 mg of a pale yellow solid. Both ^1H and ^{11}B NMR identified it to be the same product isolated from the reaction of $PaCl_5$ with $LiBH_3CH_3$. *No* EPR could be observed.

The failure to previously observe an absorption spectrum was obviously due to the low concentration of the solution used; typical $f \rightarrow f$ transitions have low intensities. A much more concentrated solution was then used to obtain an absorption spectrum and it is shown in Figure 4.13. Variable temperature ^1H (Fig 4.14) and ^{11}B NMR of the product were also recorded, showing that the reaction product is indeed paramagnetic (*vide infra*). Together they established the tetravalent state of Pa in the final product. In light of all these results, it is apparent that Pa^{4+}:$CsZrCl_6$ might also have yielded $Pa(BH_3CH_3)_4$. The considerably higher volatility of $Pa(BH_3CH_3)_4$ compared to that of $Zr(BH_3CH_3)_4$ explains why the relative yield of $Pa(BH_3CH_3)_4$ was so low; sublimation was carried out using a dynamic vacuum and at 50° C required for the separation of $Zr(BH_3CH_3)_4$ instead of at room temperature. The little amount of $Pa(BH_3CH_3)_4$ present in the matrix of $Zr(BH_3CH_3)_4$ was also EPR silent. It is not known if

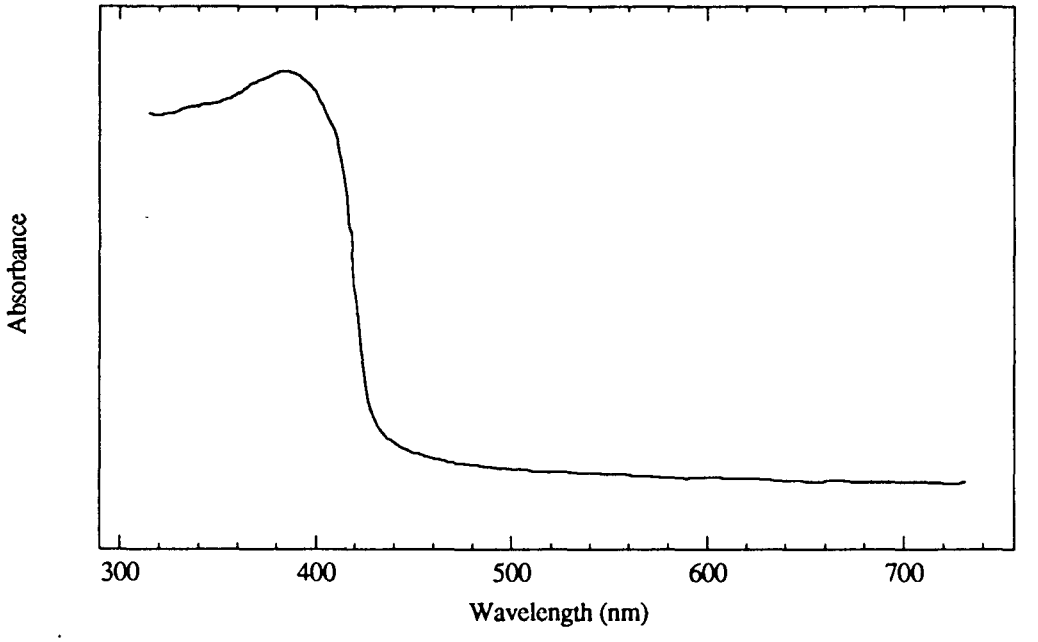

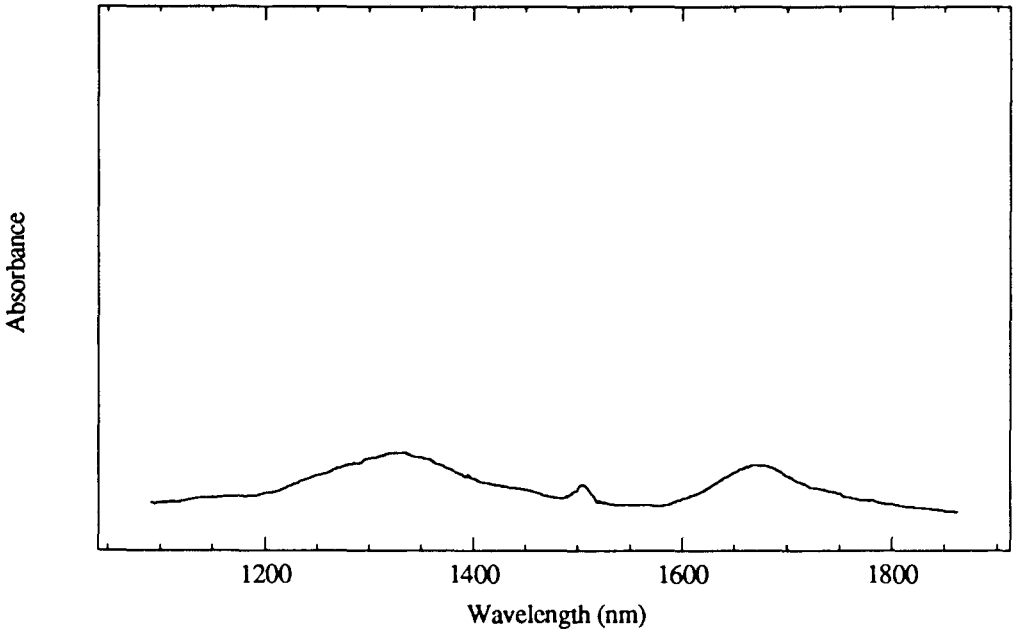

FIGURE 4.13 Absorption spectrum of $Pa(BH_3CH_3)_4$ in d_8-toluene in the (top) visible and (bottom) the near IR regions. Note that the two have different absorbance scales: (top) full scale = 2.0 and (bottom) full scale = 0.5. The small peak at 1,510 nm is due to solvent.

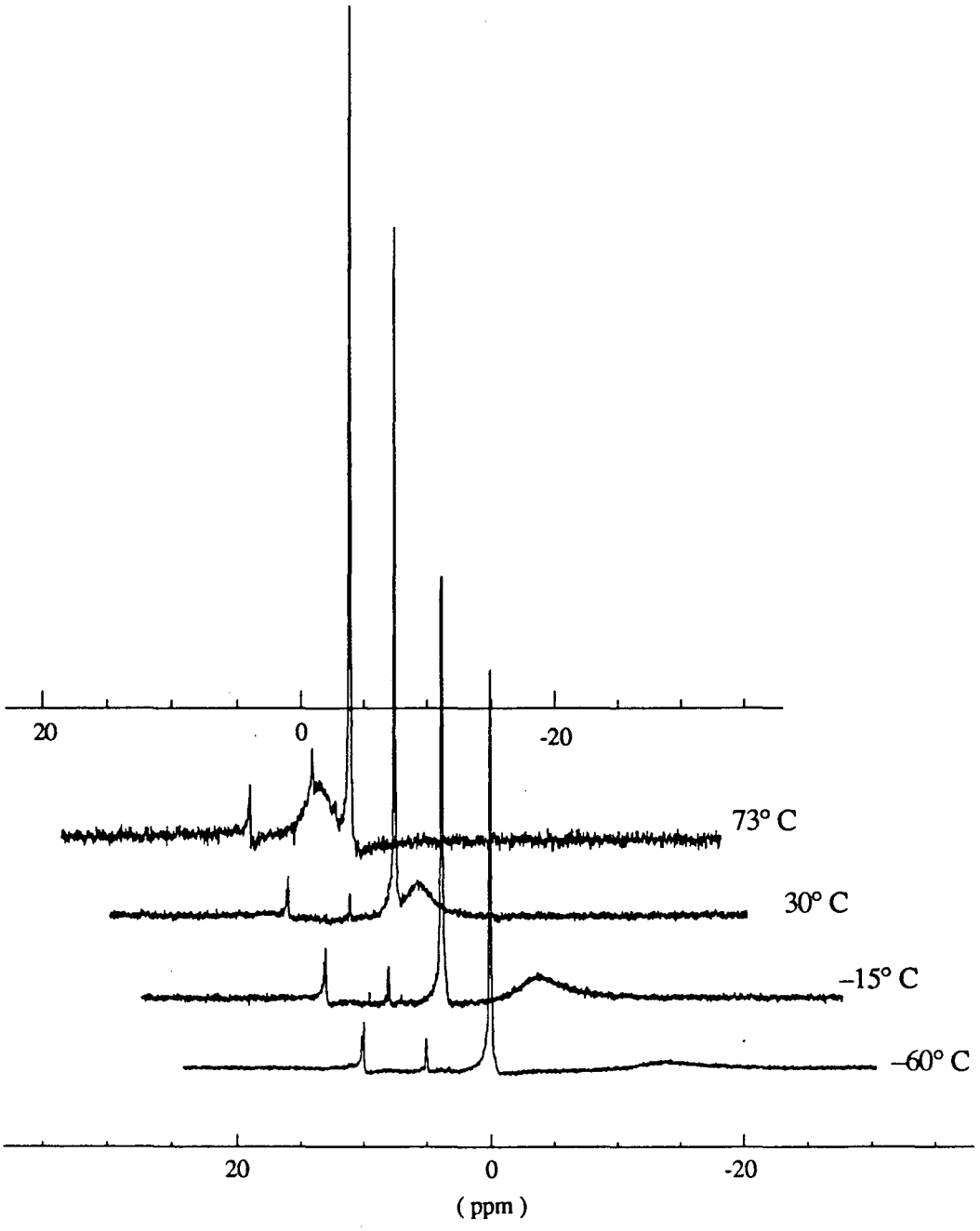

FIGURE 4.14 Variable temperature ^1H NMR spectra of $Pa(BH_3CH_3)_4$ in d_8-toluene.

$Pa(BH_3CH_3)_4$ was present in $Zr(BH_3CH_3)_4$ merely as a physical mixture or Pa^{4+} actually substituted Zr^{4+} in the crystal lattice of $Zr(BH_3CH_3)_4$; $Pa(BH_4)_4$ was found to retain its polymeric structure and did not 'cosublime' with $Zr(BH_4)_4$ [28].

4.7 Electronic Structure of $Pa(BH_3CH_3)_4$

For an f-electron system in a cubic site symmetry, the crystal-field Hamiltonian (2.4) becomes

$$\mathcal{H}_{crystal\text{-}field} = B_0^4 \left[C_0^4 + \sqrt{\frac{5}{14}}\,(C_4^4 + C_{-4}^4)\right] + B_0^6 \left[C_0^6 - \sqrt{\frac{7}{2}}\,(C_4^6 + C_{-4}^6)\right] \qquad (4.2)$$

and only two parameters, B_0^4 and B_0^6, are required to describe the crystal-field. The calculated spin-orbit coupling constant ζ_{5f} of the Pa^{4+} free ion is 1,834 cm^{-1} [63] and the ground term of $^2F_{5/2}$ is ≈ 5,500 cm^{-1} below $^2F_{7/2}$. As shown in Table 2.1, the free-ion terms are split by a crystal-field of T_d symmetry according to: $^2F_{5/2} \rightarrow \Gamma_6, \Gamma_8$ and $^2F_{7/2} \rightarrow \Gamma_6, \Gamma_7$ and Γ_8; states with labels Γ_6 and Γ_7 are Kramers doublets while Γ_8 is a quartet. To first order (i.e. assuming no J mixing by the crystal-field occurs), states arising from $^2F_{5/2}$ are not affected by the sixth-order crystal-field and their energies are dependent on the fourth-order term only. Lea *et al.* have calculated eigenvectors and eigenvalues for various J states in a cubic crystal-field as a function of the ratio of the two crystal-field parameters [64]. If a tetrahedral coordination is assumed in $Pa(BH_3CH_3)_4$ with ligands located at alternate vertices of a cube, B_0^4 is found to be negative from a point charge model; and from the tabulated eigenvalues, a negative B_0^4 predicts Γ_8 to be the ground state. But Banks [28] and Bernstein et al. [19] have found that a 12-coordination model, with hydrogen atoms located at the mid-point of every edge of a cube, is more suitable for the description of the electronic structures in $Np(BH_4)_4$ and $U(BH_4)_4$:$Hf(BH_4)_4$; the 4-coordination model predicts the wrong ground states in both cases. Using the 12-coordination model on the present $5f^1$ system, however, also results in a negative B_0^4 and so a Γ_8 ground state. In fact, among the many cubic symmetry f^1 crystal-fields, only the octahedral 6-coordination results in a positive B_0^4 and a Γ_7 ground state (the Kramers doublet

carries a label of Γ_7 in O_h symmetry) —— a cubic 8-coordination also gives a Γ_8 ground state —— and this has been experimentally confirmed in Cs_2PaCl_6 [50, 51]. The ground Kramers doublet Γ_7 in Cs_2PaCl_6 shows an isotropic EPR spectrum with rather sharp peak widths at low temperature (Fig 4.5). The Γ_8 state is at 2,108 cm^{-1} away and the calculated B_0^4 is 6,945 cm^{-1} [51]. Based on these considerations, the Γ_8 state is almost certain to be the ground state in $Pa(BH_3CH_3)_4$. No other f^1 complex with T_d symmetry is known despite the apparent interest in Ce^{3+} with a tetrahedral crystal-field which, with an anticipated Γ_8 ground state, has been discussed widely as a useful maser material [65]. Consequently, no comparison can be made concerning the ground f^1 Γ_8 state in $Pa(BH_3CH_3)_4$.

The magnetic behavior of the Γ_8 state is complicated [66]. Briefly, in a magnetic field, it gives rise to four levels which exhibit a linear Zeeman effect but they may not be evenly spaced, their ordering and position depend on the exact crystal-field. The calculated $|J, M_J\rangle$ wavefunctions for the Γ_8 state in $Pa(BH_3CH_3)_4$ using crystal-field parameters for $U(BD_4)_4$:$Hf(BD_4)_4$ [17] are

$$\begin{aligned} &0.962\ |\tfrac{5}{2}, \mp\tfrac{1}{2}\rangle + 0.207\ |\tfrac{7}{2}, \pm\tfrac{7}{2}\rangle - 0.177\ |\tfrac{7}{2}, \mp\tfrac{1}{2}\rangle \ldots \\ &-0.878\ |\tfrac{5}{2}, \pm\tfrac{5}{2}\rangle - 0.393\ |\tfrac{5}{2}, \mp\tfrac{3}{2}\rangle + 0.235\ |\tfrac{7}{2}, \mp\tfrac{3}{2}\rangle \ldots \end{aligned}$$

These wavefunctions are further admixed by a magnetic field, a field directed along the molecular four-fold axis will admix states with $\Delta M_J = \pm 4$ while a field along the three-fold axis will admix states with $\Delta M_J = \pm 3$. As a result, for a randomly oriented sample such as a powder, all six EPR transitions between the four levels are allowed. All transition probabilities, however, are expected to be small compared to that between the Kramers pair $|\pm\frac{1}{2}\rangle$. The calculated g-values for this transition using the wavefunctions from above are $g_{\parallel} = -0.82$ and $g_{\perp} = 2.08$; they were not observed experimentally. In addition to being anisotropic, these transitions are expected to have broad peaks because of fast spin-lattice relaxation and this seems to be the most likely reason why EPR was not observed. EPR transitions involving the Γ_8 state have been observed in other cubic systems (all degeneracies except the Kramers degeneracy are removed in systems with symmetries lower than cubic) but only under better experimental conditions —— rare-earth impurities diluted into single crystals are available; even

then the strong $|-\frac{1}{2}\rangle \rightarrow |\frac{1}{2}\rangle$ transition could not always be detected, for instance, it was absent in the EPR of Er^{3+}:CaO [67].

No EPR could be observed with $MeCp_4Pa$ either. If a tetrahedral coordination is assumed for $MeCp_4Pa$, the Γ_8 state will again form the electronic ground state and the same reasoning from above equally applies. However, the structure of Cp_4U is determined to be S_4 with four pentahapto Cp rings. There is therefore an uncertainty over the structure of $MeCp_4Pa$ and the Γ_8 state will split into two Kramers doublets upon lowering of the symmetry. Regardless of the exact electronic structure in $MeCp_4Pa$, which is a function of the structural deviation from the tetrahedral symmetry, the peak widths are expected to be broad; the ground Γ_6 doublet in Cp_4Np shows an EPR absorption but the peak is well over 800 G wide [68] and a sample of Cp_4Np diluted in Cp_4Th did not reduce the peak widths significantly. Diluting $MeCp_4Pa$ into $MeCp_4Th$ also did not result in an observable EPR signal. Consequently, the only Pa^{4+} EPR observed remain those of Pa^{4+} doped into single crystals of Cs_2PaCl_6 and ThX_4 (X = Cl, Br) [50, 69].

The absorption spectrum of $Pa(BH_3CH_3)_4$ shows two very weak and broad peaks centered at 1,330 nm ($\approx$ 7,520 cm^{-1}) and 1,670 nm ($\approx$ 5,990 cm^{-1}); they can be assigned as the crystal-field states arising from the free-ion term $F_{7/2}$; the third $F_{7/2}$ crystal-field state was not observed but probably occurred at a lower energy. They can be compared to those found at 1,420 nm and 1,620 nm in a solution of $Pa(BH_4)_4$ which were not assigned in that case because of an uncertainty over the symmetry of the compound at low temperature [28]. The calculated Γ_7 and Γ_6 states using crystal-field parameters for $U(BD_4)_4$:$Hf(BD_4)_4$ [17] are at 6,670 cm^{-1} and 7,520 cm^{-1} respectively, the ($F_{7/2}$) Γ_8 state was calculated to be at 4,340 cm^{-1}, a region difficult to investigate because of the decreased sensitivity of the spectrometer and a lack of suitable solvent. The strong absorption edge beginning at 430 nm ($\approx$ 23,250 cm^{-1}) is certainly due to the dipole-allowed $5f \rightarrow 6d$ transition, the corresponding transition in Cs_2PaCl_6 is found to be at 19,956 cm^{-1} [51]. A complete crystal-field analysis for either the *f*- or the *d*-configuration is not possible until the other crystal-field states are located. Strong emission from the excited $6d$ state should be most useful in locating the other $5f$ crystal-field states.

4.8 NMR of $Np(BH_3CH_3)_4$ and $Pa(BH_3CH_3)_4$

Because of the T_d molecular symmetry in $M(BH_3CH_3)_4$, their NMR studies are also of special interest since the dipolar contribution to the paramagnetic shift vanishes and interactions between the unpaired magnetic electrons and the ligand nuclei can be studied more conveniently. Gamp et al. [70] have studied the temperature dependence of the ^1H, ^{11}B and ^{13}C NMR in $U(BH_3CH_3)_4$ and found that the temperature dependence of the ^1H shifts could be fitted to a spin polarization mechanism, but that of the ^{11}B and ^{13}C shifts showed deviation from the same mechanism and covalency between the $5f$ and the ligand s and p orbitals had to be included to result in a better fit. Temperature dependence of the ^1H (bridging and terminal) and ^{11}B NMR spectra have been measured for $Pa(BH_3CH_3)_4$ and $Np(BH_3CH_3)_4$. Analysis of the present data follows closely that of Reference 70.

4.8.1 Theory of Paramagnetic NMR Shift

The theory of paramagnetic NMR shifts is complicated, only the more relevant aspects are summarized here. For a more comprehensive review, a number of references can be consulted [71].

The paramagnetic shift $\Delta H/H$ arises due to the hyperfine interaction between the magnetic nucleus with the surrounding electrons. In a solution, $\Delta H/H$, referenced to a diamagnetic analogue which is $Th(BH_3CH_3)_4$ in the present case, can be calculated as the average of the shifts along the three principal axes (x,y,z) of the molecular system found in the solid state [72]:

$$\Delta H/H = (3kT \sum_{\Gamma_n} e^{-\varepsilon_\Gamma/kT})^{-1} \times \sum_{i=x,y,z} \left\{ \sum_{\Gamma_n,\Gamma_m} e^{-\varepsilon_\Gamma/kT} \langle \Gamma_n | \mu_i | \Gamma_m \rangle \langle \Gamma_m | A_{N_i} / g_N \beta_N | \Gamma_n \rangle - \right.$$
$$\left. kT \sum_{\Gamma_n,\Gamma_m'(\Gamma_n \neq \Gamma_m')} \frac{(e^{-\varepsilon_\Gamma/kT} - e^{-\varepsilon_{\Gamma'}/kT})}{(\varepsilon_\Gamma - \varepsilon_{\Gamma'})} \langle \Gamma_n | \mu_i | \Gamma'_m \rangle \langle \Gamma'_m | A_{N_i} / g_N \beta_N | \Gamma_n \rangle \right\} \quad (4.3)$$

where

$$\mu_i = -\beta_e(L_i + g_e S_i) \tag{4.4}$$

and Γ (Γ') and ε_Γ ($\varepsilon_{\Gamma'}$) are the eigenfunction and eigenvalue of the field-independent Hamiltonian respectively while n and m are the Kramers degeneracies. For the present case, Γ labels the SLJ state with energy ε_Γ, and n and m label its M_J components which are degenerate in the absence of a magnetic field. The total orbital angular momentum and electron spin operators are represented by L_i and S_i respectively; β_e is the Bohr magneton and β_N is the nuclear magneton, g_e is the electron g-factor and g_N is the nuclear g factor. Finally, k is the Boltzmann constant and T is the temperature. It is seen that the problem is primarily one of evaluating the hyperfine matrix elements between electronic states. The hyperfine interaction operator $A_{N_i}/g_N\beta_N$ connects the nuclear and electron spins and contains contributions from three different terms:

i) the dipolar term which consists of the dipole interaction between the electron spin and the nuclear spin which, in the case of a T_d complex, averages to zero.

ii) the orbital term which represents the interaction between the nuclear magnetic moment and the magnetic field generated by the orbital angular momentum of the electrons. Obviously, this term is important only when quenching of the electron orbital angular momentum is not complete, which is the case for most lanthanide and actinide complexes and ligands with filled p-orbitals. It is, however, in general assumed that spin effects are small and in ligand p orbitals they average out in solution. Following reference 70, the orbital term is ignored in the following analysis.

iii) the Fermi contact term which describes the interaction of the magnetic nuclei with an unpaired spin at the nuclei. While it is recognized that only s-wavefunctions have a finite amplitude at the nucleus, any unpaired spin density around the nucleus can be transferred to the nucleus through a variety of mechanisms. In a paramagnetic complex, two mechanisms are generally important for transferring spin to the ligand nuclei —— spin polarization and covalency.

Both unrestricted Hartree-Fock calculations and experiments have shown that an unpaired electron density in atoms and ions causes "spin polarization" in the filled shells through exchange interaction [73]. The resultant difference in radial distributions of spins with opposite signs leads to a difference in s electron densities at the nucleus, i.e. $|\psi_\uparrow(0)|^2 - |\psi_\downarrow(0)|^2 \neq 0$, which contributes to the hyperfine interaction and the Fermi contact term is negative. A measure of this polarization is given by

$$\chi = (4\pi/S) \sum_{all\ shells} \left[|\psi_\uparrow(0)|^2 - |\psi_\downarrow(0)|^2 \right] \tag{4.5}$$

where S stands for the number of unpaired electrons. It has been found that χ, measured from the hyperfine interaction between the electrons and the metal nucleus, is roughly constant in transition metal ions, leading to the assumption that spin polarization is linear in total spin [74]. On the other side of the Fermi hole, polarized spin is also transferred to the ligand nuclei and manifest itself as superhyperfine interaction (the hyperfine interaction between metal electrons with ligand nuclei). Studies of ^{17}O NMR of lanthanides show that the shifts are Fermi contact in origin and the contact term is also negative, it is then proposed that electrons donated by ligands into the empty metal orbitals are polarized by the inner $4f$ electrons [75]. A second polarization mechanism involves polarization of the outer $5s$ and $5p$ electrons of the lanthanide ions by the $4f$ electrons and the unpaired spin density is then transferred to the ligands by overlap or covalent interaction [76]. Different polarization mechanisms cannot be distinguished easily in experiments; however, they all lead to a negative hyperfine interaction.

In the polarization model, the problem in evaluating (4.3) is the availability of the basis functions $|\Gamma m\rangle$ which are best obtained from an unrestricted Hartree-Fock calculation since exchange interaction is being studied; they are, of course, in general not known. Instead it is assumed that, similar to the situation in the transition metals, the hyperfine interaction is proportional to the spin of the f orbitals causing the polarization such that [77]

$$\langle \Gamma' m | A_{N_i}/g_N\beta_N | \Gamma n \rangle = (K/g_N\beta_N) \langle \Gamma' m | S_i | \Gamma n \rangle \tag{4.6}$$

where K is a proportional constant (hyperfine parameter) and the matrix elements $\langle \Gamma' m | S_i | \Gamma n \rangle$ can be calculated using $|SLJM_J\rangle$ as basis functions. As spin with a sign opposite to that of the unpaired spin in the f shell is transferred to the ligand orbitals, K has a negative sign. For an isotropic shift, the shift is calculated for the z direction so that (4.3) and (4.6) together give

$$\Delta H/H = (K/g_N\beta_N)\,\langle S_z\rangle / H \tag{4.7}$$

and the average total electronic spin $\langle S_z\rangle$ is given by

$$\langle S_z\rangle/H = \beta_e(kT\sum_{\Gamma_n} e^{-\varepsilon_\Gamma/kT})^{-1} \times \Bigg\{ \sum_{\Gamma_n,\Gamma_m} e^{-\varepsilon_\Gamma/kT} \langle \Gamma_n | L_z + g_e S_z | \Gamma_m \rangle \langle \Gamma_m | S_z | \Gamma_n \rangle - kT \sum_{\Gamma_n,\Gamma_m(\Gamma_n \neq \Gamma_m')} \frac{(e^{-\varepsilon_\Gamma/kT} - e^{-\varepsilon_{\Gamma'}/kT})}{(\varepsilon_\Gamma - \varepsilon_{\Gamma'})} \langle \Gamma_n | L_z + g_e S_z | \Gamma'_m \rangle \langle \Gamma'_m | S_z | \Gamma_n \rangle \Bigg\} \tag{4.8}$$

If J-mixing is ignored, the operator equivalents $L_z + g_e S_z = g_J J_z$ and $S_z = (g_J - 1)J_z$ can be substituted into (4.8) where g_J is the Landé g factor. It is then seen that the sign of the shifts is determined by the sign of $g_J(1-g_J)K$. Note that g_J is less than 1 for ions with less than a half-filled shell and the polarization mechanism predicts a negative shift for a negative hyperfine parameter K; a positive shift is expected for ions with more than a half-filled shell. Sign conventions found in published literature are such that shifts to high field are positive, opposite to the one being used here and in most synthetic work; the negative sign of K is, however, retained here since it has a physical meaning and allows for consistent for comparison with other results. The important point to note of these theoretical considerations is that *the polarization mechanism predicts a downfield isotropic shift for* f^n *(n < 7) ions and that the temperature dependence of the isotropic shifts is a function of* $\langle S_z\rangle/H$ *with a coupling constant* K.

For a covalent model, the problem is more complex. Axe and Burns [78] first applied a semiempirical MO study to ligand field splittings and transferred hyperfine effects in Tm^{2+}:CaF_2 and Tm^{2+}:SrF_2, obtaining a positive hyperfine constant. Spin-transfer studied by

ENDOR in Yb^{3+}:CaF_2 also revealed a covalent and positive hyperfine interaction [79]. Although spin transferred by a covalent mechanism generally results in a positive Fermi term and hence a shift opposite to that caused by polarization, exceptions are known to exist [80] and there is no simple principle to predict the sign of the shift. Analysis of the present data using a covalent model has not been attempted.

4.8.2 ^{1}H and ^{11}B NMR of $Np(BH_3CH_3)_4$

Figure 4.15 shows the ^{1}H NMR spectrum of $Np(BH_3CH_3)_4$ at room temperature. The peak of the bridging protons at 182 ppm is very broad ($\nu_{1/2}$ = 750 Hz at 30° C) because of its proximity to a paramagnetic center and quadrupole broadening with ^{10,11}B. As the temperature is lowered, it undergoes further broadening to ≈ 1,500 Hz at –70° C. Temperature dependences of the ^{1}H and ^{11}B isotropic shifts found in $Np(BH_3CH_3)_4$ and $Pa(BH_3CH_3)_4$ are shown in Figure 4.16; those found in $U(BH_3CH_3)_4$ are included for comparison.

Similar to $U(BH_3CH_3)_4$, all paramagnetic shifts in $Np(BH_3CH_3)_4$ are to low field, suggesting that the dominating spin-transfer mechanism is spin polarization. Rajnak et al. have obtained crystal-field parameters for $Np(BD_4)_4$ from an analysis of the optical spectrum of $Np(BD_4)_4$:$Zr(BD_4)_4$ and found that introduction of an orbital reduction factor k = 0.862 was needed before those parameters could be used to fit satisfactorily the measured magnetic susceptibility and the EPR spectrum of $Np(BH_3CH_3)_4$ [18]. Values of $\langle S_z \rangle/H$ can be calculated from equation (4.8) using these parameters and the same orbital reduction factor. The results are shown in Figure 4.17, they show a slight curvature and approach linear T^{-1} dependence as the first excited crystal-field state is relatively high in energy (385 cm^{-1}). Use of an orbital reduction factor changes the operator $L_z + g_e S_z$ in (4.8) to $kL_z + g_e S_z$ but does not alter the temperature dependence of $\langle S_z \rangle/H$, only the magnitude of $\langle S_z \rangle/H$ and hence the hyperfine parameter K, are changed. Since k is found necessary to give good fit to the magnetic data in $Np(BH_3CH_3)_4$ and, more importantly, to obtain a consistent comparison with the NMR data in $U(BH_3CH_3)_4$, it was included in the present calculation. The experimental ^{1}H and ^{11}B shifts are then least-squares fitted according to (4.7) and the results are shown in Figure 4.16 and Table 4.4. Similar conclusion to those found in $U(BH_3CH_3)_4$ can be drawn —— the good fit between

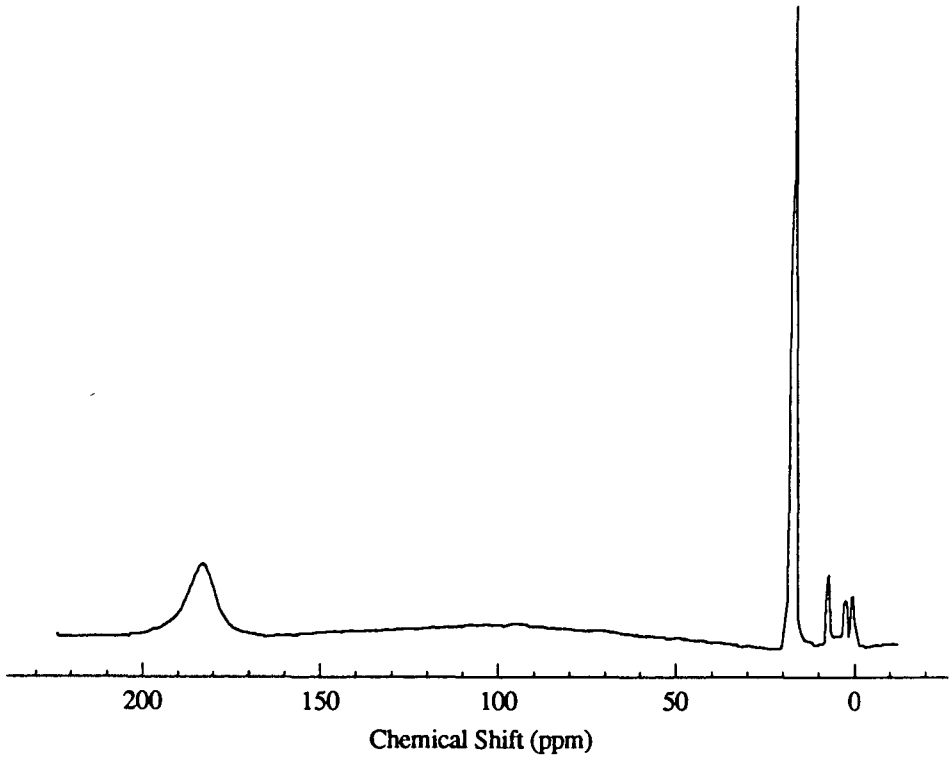

FIGURE 4.15 Room-temperature ^1H NMR spectrum of $Np(BH_3CH_3)_4$ in d_8-toluene. A grease peak is present at ≈ 0.2 ppm.

	H_{bridge}	$H_{terminal}$	B
$U(BH_3CH_3)_4$ K (MHz)	–5.640	–0.588	–1.093
standard dev (ppm)	0.43	0.18	9.76
$Np(BH_3CH_3)_4$ K (MHz)	–5.177	–0.498	–1.053
standard dev (ppm)	1.21	0.24	5.45

TABLE 4.4 Fitted Values of the Hyperfine Parameters K for $U(BH_3CH_3)_4$ (From Ref. 70) and $Np(BH_3CH_3)_4$

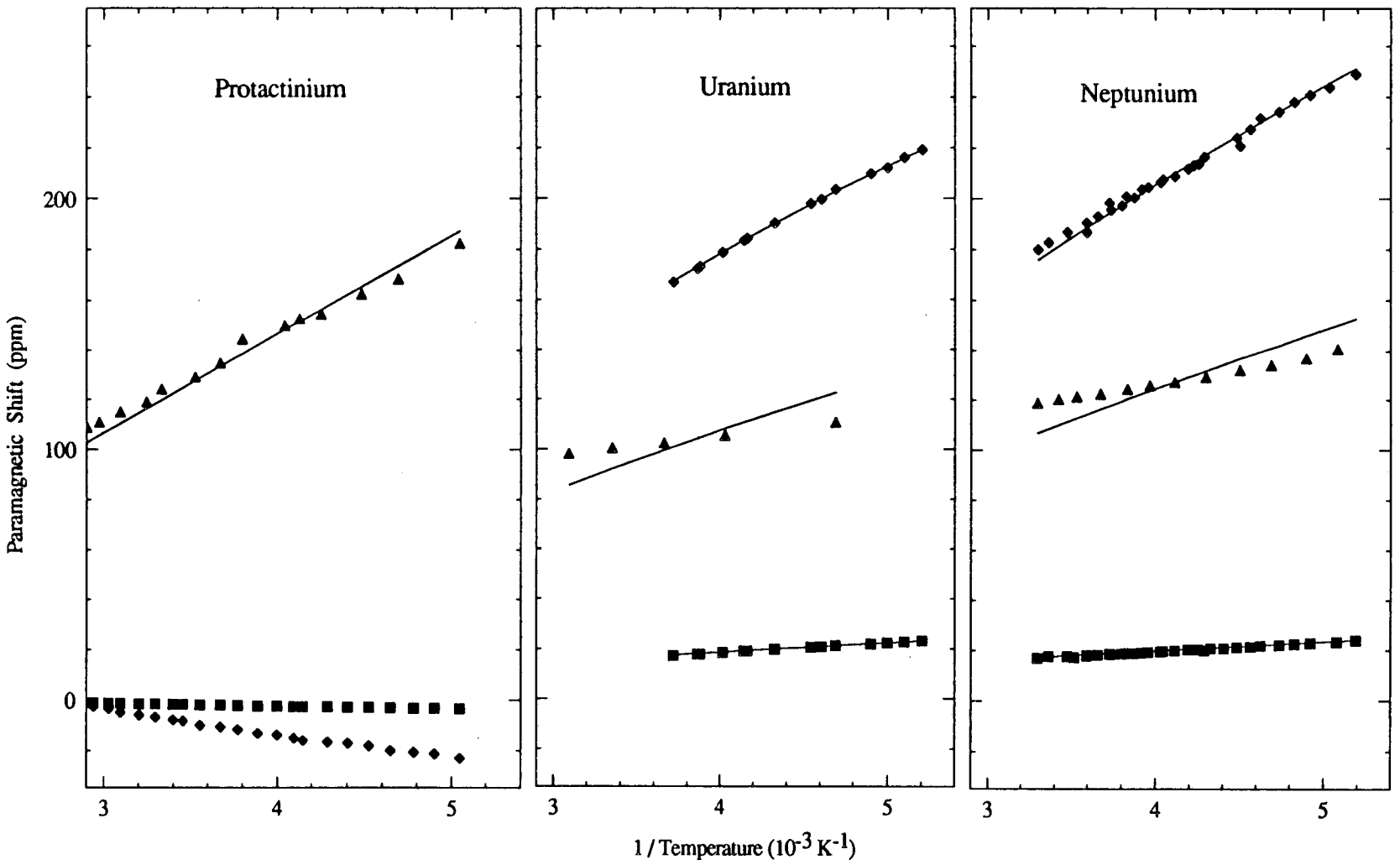

FIGURE 4.16 Temperature dependences of the ^{1}H and ^{11}B paramagnetic shifts of $Pa(BH_3CH_3)_4$, $U(BH_3CH_3)_4$ (from Ref. 70) and $Np(BH_3CH_3)_4$. (♦ : bridging proton, ■ : terminal proton, ▲: boron, line is least-squares fit, see text.)

the ^1H shifts and (4.7) is strong evidence that the spin polarization is the dominant spin-transfer mechanism while the disagreement between the temperature dependences of the ^{11}B isotropic shifts and the calculated $\langle S_z \rangle / H$ indicates that a second mechanism must also be important. Inclusion of covalency shall necessarily improve the fit to the ^{11}B shifts since it amounts to addition of an extra variable; it was not attempted. The hyperfine parameters obtained here are 5-10% smaller than those found in $U(BH_3CH_3)_4$. Although it is reasonable to assume these parameters to be dependent primarily on the *5f* radial distributions, it is not evident what significance can be attached to them because different orbital reduction factors have been used in the fitting (0.85 for $U(BH_3CH_3)_4$ and 0.862 for $Np(BH_3CH_3)_4$). Additionally, it has been shown by Reuben and Fiat [81], when the assumption that the dipolar shifts are the same throughout the series, that the ^{17}O hyperfine coupling parameter is roughly constant in the lanthanides. However, it is obvious that the polarization model adequately describes the ^1H isotropic shifts in $Np(BH_3CH_3)_4$ as in $U(BH_3CH_3)_4$.

4.8.3 ^1H and ^{11}B NMR of $Pa(BH_3CH_3)_4$

No NMR data of any Pa compound has ever been reported; the variable temperature ^1H NMR of $Pa(BH_3CH_3)_4$ (Fig 4.14) and $MeCp_4Pa$ (Fig 4.9 and 4.10) represent the first Pa PMR spectra. Apart from the bridging protons peak of $Pa(BH_3CH_3)_4$ ($\nu_{1/2}$ = 150 Hz at 30° C), the peak widths are rather narrow (12 – 25 Hz) and are comparable to or even sharper than those found in known Ce(III) and U(V) compounds (e.g. $\nu_{1/2}$ = 20 – 58 Hz in $MeCp_3Ce$ [82] and 30 – 150 Hz in $MeCp_3UNCMe_3$ [83]), suggesting electronic spin-relaxation is indeed rapid as discussed in Section 4.7. In addition, they do not show large variation with temperature, with the exception of the bridging protons peak of $Pa(BH_3CH_3)_4$ which broadens rapidly with low temperature and becomes undetectable at about –60°C. Similar to the thorium and uranium analogues [84], the A A'BB'X structure of $MeCp_4Pa$ cannot be resolved and the methyl protons have a chemical shift of –0.03 ppm while the ring protons are found at 1.47 and -2.16 ppm. They are upfield relative to those of $MeCp_4Th$ and the chemical shifts of the ring protons fall in

M	X (ppm)	A (A') (ppm)	B(B') (ppm)
Th[a]	2.17	5.91	6.31
Pa	–0.03	1.47	–2.16
U[a]	0.94	–13.47	–14.89
Np[b]		(–16.0)	(–16.0)

TABLE 4.5 The A A'BB'X ^{1}H NMR spectra of $MeCp_4M$ at 30° C. [a]From Reference 84. [b]Chemical shifts are for Cp_4Np, from Reference 85.

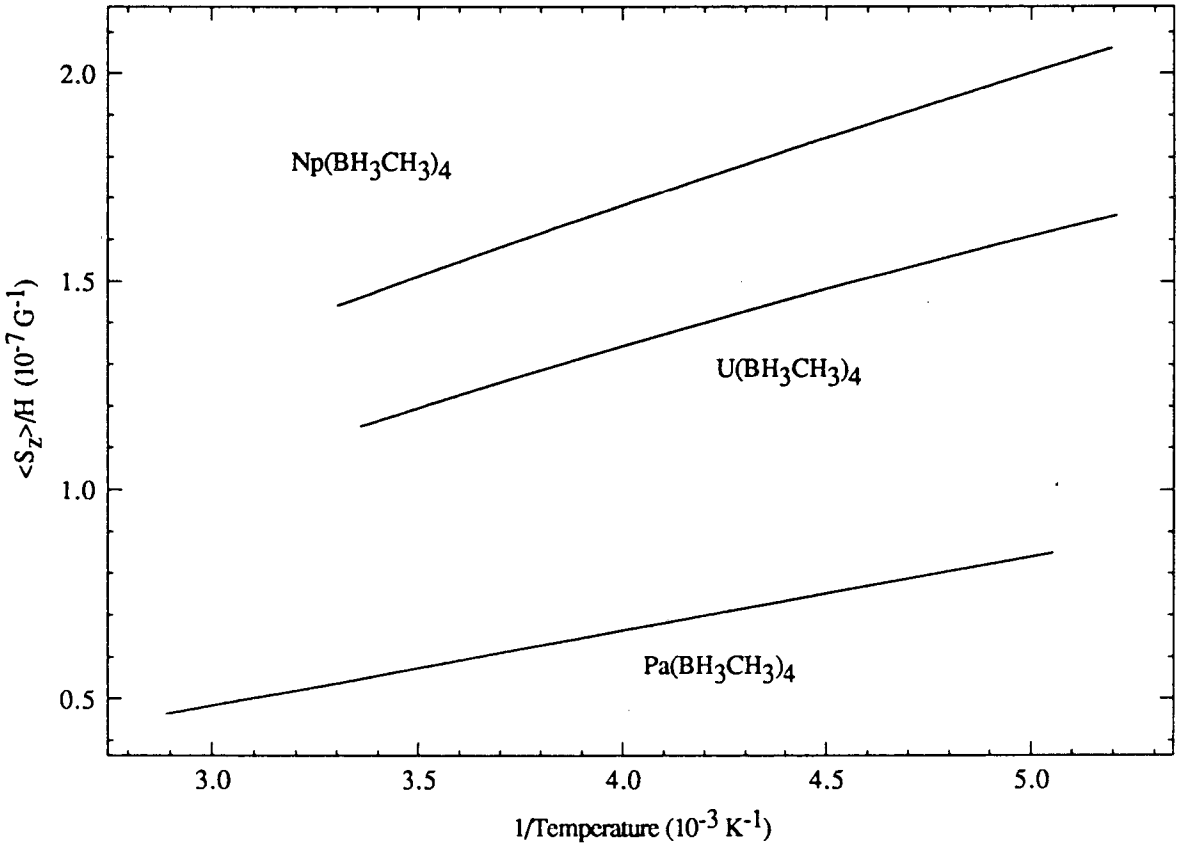

FIGURE 4.17 Calculated values of $\langle S_z \rangle / H$ for $Pa(BH_3CH_3)_4$, $U(BH_3CH_3)_4$ (from Ref 70) and $Np(BH_3CH_3)_4$.

the expected range when the chemical shifts of $MeCp_4M$ (M = Th, U and Np) are interpolated [84, 85] (Table 4.5). If it is assumed that they all have T_d symmetries in solution, these chemical shifts of the ring protons reflect a relatively smooth variation of the isotropic shift across the series.

It is at once obvious from Figure 4.16 that the polarization mechanism alone is inadequate in describing the spin-transferring process in $Pa(BH_3CH_3)_4$; while the ^{11}B isotropic shifts are to low-field as in $U(BH_3CH_3)_4$ and $Np(BH_3CH_3)_4$, those for the bridging and terminal protons are to upfield, opposite to that predicted by the polarization model. A complete crystal-field analysis is not presently possible for $Pa(BH_3CH_3)_4$, an estimate of $\langle S_z \rangle / H$ can nonetheless be obtained by using the crystal-field parameters of $U(BD_4)_4$:$Hf(BD_4)_4$, and the calculated values are shown in Figure 4.17. The estimate is probably a good one since the excited crystal-field states are not expected to be low-lying (the calculated first excited state of Γ_6 is at 350 cm^{-1}) and the ground Γ_8 state is to first order independent on the sixth-order parameter. The calculated $\langle S_z \rangle / H$ is rather small and compared to the analogous f^2 and f^3 systems; it should be noted that the measured susceptibility of Cp_4Pa also shows a very low magnetic moment [86]. The calculated $\langle S_z \rangle / H$, together with the hyperfine parameters K found for $U(BH_3CH_3)_4$ or $Np(BH_3CH_3)_4$, predict the room-temperature isotropic shifts in $Pa(BH_3CH_3)_4$ to be at ≈ 80 ppm and ≈ 8 ppm for the bridging and terminal protons respectively. This explains why the ^1H NMR of $Pa(BH_3CH_3)_4$, when first observed (Section 4.6), was totally unexpected. A different spin-transfer mechanism is dominant in $Pa(BH_3CH_3)_4$. The (negative) temperature dependence of the calculated $\langle S_z \rangle / H$ also deviates from that of the data, suggesting that the second spin-transferring mechanism does not bear a simple relation with $\langle S_z \rangle / H$, or it may merely be due to the inadequacy of using the $U(BD_4)_4$:$Hf(BD_4)_4$ crystal-field parameters. This second mechanism is not important in the ^1H NMR of $U(BH_3CH_3)_4$ and $Np(BH_3CH_3)_4$ but must produce a rather large upfield shift (≈ 90 ppm) for the bridging protons in $Pa(BH_3CH_3)_4$ if the spin polarization effect is assumed to be linear in total spin as in the transition metals.

The ^{11}B isotropic shifts found for $Pa(BH_3CH_3)_4$ occur at an even lower field than those in $U(BH_3CH_3)_4$ and $Np(BH_3CH_3)_4$ while a linear dependence of the shifts on the total spin would predict them to occur at a higher field of ≈ 60 ppm. Using the calculated values for $\langle S_z \rangle / H$ from above results in a hyperfine parameter of –3.01 MHz; the calculated fit is shown in

Figure 4.16. It is difficult to ascribe these very large observed shifts to polarization alone although the fit appears to be better than in the U and Np analogues. Since polarization alone cannot adequately describe the ^{11}B isotropic shifts in both $U(BH_3CH_3)_4$ and $Np(BH_3CH_3)_4$ or the ^{1}H shifts in $Pa(BH_3CH_3)_4$, it is expected that a second mechanism is also important in describing the ^{11}B shifts in $Pa(BH_3CH_3)_4$. It appears that this mechanism is cooperative with polarization but it cancels the ^{1}H downfield shifts predicted by polarization. While it is natural to assume the second mechanism important in transferring spin density to both ^{1}H and ^{11}B is the same and point to covalency as this mechanism, a much more detailed analysis is needed before any definite conclusion can be drawn. It is only repeated that spin-polarization does not explain qualitatively the observed NMR data in $Pa(BH_3CH_3)_4$.

4.9 Summary

In addition to the difficulties associated with its handling, availability of protactinium is a major problem in its study. The somewhat unexpected solubility of protactinium (V) chloride in aromatic solvents such as toluene and chlorobenzene has been exploited to repeat the syntheses of $Pa(BH_4)_4$ and $(CH_3C_5H_4)_4Pa$, simplifying the procedure and improving the yields. The use of protactinium (V) chloride in aromatic solvents should facilitate the synthesis of most protactinium (IV) and (V) compounds; even novel trivalent compounds may be accessible (e.g. Cp_3Pa is the only missing member in the series Cp_3An, Cp = various substituted and unsubstituted cyclopentadienyl and An = Th – Cf). Reaction of $PaCl_5$ or $PaCl_4$ with $LiBH_3CH_3$ produced the highly volatile $Pa(BH_3CH_3)_4$. Failure to observe any EPR signal with $Pa(BH_3CH_3)_4$ and $(CH_3C_5H_4)_4Pa$ is most likely due to the fact that their electronic ground states are the quartet Γ_8; the magnetic anisotropy together with rapid spin-lattice relaxation probably cause peak-broadening beyond observation of a signal. Two excited crystal-field states of $Pa(BH_3CH_3)_4$ were located and they show reasonable agreement with those predicted by the crystal-field parameters of $U(BD_4)_4$:$Hf(BD_4)_4$. A complete crystal-field analysis, however, cannot be performed until the rest of crystal-field states are located.

The first NMR spectra of a compound of protactinium —— $(CH_3C_5H_4)_4Pa$ (^1H) and $Pa(BH_3CH_3)_4$ (^1H and ^{11}B) —— were recorded. The $(CH_3C_5H_4)_4Pa$ spectra show expected chemical shifts but not those of $Pa(BH_3CH_3)_4$. The spin-polarization mechanism which shows success in interpreting the temperature dependence of the ^1H isotropic shifts in $U(BH_3CH_3)_4$ is shown to be an equally adequate model for $Np(BH_3CH_3)_4$; the hyperfine parameters are ≈10% smaller than those of $U(BH_3CH_3)_4$. The same model, however, cannot explain the sign of the ^1H upfield shifts nor the magnitude of the ^{11}B downfield shifts in $Pa(BH_3CH_3)_4$. A second spin-transferring mechanism such as covalency is important but a more detailed analysis must await more data. There is therefore a qualitative difference, based on these results, in the metal-ligand interactions between $Pa(BH_3CH_3)_4$ and its uranium and neptunium analogues.

4.10 Experimental

All manipulations were conducted under an inert atmosphere on a Schlenk line or in an inert-atmosphere glovebox. Solvents were dried and purged according to standard procedures. The ^{1}H (89.5 MHz) and ^{11}B (28.7 MHz) NMR spectra were recorded on a JEOL FX-90Q spectrometer and referred to tetramethylsilane and boron trifluoride etherate, respectively; a positive sign indicating downfield shift. The IR spectra were recorded on a Perkin-Elmer 297 spectrometer. Mass spectra were obtained with Atlas MS-12 and Consolidated 12-110 instruments at the U. C. Berkeley mass spectroscopy laboratory.

All radioactivity was handled inside a negative-pressure Berkeley box. All EPR, NMR and absorption samples were doubly contained and decontaminated before each experiment.

Preparation of $CsUCl_6$

A orange-yellow solution of $UCl_5 \cdot SOCl_2$ was prepared by refluxing 25 g of UO_3 powder with $SOCl_2$ for a week, its identity was established by absorption spectroscopy. Instead of adding ICl [87] to increase the solubility of CsCl in $SOCl_2$, 5 g of CsCl was added to this solution and then refluxed for 1 day. The solution was then allowed to cool and filtered to give 11.5 g of pale yellow $CsUCl_6$ which was washed with CH_2Cl_2 and dried under vacuum before use. No unreacted CsCl in the final product was found by powder diffraction.

Preparation of Cs_2NpCl_6 and Cs_2PuCl_6

Stock solutions of Np and Pu were obtained by dissolving respectively NpO_2 and PuO_2 in concentrated HCl/HNO_3 and the tetravalent state was prepared by electrochemical reduction. The reduction was monitored by absorption and the solution contained over 99% of the tetravalent state. Absorption spectroscopy also determined the concentration of the solution. A slight excess of CsCl (2.5 equivalents) was added to these solutions. Cs_2NpCl_6 was precipitated by saturating the solution with HCl gas; Cs_2PuCl_6 was obtained by slow evaporation. Both were washed with ethanol and dried under vacuum before use. They were identified by powder diffraction.

Preparation of $Cp_2Zr(H)BH_3CH_3$.

Commercially available Cp_2ZrCl_2 (1.2 g, 4.1 mmol; Alfa Inorganic) was mixed with $LiBH_3CH_3$ (0.36 g, 10 mmol) and stirred for 12 h in either diethyl ether or chlorobenzene. Alternatively, a THF solution of CpNa (10 mmol) was added to 1.04 g (5 mmol) of $Zr(BH_3CH_3)_4$ in diethyl ether. In both cases, the colorless solution gradually attained a pale yellow color. After removal of the solvent by vacuum, the pale yellow residue was sublimed at 60 °C and white needle-shaped crystals were collected on a 0 °C cold finger. Yield is 0.4 g, 35%.

MS data (EI): 249 (relative intensity 100, $Cp_2{}^{90}Zr^{11}BH_3CH_3{}^+$), 235 (70, M – CH_3), 221 (19, M – BH_3CH_3). ^1H NMR (d_8-toluene, 30 °C): 5.61 (10 H, s), 4.16 (1 H, s), 0.51 (3 H, s), -1.20 (3 H, br, quart). ^{11}B NMR (d_8-toluene, 30 °C): 20.2 (quart). IR (Nujol, KBr): 2388s, 2240w, 2078w, 1903s, 1850m, 1810sh, 1720w, 1610m, 1595sh, 1290w, 1260w, 1125s, 1065w, 1010s, 993w, 855w, 830sh, 808s.

Preparation of $Cp_2Zr(D)BD_3CH_3$.

The deuterated compound was prepared as above with the substitution of $LiBD_3CH_3$ for $LiBH_3CH_3$, $LiBD_3CH_3$ in turn was obtained by reacting $LiAlD_4$ with $(CH_3)_3B$. ^1H NMR (d_8-toluene, 30 °C): 5.61 (10 H, s), 0.51 (3 H, s). IR (Nujol, KBr): 1775m, 1720m, 1610m, 1290w, 1260w, 1205w, 1150m, 1115w, 1065w, 1030s, 1010s, 972w, 910w, 830sh. 808s, 735m, 720m.

Preparation of $Cp_2TiBH_3CH_3$.

Cp_2TiCl_2 (1.6 g, 6.5 mmole) and $LiBH_3CH_3$ (0.6 g, 16.5 mmole) was mixed and diethyl ether was added. The color turned from reddish brown to purple instantly with evolution of a gas. After 12 h of reaction, the solvent was removed and the residue was sublimed at 50° C onto a 0° C cold finger. The yield of the purple needle-shaped crystals was 0.65 g, 50%.

MS data (CI): 206 (relative intensity 28, M – H), 192 (32, M – CH_3) and 178 (100, M – BH_3CH_3). Elemental analysis: $C_{11}H_{16}BTi$ requires 63.839% C and 7.792% H, found

63.77% C and 7.91% H. IR (Nujol, KBr): 2598w, 2366s, 2250sh, 2234m, 2070m, 1980m, 1880s, 1835s, 1810sh, 1735m, 1620m, 1292m, 1260m, 1128s, 1010s, 902m, 845sh, 825sh, 800s. m. p. = 84 - 86° C.

X-ray powder diffraction data:

The following cell dimensions determined from single crystal diffraction are used in the calculation: $\alpha = \beta = \gamma = 90°$ and a = 13.192 Å, b = 9.330 Å and c = 8.931 Å.

$\sin^2\theta_{(obs)}$	I (obs)	$\sin^2\theta_{(cal)}$	I (cal)	*h,k,l*
0.01366	M–	0.01366	101	200
0.01778	S+	0.01769	1998	11±1
0.02742	S	0.02731	247	020
0.02971	M+	0.02980	265	00±2
0.04104	M+	0.04097	87	220
		0.04346	31	20±2
0.04511	M	0.04501	95	31±1
		0.05464	4	400
0.05711	W	0.05711	78	02±2
		0.07077	64	22±2
0.07096	W, broad	0.07231	110	13±1
0.07760	W+	0.07730	138	11±3
		0.08195	14	420
0.08414	W	0.08444	34	40±2
0.09885	M	0.09963	190	33±1, 51±1
0.10465	W	0.10462	54	31±3
		0.10923	5	040
0.11197	W	0.11175	53	42±2
0.11979	W–	0.11921	24	00±4
		0.12289	22	240
0.12265	W+	0.12294	17	600
0.13166	W	0.13191	34	13±3
0.13284	W	0.13287	26	20±4
		0.13904	4	04±2
0.14706	W	0.14652	24	02±4

References

[1] A. J. Freeman in Handbo*ok on the Physics and Chemistry of the Actinides* edited by A. J. Freeman and G. H. Lander (North-Holland, Amsterdam, 1984).

[2] H. L. Skriver, O. K. Andersen and B. Johansson, Phy. Rev. Lett. **41**, 42 (1978).

[3] W. Kolbe and N. Edelstein, Phy. Rev. B **4**, 2869 (1971).

[4] J. A. Stone and E. R. Jones, Jr., J. Chem. Phys. **54**, 1713 (1971).

[5] M. E. Hendricks, E. R. Jones, Jr., J. A. Stone and D. G. Karraker, J. Chem. Phys. **55**, 2993 (1971).

[6] E. R. Jones, Jr., M. E. Hendricks, J. A. Stone and D. G. Karraker, J. Chem. Phys. **60**, 2088 (1974).

[7] R. D. Fowler, B. T. Matthias, L. B. Asprey, H. H. Hill, J. D. G. Lindsay, C. E. Olsen and R. W. White, Phy. Rev. Lett. **15**, 860 (1965).

[8] (a) H. H. Hill, Physica **55**, 186 (1971). (b) B. Johansson, Phy. Rev. B **11**, 2740 (1975).

[9] (a) J. L. Smith, J. C. Spirlet and W. Müller, Science **205**, 188 (1979). (b) R. O. A. Hall, J. A. Lee and M. J. Mortimer, J. Low Temp. Phys. **27**, 305 (1977). (c) B. M. Bansal, Ph. D. Dissertation, University of California at Berkeley (1966). (d) R. L. Dod, Ph. D. Dissertation, University of California at Berkeley (1972).

[10] H. W. Kirby in *The Chemistry of the Actinide Elements*, Vol. 1, Second Edition, edited by J. J. Katz, G. T. Seaborg and L. R. Morss (Chapman and Hall, London, 1986).

[11] D. Brown, G. de Paoli and B. Whittaker, United Kingdom Atomic Energy Authority Report AERE-R8367 (1976).

[12] F. A. Cotton and G. Wilkinson, *Advanced Inorganic Chemistry*, Second Edition (Wiley-Interscience, New York, 1966).

[13] F. Baumgärtner, E. O. Fischer, B. Kanellakopulos and P. Laubereau, Angew. Chem. Int. Ed. Engl **8**, 202 (1969).

[14] D. F. Starks, T. C. Parsons, A. Streitweiser, Jr., and N. Edelstein, Inorg. Chem. **13**, 1307 (1974).

[15] J. P. Solar, H. P. G. Burghad, R. H. Banks, A. Streitweiser, Jr., and D. Brown, Inorg. Chem. **19**, 2186 (1980).

[16] R. H. Banks, N. M. Edelstein, R. R. Rietz, D. H. Templeton and A. Zalkin, J. Am. Chem. Soc. **100**, 1857 (1978).

[17] K. Rajnak, E. Gamp, R. Shinomoto and N. Edelstein, J. Chem. Phys. **80**, 5943 (1984).

[18] K. Rajnak, R. H. Banks, E. Gamp and N. Edelstein, J. Chem. Phys. **80**, 5951 (1984).

[19] E. R. Bernstein and T. A. Keiderling, J. Chem. Phys. **59**, 2105 (1973).

[20] C. J. Ballhausen, Theoret. Chim. Acta (Berl.) **24**, 234 (1972).

[21] R. Shinomoto, E. Gamp, N. M. Edelstein, D. H. Templeton and A. Zalkin, Inorg. Chem. **22**, 2351 (1983).

[22] D. F. Starks, unpublished result.

[23] L. Astheimer and K. Schwochau, Inorg. Nucl. Chem. **35**, 223 (1973).

[24] H. C. Brown and H. M. Hess, J. Org. Chem. **34**, 2206 (1969).

[25] R. B. King, Z. Naturforsch., Teil B **18**, 152 (1963).

[26] C. R. Lucas and M. L. H. Green, J. Chem. Soc. Chem. Commun., 1005 (1972).

[27] T. J. Marks and W. J. Kennelly, J. Am. Chem. Soc. **97**, 1439 (1975).

[28] R. H. Banks, Ph. D. Dissertation, University of California at Berkeley (1979).

[29] R. S. Shinomoto, Ph. D. Dissertation, University of California at Berkeley (1984).

[30] R. D. Shannon, Acta Cryst. **A32**, 751 (1976).

[31] (a) A. C. Bond and F. L. Himpsl, Jr., J. Am. Chem. Soc. **99**, 6906 (1977). (b) V. M. Ehemann and H. Nöth, Z. Anorg. Allg. Chem. **386**, 87 (1971).

[32] K. Schwochau and L. Astheimer, J. Inorg. Nucl. Chem. **32**, 119 (1970).

[33] L. J. Nugent, R. D. Baybarz, J. L. Burnett and J. L. Ryan, J. Phys. Chem. **17**, 1528 (1973).

[34] H. J. Wasserman, D. C. Moody and R. R. Ryan, J. Chem. Soc. Chem. Commun., 532 (1984).

[35] (a) D. S. Marynick and W. N. Lipscomb, J. Am. Chem. Soc. **94**,4461 (1972). (b) R. Ahlrichs, Chem. Phys. Lett. **19**, 174 (1973).

[36] T. J. Marks and J. R. Kolb, Chem. Rev. **77**, 263 (1977).

[37] (a) R. K. Nanda and M. G. H. Wallbridge, Inorg. Chem. **3**, 1798 (1964). (b) B. D. James, R. K. Nanda and M. G. H. Wallbridge, Inorg. Chem. **6**, 1979 (1967).

[38] T. J. Marks, W. J. Kennelly, J. R. Kolb and L. A. Shimp, Inorg. Chem. **11**, 2540 (1972).

[39] J. E. Bercaw in *Adv. Chem. Ser.* **167**, 136 (1978).

[40] N. Edelstein, Inorg. Chem. **20**, 297 (1981).

[41] (a) M. A. Bush and G. A. Sim, J. Chem. Soc. A, 2225 (1971). (b) I. A. Ronova, N. V. Alekseev, N. I. Gapotchenko and Yu. T. Struchkov, J. Organomet. Chem. **25**, 149 (1971).

[42] W. J. Highcock, R. M. Mills, J. L. Spencer, and P. Woodward, J. Chem. Soc., Dalton Trans, 821 (1986).

[43] S. B. Stones and J. L. Petersen, Inorg. Chem. **20**, 2889 (1981).

[44] C. J. Dain, A. J. Downs and D. W. H. Rankin, Angew. Chem. Int. Ed. Engl **21**, 534 (1982).

[45] (a) K. Franz and H. Nöth, Z. Anorg. Allg. Chem. **397**, 247 (1973). (b) K. Franz, H. Fusstetter and H. Nöth , Z. Anorg. Allg. Chem. **427**, 97 (1976).

[46] B. J. James and M. G. H. Wallbridge, J. Inorg. Nucl. Chem. **28**, 2456 (1966).

[47] H. Nöth and R. Hartwimmer, Chem. Ber. **93**, 2238 (1960).

[48] (a) E. V. Evdokimova, B. M. Bulychev and G. L. Soloveichik, Kinetika i Kataliz **22**, 170 (1981). (b) H. Nöth , J. Voitlander and M. Nussbaum, Nautrwissenschaften **47**, 57 (1960).

[49] K. M. Melmed, D. Coucouvanis, and S. J. Lippard, Inorg. Chem. **12**, 232 (1973).

[50] J. D. Axe, Ph. D. Dissertation, University of California at Berkeley (1960).

[51] D. Piehler, W. K. Kot and N. Edelstein, J. Chem. Phys. **96**, 942 (1991).

[52] R. Carlier and M. Genet, Radiochim. Acta **18**, 11 (1972).

[53] D. Brown and P. J. Jones, J. Chem. Soc. (A), 874 (1966).

[54] D. Brown and P. J. Jones, J. Chem. Soc. (A), 719 (1967).

[55] P. A. Sellers, S. M. Fried, R. E. Elson and W. H. Zachariasen, J. Am. Chem. Soc. **76**, 5939 (1954).

[56] R. Commandeur, H. Mathais, B. Raynier and B. Waegell, Nouv. J. Chim. **3**, 385 (1979).

[57] H. L. Krauss and G. Gnatz, Chem. Ber. **95**, 1023 (1962).

[58] H. L. Krauss and J. Nickl, Z. Naturforsch. **20b**, 630 (1965).

[59] P. R. Hammond and R. R. Lake, J. Chem. Soc. (A), 3800 (1971).

[60] D. Brown and P. J. Jones, J. Chem. Soc. (A), 262 (1966).

[61] E. Dornberger, R. Klenze and B. Kanellakopulos, Inorg. Nucl. Chem. Lett. **14**, 319 (1978).

[62] Synthesis of MeCpNa by M. Weydert.

[63] N. Edelstein, J. C. Krupa, R. C. Naik, K. Rajnak, B. Whittaker and D. Brown, Inorg. Chem. **27**, 3186 (1988).

[64] K. R. Lea, M. J. M. Leask and W. P. Wolf, J. Phys. Chem. Solids **23**, 1381 (1962).

[65] (a) N. Bloembergen, Phys. Rev. **104**, 324 (1956). (b) B. Bleaney, Proc. Phys. Soc. London **73**, 937 (1959).

[66] (a) B. Bleaney, Proc. Phys. Soc. London **73**, 939 (1959). (b) Y. Ayant, E Belorizky and J. Rosset, J. Phys. Radium **23**, 201 (1962). (c) D. Deschamps and Y. Merle d'Aubigne, Phys. Lett. **8**, 5 (1964). (d) E. R. Bernstein and L. W. Dennis, Phys. Rev. B **20**, 870 (1979).

[67] W. Low and R. S. Rubins, Phy. Rev. **131**, 2527 (1963).

[68] B. Klenze, A. H. Stollenwerk, J. Müller, and B. Kanellakopulos in Proceedings of 11ème Journées des Actinides, Jesolo, (1981), p.51.

[69] J. C. Krupa, S. Hubert, M. Foyentin, E. Gamp and N. Edelstein, J. Chem. Phys. **78**, 2175 (1983).

[70] E. Gamp, R. Shinomoto, N. Edelstein and B. R. McGarvey, Inorg. Chem. **26**, 2177 (1987).

[71] See, for example, (a) *NMR of Paramagnetic Molecules*, edited by G. N. LaMar, W. D. Horrocks and R. H. Holm, Jr., (Academic, New York, 1973). (b) B. R. McGarvey in *Fundamental and Technological Aspects of Organo-f-Element Chemistry*, edited by T. J. Marks and I. L. Fragalà, (D. Reidel, Dordrecht, 1985).

[72] R. J. Kurland and B. R. McGarvey, J. Mag. Reson. **2**, 286 (1970).

[73] (a) D. A. Goodings and V. Heine, Phy. Rev. Lett. **5**, 370 (1960). (b) A. J. Freeman and R. E. Watson, Phy. Rev. Lett. **5**, 498 (1960). (c) R. E. Watson and A. J. Freeman, Phy. Rev. Lett. **6**, 277 (1961). (d) S. S. Hanna, J. Heberle, C. Littlejohn, G. J. Perlow, R. S. Preston and D. H. Vincent, Phy. Rev. Lett. **4**, 177 (1960). (e) S. S. Hanna, J. Heberle, G. J. Perlow, R. S. Preston and D. H. Vincent, Phy. Rev. Lett. **4**, 513 (1960).

[74] A. Abragam, J. Horowitz and M. H. L. Pryce, Proc. Roy. Soc. London **A230**, 169 (1955).

[75] W. B. Lewis, J. A. Jackson, J. F. Lemons and H. Taube, J. Chem. Phys. **30**,694 (1962).

[76] R. E. Watson and A. J. Freeman , Phy. Rev. **156**, 251 (1967).

[77] J. M. Baker, J. Phys. C **1**, 1670 (1968).

[78] J. D. Axe and G. Burns, Phys. Rev. **152**, 331 (1966).

[79] (a) B. R. McGarvey, J. Chem. Phys. **65**, 955 (1976). (b) B. R. McGarvey, J. Chem. Phys. **65**, 962 (1976).

[80] B. R. McGarvey, J. Chem. Phys. **70**, 4971 (1979).

[81] J. Reuben and D. Fiat, J. Chem. Phys. **51**, 4909 (1969).

[82] S. D. Stults, Ph. D. Dissertation, University of California at Berkeley, (1988).

[83] R. K. Rosen, Ph. D. Dissertation, University of California at Berkeley, (1989).

[84] M. Weydert, personal communication.

[85] B. Kanellakopulos, R. Klenze, G. Schilling and A. H. Stollenwerk, J. Chem. Phys. **72**, 6311 (1980).

[86] B. Kanellakopulos in *Organometallics of the f-Elements*, edited by T. J. Marks and R. D. Fischer, (D. Reidel, Dordrecht, 1979).

[87] K. W. Bagnall, D. Brwon and J. G. H. du Preez, J. Chem. Soc., 2603 (1964).

LAWRENCE BERKELEY LABORATORY
UNIVERSITY OF CALIFORNIA
INFORMATION RESOURCES DEPARTMENT
BERKELEY, CALIFORNIA 94720